

AD-A239 201



2

PL-TR-91-2059 (I)

**BROADBAND STUDIES OF SEISMIC SOURCES
AT REGIONAL AND TELESEISMIC DISTANCES
USING ADVANCED TIME SERIES ANALYSIS METHODS**

**Zoltan A. Der
Michael R. Hirano
Kathleen A. Ziegler
R.H. Shumway**

**ENSCO, Inc.
5400 Port Royal Road
Springfield, Virginia 22151**

**DTIC
ELECTE
AUG 1 1991
S B D**

21 March 1991

**Final Report (Volume I)
29 September 1989 - 30 January 1991**

APPROVED FOR PUBLIC RELEASE; DISTRIBUTION UNLIMITED



**PHILLIPS LABORATORY
AIR FORCE SYSTEMS COMMAND
HANSCOM AIR FORCE BASE, MASSACHUSETTS 01731-5000**

91-06568



91

7

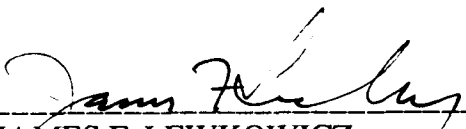
00


000

SPONSORED BY
Defense Advanced Research Projects Agency
Nuclear Monitoring Research Office
ARPA ORDER NO. 5307


MONITORED BY
Phillips Laboratory
Contract No. F19628-89-C-0030

"This technical report has been reviewed and is approved for publication."


JAMES F. LEWKOWICZ
Contract Manager
Solid Earth Geophysics Branch
Earth Sciences Division


JAMES F. LEWKOWICZ
Branch Chief
Solid Earth Geophysics Branch
Earth Sciences Division

FOR THE COMMANDER


DONALD H. ECKHARDT
Director
Earth Sciences Division

This report has been reviewed by the ESD Public Affairs Office (PA) and is release-able to the National Technical Information Service.

Qualified requestors may obtain additional copies from the Defense Technical Information Center. All others should apply to the National Technical Information Service (NTIS).

If your address has changed, or if you wish to be removed from the mailing list, or if the addressee is no longer employed by your organization, please notify PL/IMA, Hanscom AFB, MA 01731-5000. This will assist us in maintaining a current mailing list.

Do not return copies of this report unless contractual obligations or notices on a specific document requires that it be returned.

UNCLASSIFIED

SECURITY CLASSIFICATION OF THIS PAGE

REPORT DOCUMENTATION PAGE																
1a. REPORT SECURITY CLASSIFICATION Unclassified		1b. RESTRICTIVE MARKINGS N/A														
2a. SECURITY CLASSIFICATION AUTHORITY		3. DISTRIBUTION/AVAILABILITY OF REPORT Approved for public release distribution unlimited														
2b. DECLASSIFICATION/DOWNGRADING SCHEDULE																
4. PERFORMING ORGANIZATION REPORT NUMBER(S) SAS-TR-91-49		5. MONITORING ORGANIZATION REPORT NUMBER (S) PL-TR-91-2059 (I)														
6a. NAME OF PERFORMING ORGANIZATION ENSCO, Inc.	6b. OFFICE SYMBOL (if applicable)	7a. NAME OF MONITORING ORGANIZATION DCASMA, Baltimore														
8a. ADDRESS (CITY, STATE, AND ZIP CODE) 5400 Port Royal Road Springfield, VA 22151-2388		7b. ADDRESS (CITY, STATE, AND ZIP CODE) 200 Towsontown Blvd., West Towson, MD 21204														
8a. NAME OF FUNDING/SPONSORING ORGANIZATION Phillips Laboratory	8b. OFFICE SYMBOL	9. PROCUREMENT INSTRUMENT IDENTIFICATION NUMBER F19628-89-C-0030														
8c. ADDRESS (City, State, and Zip Code) Hanscom Air Force Base Massachusetts 01731-5000		10. SOURCE OF FUNDING NUMBERS <table border="1"><tr><td>PROGRAM ELEMENT 62714E</td><td>PROJECT NO. 9A10</td><td>TASK NO. DA</td><td>ACCESSION NO. WORK UNIT BA</td></tr></table>			PROGRAM ELEMENT 62714E	PROJECT NO. 9A10	TASK NO. DA	ACCESSION NO. WORK UNIT BA								
PROGRAM ELEMENT 62714E	PROJECT NO. 9A10	TASK NO. DA	ACCESSION NO. WORK UNIT BA													
11. TITLE (Include Security Classification) Broadband Studies of Selsmic Sources at Regional and Teleseismic Distances Using Advanced Time Series Analysis Methods																
12. PERSONAL AUTHOR(S) Dr. Zoltan A. Der, Mr. Mike Hirano, Ms. Kathleen A. Ziegler and Dr. R. H. Shumway																
13. TYPE OF REPORT Final (Volume I)	13b. TIME COVERED FROM 9/29/89 TO 1/30/91	14. DATE OF REPORT (Year, Month, Day) 1991 March 21		15. PAGE COUNT 192												
16. SUPPLEMENTARY NOTATION																
17. COSATI CODES <table border="1"><tr><th>FIELD</th><th>GROUP</th><th>SUB-GROUP</th></tr><tr><td></td><td></td><td></td></tr><tr><td></td><td></td><td></td></tr><tr><td></td><td></td><td></td></tr></table>		FIELD	GROUP	SUB-GROUP										18. SUBJECT TERMS (Continue on reverse if necessary and identify by block number) Seismic signal processing Nuclear test monitoring Frequency-domain decomposition		
FIELD	GROUP	SUB-GROUP														
19. ABSTRACT (Continue on reverse if necessary and identify by block number) <p>This report explores broadband seismic signal processing aimed at extracting information relevant to several key aspects of nuclear monitoring, yield estimation, source studies and discrimination. The term "broadband processing" in our definition refers to techniques designed for extracting the <i>maximum information</i> allowed by the S/N ratio from the data, using an information-theoretical definition, not the conventional waveform inversion of the so-called broadband seismograms, and estimating error bounds for parameters estimated. Another recurrent central idea examined and exploited in this report is the frequency-domain decomposition of multi-event, multi-sensor data into source and site factors. Various ensemble-averaged coherence measures can then be used to test the effectiveness of such factorization.</p>																
20. DISTRIBUTION/AVAILABILITY OF ABSTRACT <input type="checkbox"/> UNCLASSIFIED/UNLIMITED <input checked="" type="checkbox"/> SAME AS REPORT <input type="checkbox"/> DTIC USERS		21. ABSTRACT SECURITY CLASSIFICATION UNCLASSIFIED														
22a. NAME OF RESPONSIBLE INDIVIDUAL James F. Lewkowicz		22b. TELEPHONE (Include Area Code) (617) 377-3222		22c. OFFICE SYMBOL PL,LWH												

DD FORM 1473, 84 MAR

UNCLASSIFIED

SECURITY CLASSIFICATION OF THIS PAGE

Unclassified

SECURITY CLASSIFICATION OF THIS PAGE

19.

Following a brief discussion of spectral factorability and motivations for broadband analysis, the report is subdivided into four main sections. In Section 1.0, we examine the spectral factorability of P_n and Lg phases recorded at NORESS and the 3C subarray of NORSAR. We find that closely located events can be subdivided into distinct factorable groups with coherence measures indicating high effectiveness of factorization. Events not within such groups do not factor efficiently, and thus, result in a low coherence measure. The factorizable groups are probably events which are close in location, depth and source mechanism. Within factorizable groups, fine details of regional waveforms can be reconstructed from source and site factors. This is the first utilization of the information in the *details* of regional waveforms we know of; even the most ambitious direct modeling efforts can reproduce only envelope shapes and a few main features, such as relative phase amplitudes of regional seismograms. Factorization studies can thus result in better location and the detection of anomalous events with differing source mechanisms or depths (such as decoupled large explosions in some evasion scenarios). Methods are described for diagnosing regional waveform differences due to relative location in source time functions, source depths and mechanisms using standard linear system concepts. Neither the source time functions nor the Green's functions need be known for such analyses.

Section 2.0 re-examines some aspects of estimating secondary arrivals (pP, spall, etc.) in teleseismic P waves and applying corrections to m_b . A popular model (P+pP model) often used for interpreting P waves from nuclear explosions and deriving pP parameters consists of a site function convolved with a P and pP pulse sequence and some explosion source pulse (Lay, 1985; Murphy, 1989). Frequency domain analyses of data variance show that this model cannot explain a significant portion of the energy (30 - 40%) in the P waves from Pahute Mesa events for which such analysis methods were previously applied. Spectral factorization, which does not assume the P+pP model, on the other hand, accounts for 90 - 95% of the energy in both Pahute Mesa and Kazakh events. Therefore, the complex source waveforms often seen in multi-channel deconvolved P waves from nuclear explosions at both Pahute Mesa and the Kazakh test sites are required for explaining the data and reflect the actual complexity of P waves radiated from nuclear explosions. It is shown that magnitude-yield relationships appropriate to the generic pP characteristics, derived from multi-channel deconvolutions of nuclear explosions (and appropriate t^*), are similar to those directly derived by regression analyses of m_b data and published yields of nuclear explosions for Pahute and Kazakh test sites by Jih (1990).

Section 3.0 explores ways to perform spatio-temporal source inversion using waveform data. The formalisms used are generalizations of F-K algorithms. Shumway's F-K method, compounded over various frequencies, is used mostly in this part of the report. Unlike many of the F-K statistics in use, the statistics for each frequency has a known, non-central F, statistical distribution. Assuming that the compounded statistics is approximately normal, confidence bounds on the various parameters derived could be estimated. An alternative statistic having a central χ^2 distribution has also been derived. We explored the resolution of inversion of long period body waveforms and concluded that it is extremely poor and we suggest that such methodologies must be replaced by more precise methods. The concepts are demonstrated by analyses of actual data from nuclear explosions and three earthquakes: the 1966 El Golfo, the 1976 Kazakh and the 1988 Armenian events. Much needs to be done for further refinement of the methodology we have developed.

In the last part of the report we describe an approach for S/N ratio enhancement, using the application of site waveform-equalization, together with adaptive filtering. This combines the reduction of the beam loss with the advantages of optimum-filtering. The method was applied to both regional and teleseismic array data. We found that, typically, we were able to obtain a 4 - 6 dB improvement relative to conventional beamforming. This S/N ratio improvement is significant enough to be pursued further, despite the complexity of the processing.

Unclassified

SECURITY CLASSIFICATION OF THIS PAGE

TABLE OF CONTENTS

SECTION	PAGE
Introduction	1
1.0 Coherent Processing of Regional Signals at Seismic Arrays.....	12
General Considerations	12
A summary of the diagnostics for grouping events with respect to location mechanism and/or source depth.	21
Analyses of NORESS Data from Quarry Blasts in Scandinavia	22
Coherence and cross-filtering analyses	22
Site equalization processing.....	36
Factorizability studies and coherence grouping of Estonian mine blasts.....	42
Summary of the processing results for regional array data	50
2.0 Further Analyses of Deconvolution Results.....	52
General Discussion	52
Arguments in Favor of the Deconvolution Approach.....	58
Tests of Some pP Results from the Literature	59
Deconvolution Results and their Consequences with Respect to Magnitude-Yield	70
3.0 Studies of Spatio-Temporal Resolution in Source Inversions.....	78
General Discussion	78
Quantification of Time Domain Waveform Fits	83
Statistical Analysis of the Source Inversion Problem.....	90
Depth estimation error limits for the 1966 El Golfo earthquake	102
Imaging of the 1988 Armenian earthquake.....	108
Imaging of selected nuclear explosions from Kazakh.....	119
Analysis of surface waves from Kazakh nuclear explosions.....	122
Depth imaging of the 1976 Kazakh earthquake.....	127
Summary of Section III	127
4.0 Tests of Various S/N Optimization Algorithms	132
General Remarks.....	132
Processing of Teleseismic P waves Recorded at Large Seismic Arrays.....	133

Processing of Western Norway Earthquakes Recorded at NORESS.....	138
Conclusions.....	140
5.0 References.....	143

Appendices

Appendix A - Source Imaging - A Statistical Theory.....	A-1
Appendix B - An Alternative Method for Source Imaging.....	B-1
Appendix C - Implementation of Multi-Channel Deconvolution in an X-Windows Environment.....	C-1

List of Figures

List of Tables



Accession For	
NTIS GRA&I	<input checked="" type="checkbox"/>
DTIC TAB	<input type="checkbox"/>
Unannounced	<input type="checkbox"/>
Justification	
By	
Distribution/	
Availability Codes	
Dist	Avail and/or Special
A-1	

LIST OF FIGURES

Figure 1: Decomposition and reconstruction of a matrix of seismograms, using site and source spectral factor representation.

Figure 2: Scenarios for which spectral factorability may be valid. a) Teleseismic P from a limited source region recorded at a seismic array. b) Network recordings of groups of events with similar radiation patterns.

Figure 3: Flow diagram of the spectral factorization process utilized in this report.

Figure 4: Map of Scandinavia with the location of NORESS and Titania, Blasjo and the Estonian mines studied.

Figure 5: a) Selected reconstructed and data traces of Pn arrivals from the Titania1 event. b) The same for the Titania4 event. The designation C2 refers to the second sensor in the C ring of NORESS, etc.

Figure 6: a) Selected reconstructed and data traces of Lg arrivals from the E4-1 event. b) The same for the E4-4 event. The designation C2 refers to the second sensor in the C ring of NORESS, etc.

Figure 7: Spectra for various regional arrivals from the Titania mine. Note that the spectral modulation is similar, regardless of the type of arrival.

Figure 8: Inter-event coherences for Pn arrivals from the Titania mine.

Figure 9a: Wiener filtering results for transforming Event Titania4 into Event Titania1.

Figure 9b: Wiener filtering results for transforming Event Titania4 into Event Titania3.

Figure 10: Cross-correlations of the site-equalized traces of Pn between sensors D1 and D5 for selected Titania events.

Figure 11: Site-equalized Pn traces for selected Titania events between sensors D1 and D5.

Figure 12: Cross-correlation of the site-equalized traces and the equalized traces of Lg between sensors D1 and D5 for the E9 event. Note the excellent similarity between the cross-equalized traces.

Figure 13: Results of site-equalization when spectral factors from joining factorization of E1 and E4 Events were utilized. Although the cross-correlations still have peaks at the proper alignment with reduced correlation coefficients, (a) the efficiency of site-equalization is greatly degraded as evidenced by the poor similarity of the site-equalized traces (b).

Figure 14: Site-averaged coherence results from the joint factorization of three E9 events and one E4 event.

Figure 15: Site-averaged coherence results from the joint factorization of four E9 events with reconstructions of one event being much less similar to the original data than the others.

Figure 16: Envelopes of band-pass filtered traces Type I of E9 Event.

Figure 17: Envelopes of band-pass filtered traces Type II of Event E9. Even though these events seem to be noisier than those of Figure 16, the S/N ratio for Lg for these events is about the same as for E9.

Figure 18: Coherences demonstrating the high factorization efficiency - 90 to 95% of the energy accounted for, across the 3 C subarray of NORSAR, of the Pn phases from a group of closely located FENNOLORA profiling shots. What is noteworthy about this is the relatively large spacing about 5 km, of the subarray sensors.

Figure 19: Methods for testing the efficiency (portion of energy accounted for). a) By spectral factorization. b) By the P+pP model.

Figure 20: Some typical deconvolution results for various test sites.

Figure 21: Data and reconstructions using the spectral factorization method.

Figure 22: Waveform inter-correlation results at NORSAR using Murphy's (1989) pP parameters for Pahute Mesa events. The waveforms at the same sensors should be identical, but they are not indicating that the P+pP model and/or the pP parameters are invalid.

Figure 23: Portion of P wave energy in Pahute Mesa events accounted for at NORSAR by Lay's (top row), Murphy's pP parameters (second row) all shown by dashed lines. The energy accounted for in Pahute Mesa events by spectral factorization (multi-channel deconvolution) is shown by solid lines in the first two rows. The bottom graph shows the average value of the same for Kazakh events obtained by spectral factorization.

Figure 24: Simulated WWSSN m_b for the three test sites obtained by using the source model of von Seggern and Blandford (1972), t^* derived from P spectra and pP parameters derived from deconvolution. Note the large NTS-Kazakh bias and the Degelen negative offset relative to Shagan. The M_s - m_b lines have a pronounced curvature and the biases increase with decreasing yield. The two sets of curves are for stations located in shield and tectonic areas respectively. Identical source media were assumed for simplicity.

Figure 25: Simulated WWSSN m_b for the three test sites obtained by using the source model of Mueller and Murphy (1971), t^* derived from P spectra and pP parameters derived from deconvolution. Note the large NTS-Kazakh bias and the Degelen Negative offset relative to Shagan. The M_s - m_b lines have little curvature and the biases increase only slightly with decreasing yield. The latter features are more in agreement with the data. Identical source media were assumed for simplicity.

Figure 26: Jih's regression results for NTS and Kazakh (Degelen and Shagan) events using maximum likelihood analyses of actual and simulated P waves (recorded at other stations transformed to WWSSN response). Note the offset of Degelen relative to Shagan and the large NTS-Shagan difference that increase with decreasing m_b . Note the similarities of these lines to the general features in Figure B1 and especially to those in Figure 25.

Figure 27: Waveforms used for computing the data synthetic coherences in Figure 3. The different traces are shown below each pair. The two numbers next to each pair are the reference number in Table II and the time domain correlation coefficient.

Figure 28: Averaged spectra of a sample of long period data and synthetic seismogram pairs randomly selected from the literature.

Figure 29: Ensemble-averaged coherences of our sample of data synthetic pairs defining the "average fit". The 95% limit shows the level below which the coherences are not significantly different from zero.

Figure 30: Perspective views of the variations of the frequency-compounded F statistics over the frequency range of 0.02-0.15 Hz for a pair of double-couple point sources with equal power. Uniform random noise was added to simulate a fit with an average correlation coefficient of 0.9. The peak value occurs between the two sources and the two sources were not resolved. The F statistics were computed for various assumed source depths and the sides of the source region views are 250 km long. The maximum value of the statistic and its location in gridpoint coordinates from the left lower corner (5 km spacing was used in both x and y) are given beside each view. The gridpoint x-y coordinates of the two synthetic sources were at 27, 27 and 31, 31 and the depths were at 3 and 9 km respectively.

Figure 31: Perspective views of the variations of the frequency-compounded F statistics over the frequency range of 0.02-0.35 Hz for a pair of double-couple point sources the F values were computed for various assumed source depths. Random noise with 16% of the signal was added throughout the band. The peak values occur nearer to the two sources and the two sources were marginally resolved (for additional details of this display see the caption of Figure 4).

Figure 32: Perspective views of the variations of the frequency-compounded F statistics over the frequency range of 0.15-0.35 Hz, thus deleting the low frequencies, for a pair of double-couple point sources the F values were computed for various assumed source depths. Random noise with 16% of the signal was added throughout the band. The peak values occur near to the two sources and the two sources were well resolved (for additional details of this display see the caption of Figure 4).

Figure 33: Perspective views of the variations of the positive parts of the simulated site-averaged time domain data vs. probe vector (data synthetic) correlation coefficient over the frequency range of 0.02-0.15 Hz for a pair of double-couple point sources the F values were computed for various assumed source depths. The negative parts of the correlation coefficient were set to zero arbitrarily, since only peak positive values are of interest. Random noise was added throughout the band to give a peak value near 0.9. The two sources were not resolved (for additional details of this display see the caption of Figure 4).

Figure 34: a) F statistics computed for the set of synthetic seismograms appropriate to the El Golfo crustal and point source model at 10 km depth as fitted to a wide range of depths. Five percent random white noise was added to avoid singularity in the solution. The dashed lines are approximate 95% confidence limits to the F values. The maximum unambiguously defines a depth of 10 km. b) F statistics computed using the actual P waves from the El Golfo earthquake and fitted to a wide range of depths. The dashed lines are approximate 95% confidence limits. The arrows indicate the large acceptable depth range which is consistent with the F values.

Figure 35: Selected data and synthetic seismograms appropriate to various source depths for El Golfo earthquake. The "best" time domain waveform fits occur at difference depths at the various stations.

Figure 36a: Matching the three subevent source models for the Armenian earthquake against themselves in the 0.1-1.0 Hz range using both perspective views and contour plots. Note that the distance scales are different on the horizontal (EW) and the vertical (NS) axes. a) Subevent 1.

Figure 36b: Subevent 2.

Figure 36c: Subevent 3. Perspective views are on top and contour plots of the same surface are below. The sizes of grids are 127.5 km x 127.5 km with 51 subdivisions in each direction.

Figure 37a: Matching the three subevent source models for the Armenian earthquake against each other in the 0.1-1.0 Hz range. a) Model 2 against Model 1.

Figure 37b: Model 3 against Model 1.

Figure 37c: Model 3 against Model 2. Note that the distance scales are different on the horizontal (EW) and the vertical (NS) axis. Perspective views are on top and contour plots of the same surface are below. The sizes of grids are 127.5 km x 127.5 km with 51 subdivisions in each direction.

Figure 38a: Matching the three subevent source models for the Armenian earthquake against P wave data from eight teleseismic stations in the 0.1-1.0 Hz range. Matching with a) Subevent 1.

Figure 38b: Subevent 2.

Figure 38c: Subevent 3. Note that the dominant feature is a EW trending ridge. Perspective views are on top and contour plots of the same surface are below. The size of grids are 127.5 km x 127.5 km with 51 subdivisions in each direction.

Figure 39: Shumway's statistic as a function of depth computed from deconvolved P wave seismograms of the December 25, 1975 Kazakh nuclear explosion.

Figure 40: Shumway's statistic as a function of depth computed from deconvolved P wave seismograms of the June 29, 1977 Kazakh nuclear explosion.

Figure 41: Surface wave imaging of two nuclear explosions at the Kazakh test site (October 12, 1980 on top and September 14, 1980 on the bottom) by the Capon algorithm. The geographical coordinates of the centers of the print plot grids are 50N-79E and the events are plotted relative to that. Filled circles denote the locations, obtained from body waves, as listed by unclassified files at the Center for Seismic Studies, triangles show maxima of the Capon's statistics. The grids are 50 km on each side, and the tops are facing North.

Figure 42: Deconvolved waveforms of the Kazakh earthquake at three UK arrays. Besides the surface reflections pP and sP there is an early phase which is probably a Moho-converted phase (Pooley et al 1983).

Figure 43: Depth imaging of the 3/20/1976 Kazakh earthquake.

Figure 44: Comparisons of noise adaptation with out (bottom) and with (top) the site response removed. Comparing the shapes and levels of spectra it can be seen that the overall noise is significantly reduced by the adaptive beaming method relatively to the beams, especially below 2 Hz. The adaptive beams quickly adapt to the noise, and after a few oscillations the overall noise levels are much reduced relative to the beam outputs.

Figure 45: Teleseismic P waves recorded at EKA processed by beaming and adaptive filtering with and without removal of site frequency responses.

Figure 46: Spectra representative to the signal beam loss (top) and the S/N gain obtained for two events by using the four modes of processing described in the text.

Figure 47: Optimum processing of the nuclear explosion Mast, overlain by added amplified actual background noise, at NORSAR. The best performance, about 2:1 S/N gain, is associated with site equalization followed by adaptive beaming (bottom trace). It must be pointed out, that contrary to any superficial appearances, this is not equivalent to frequency filtering since this process works by spatial filtering only and does not change the spectrum or waveforms of any signals.

Figure 48: Noise reduction gain and beam loss for western Norway earthquakes as processed by beaming and adaptive filtering with and without removing the site transfer functions.

LIST OF TABLES

- Table I: List of "Titania" Events
- Table II: List of "Estonia" Events
- Table III: Intercorrelation Results with pP Parameters Derived from Spectra
- Table IV: Intercorrelation Results with WWSSN Data Using Published pP Parameters for Pahute Events
- Table V: Sources of Waveform Synthetic Pairs for Coherence Analyses
- Table VI: Station Parameters for Numerical Simulations
- Table VII: Separation of Compressional and Deviatoric Sources with Capon's Algorithm.

INTRODUCTION

The term "broadband analysis" is often used in seismology to designate time domain studies of displacement seismograms where the effects of the instrument response were made flat, over a wide frequency band. The resulting seismograms thus will show the actual ground displacement within a wide frequency band, but will still contain the effects of Q and source time functions. Because of these limitations, matching the waveforms of such data may not extract the maximum information available, although modeling in a wider frequency band is preferable to working with either the standard short or long period instrument recordings alone. Time domain waveform-matching, using RMS fitting criteria, will inevitably weight the information in the frequency domain proportionately to the actual power spectra of the signals as they appear on the broadband seismograms. The situation will be much worse if we only use the outputs of some standard instruments, such as the WWSSN short period and the LRSM long period, which have notoriously narrowband characteristics. The problem is further limited by the presence of background noise. Assuming that we have a knowledge of the variations of the S/N ratio as a function of frequency for the data we wish to analyze the extraction of source and path, information from the data can be optimized by considering some basic formulas of information theory. Estimates of the S/N ratio, as a function of frequency, can be obtained by simply comparing the spectra of the seismic data in the signal window to those in the noise windows preceding them. Thus, we may apply Shannon's formula for the rate of the information transfer *capability* by a noisy channel,

$$I = B T \log \left(1 + \frac{P_s}{P_n} \right) \quad (1)$$

which basically tells us how to weight the data with respect to frequency in order to extract the most information. In this equation, B is the bandwidth, T is the time sample length and P_s and P_n

are the power levels of the signal and noise, respectively. If base 2 logarithm is used, the formula gives the amount of information in bits. When the signal-to-noise power ratio varies with frequency, we can subdivide the spectrum into bands with roughly constant S/N ratios and estimate the information over the total signal band by summing the information contributions for all bands. Weighting the data according to the formula above, is the ideal we should be striving for and it should form the definition of "broadband processing." We should attempt to fit both the amplitudes and phases of the frequency components of the signals with our models throughout the frequency bands where the S/N ratio is good. It should be clear that this is not what is being done in most seismological source inversion studies. Waveform inversion studies that utilize data from only one type of narrowband instrument and that is uncompensated for Q or source effects essentially discard most information. In effect, the information contained at higher frequencies is often totally ignored and these frequencies often contain the most information and provide the most resolution in space and time. In the case of misfitted high S/N signals, we may regard the power in the differences of the signals to be fitted and those predicted from a model as "misfitting noise," to be included into P_n in Equation (1).

The amount of information that can be extracted from conventional time-domain source inversions is determined by the mean square effective bandwidth B_e , defined as

$$B_e^2 = \frac{\int_{-\infty}^{\infty} f^2 P_s(f) df}{\int_{-\infty}^{\infty} P_s(f) df} \quad (2)$$

where f is frequency and the integrals are centered around the main peak (for unimodal $P(f)$). It should be clear that the effective bandwidth will depend on the instrument type, source function

and the Q along the path, and thus, the results will depend on these as well. This is very undesirable, since none of these variables has anything to do directly with the *information available* in the actual signals. If an inversion method based on Equation (1) is applied and optimized over various frequency bands, the results will depend only on the S/N ratio and the true information content as defined by Shannon's formula. We shall return to these points later.

An often stated justification for the de-emphasis of high frequency information is that waveforms appear to be quite unstable at frequencies as low as 1 Hz, and they vary strongly with small changes of location of the sensors (this fact, on the other hand, did not stop many workers from fitting, in fine detail, short period waveforms at less than a dozen stations by quite refined source-path models). It was found, however, that these variations in waveforms can generally be specified as repeatable path-dependent inter-sensor transfer functions, which can be estimated and removed from the data (Filson and Frasier, 1972; Der et al, 1985). Therefore, it is possible to extract valuable source information from the data at high frequencies, but at the expense of much more work that has to be done on the estimation of site-transfer functions and the resulting loss in the degrees of freedom. High-frequency seismic waves provide the most resolution with regard to the details of the source processes of interest in nuclear monitoring, such as estimating pP time delays, strain release mechanisms, etc., and should not be neglected.

Since spectral factorization is another one of the main themes of this report and it can be applied to various types of data, it is necessary to include a discussion of it prior to the beginning of the presentation of the results of data analyses. Spectral factorability is defined simply by the following equation defining the spectra $F_{ij}(\omega)$ of a given short period or high-frequency seismic arrival from multiple events, i and recorded at multiple sensors, j ,

$$F_{ij}(\omega) = S_i(\omega) R_j(\omega) + N_{ij}(\omega) \quad (3)$$

where $S_i(\omega)$ are source spectral factors, $R_j(\omega)$ are receiver (site) spectral factors and $N_{ij}(\omega)$ are ambient noise terms (Figure 1). The existence of site factors $R_j(\omega)$ is well-documented at seismic arrays and is the main cause of the variability of waveforms at the various sensors of the arrays. The site factors are the results of the structural complexities near the receivers and have been shown to be strongly dependent on the azimuths and slownesses of arrivals. Equation (3) is, therefore, valid only if the $R_j(\omega)$ are common to the full set of data $F_{ij}(\omega)$, i.e., the slowness vectors are the same for all the sensors for the data set. The $R_j(\omega)$ are, unfortunately, not able to be modeled deterministically from the usually scant knowledge of receiver structures and must be estimated from the data. It is generally not possible to uniquely define both factors $S_i(\omega)$ and $R_j(\omega)$ from a data set either, because we can always divide out some arbitrary function, $F(\omega)$ from all $S_i(\omega)$, and multiply all $R_j(\omega)$ with it to get new, equally valid source and site functions (Der et al, 1987). Nevertheless, in some cases (teleseismic P waves), some reasonable physical and semi-empirical assumptions can be made that limit the possible choices and define the two types of factors more uniquely, thus, reducing the possibilities of such trade-offs. The fact that Equation (3) holds in many cases is hardly surprising. One would naturally expect that taking spectral ratios between waveforms of the same type of pairs of events at common, closely-grouped sites, would tend to reflect the ratios of the effective source functions. The main point here is the utilization of this phenomenon for the elimination of the site effects and the exploitation of the redundancy in such data sets for reducing noise. Clearly, we have redundancy if we have $N > 2$ events and $M > 2$ sensors, since then $MN > M+N$.

The $R_j(\omega)$, besides being functions of the azimuth and distance of the sources, will also be dependent on the type or modal composition of the waves we want to factor. This plays a role when we try to analyze regional wave groups, which have common generic names such as Lg, but may consist of different sets of modes. Instead of getting bogged down in the discussion of various theoretical models, we shall attempt to clarify some of these statements below with concrete illustrative cases.

The first is the case of P waves from limited source regions recorded at individual teleseismic arrays (Figure 2a). Since the slownesses and the take-off angles for all arrivals are practically identical, the effective site-functions will remain the same for the various events at the

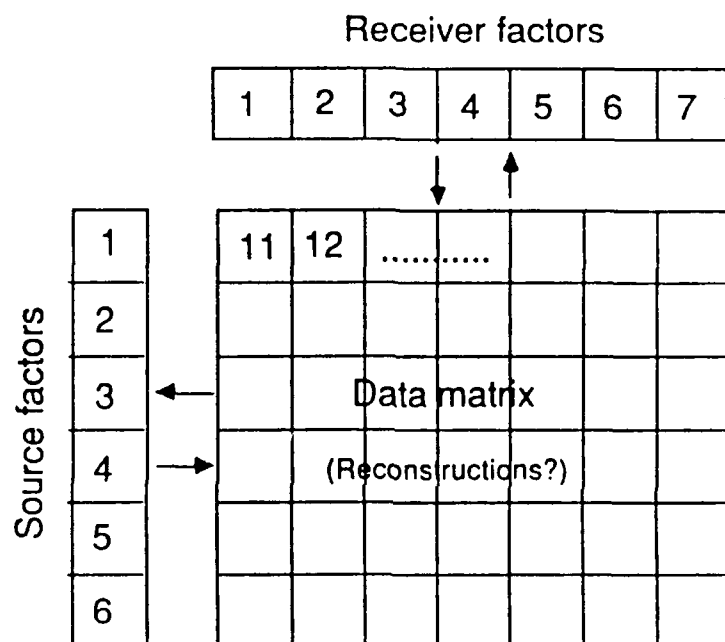


FIGURE 1: Decomposition and reconstruction of a matrix of seismograms, using site and source spectral factor representation.

same sensor. Moreover, because the array looks at a very small segment of the radiation patterns, the source functions will be the same for all sensors of a given event. This is the definition of factorability in Equation (1) and thus, groups of all events, earthquakes or explosions, will be factorable. This is the case which was most extensively studied in the past (Der et al, 1986; 1987; 1988). In this application it is assumed that the time domain representations approximately average to a delta function when stacked over sites. The source functions thus derived will be "phaseless seismograms" (Stewart and Douglas, 1983) or band-limited representations of the effective P source function radiated in the direction of the array.

Let us assume now that instead of a single array, we use teleseismic P wave recordings of a number of stations at roughly the same distance from a limited source region, containing numerous events (Figure 2b). Even if a source has a perfectly symmetrical pattern of radiation, the waveforms observed may vary considerably because the site factors can be still quite different. Nevertheless, groups of events with identical radiation patterns will be factorable and the interpretation of the resulting source time functions remains valid. We have found that the RSTN and some subsets of UK array recordings of some sets of Shagan explosions were factorable, and some groups of Degelen events were not (Der et al, 1986; 1987). On the other hand, if we include one earthquake into a group of explosions, the group as a whole will not satisfy the factorability condition because of the different symmetry of the radiation from earthquakes making the source factor different for each sensor of such events. The same is the case for the groups of Degelen explosions just mentioned, as seen at subsets of UK arrays which have different radiation symmetries, possibly because of the complex topography at the site. Thus, factorization analysis in this case can be used to test relative symmetries in radiation of a group of events with obvious potential application for discrimination.

The third example consists of recordings of a regional phases, such as Lg, from a group of events located in a limited area at a small regional array (same situation as that shown in Figure 2a).

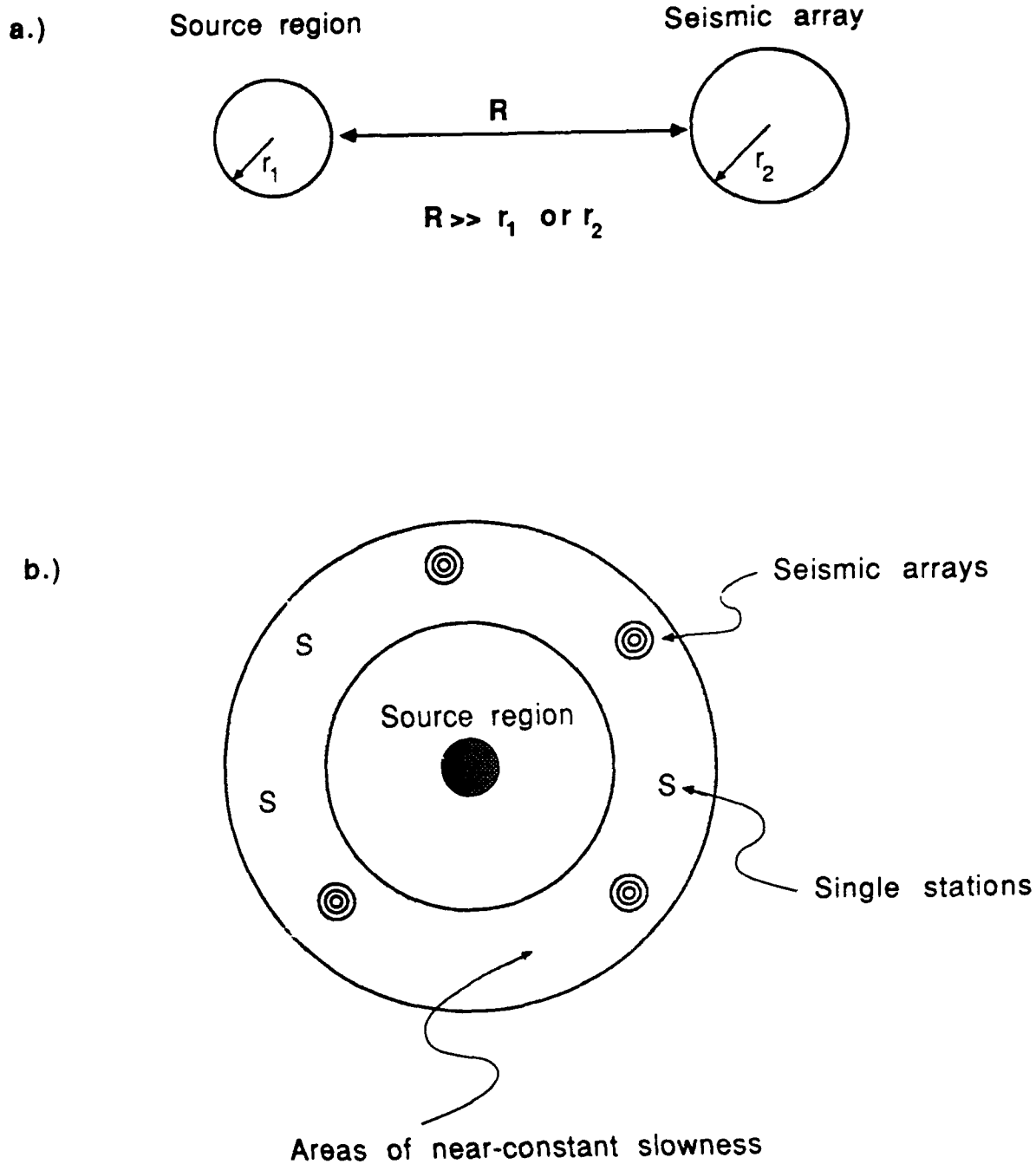


FIGURE 2: Scenarios for which spectral factorability may be valid. a) Teleseismic P from a limited source region recorded at a seismic array. b) Network recordings of groups of events with similar radiation patterns.

The designation, "Lg," is based on certain group velocity limits, not on the exact modal nature of the signals. Consequently, Lg wave groups can have different modal compositions from sources at similar locations, depending on the source mechanism and depths. Thus, Lg wave groups with similar modal compositions will interact with the near-site structures similarly and, thus, such groups will be spectrally factorable. In this application, it would not be prudent to assume that the time domain representations of site factors, averaged over sites, would still be an impulse. Thus, in this case, we simply test for the validity of a factorability equation without attempting to interpret the resulting source and site factors. When the Lg phases have different modal compositions, then the site factors that represent the interaction of the different set of modes and the associated set of site functions will be different also. Thus, it can be expected that groups of Lg (and other regional phases) from events with different modal compositions, as seen at the array, will not satisfy as a whole the factorability equation above. The obvious application of such analyses is to group closely located events with respect to differences in source mechanisms or depth.

It is easy to guess what the performance of the process would be in various other cases of source and site configurations on the basis of some general seismological principles and the examples discussed above. Given that factorability is valid for a given set of data, the remaining question is the nature of the sets of *transfer functions* that it implies. Clearly, if Equation (1) is satisfied then it will be possible to transform waveforms of the various events at all common sensors into each other by a filter constructed by taking the ratio of the respective source functions. Similarly, we can transform the waveforms recorded at various sites into each other for all common events, using filters that are ratios of the respective site functions.

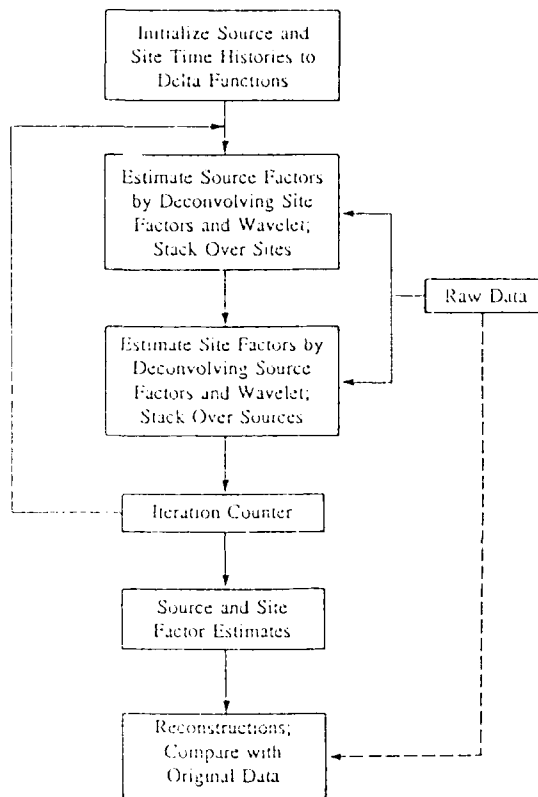
The factorization algorithm used in this report is the same as that used for multi-channel deconvolution. A flow diagram of the process is reproduced in Figure 3 for those unfamiliar with this process. For further details and statistical treatments, the reader is referred to our earlier publications (Shumway and Der, 1985; Der et al, 1987). The assumptions regarding the

interpretation of source time functions resulting from that procedure have no bearing with regard to the validity of factorization in the other applications in Section I.

Factorability implies that Equation (3) is satisfied by the spectra of a group of events (within limits allowed by the background noise). Ignoring the noise for the time being (assuming high S/N ratio), we need some way to measure how well the total energy in the data can be explained by the source and site factors as a function of frequency. There can be various ways to establish such a measure. Our choice is the average ensemble-averaged coherence defined as

$$C = \frac{\sum_e \sum_s \overline{f_d f_r}}{\sqrt{\sum_e \sum_s \overline{f_d f_d} \sum_e \sum_s \overline{f_r f_r}}} \quad (4)$$

Where overbar denotes spectral smoothing, f_d and f_r are Fourier transforms of data and reconstructions and the summations are over events and sites. All quantities in Equation (4) are implicit functions of frequency. In order to measure the trace similarities in small time neighborhoods, we apply heavy spectral smoothing. This measure has the advantage that statistics for testing significance are readily computed and the effect of background noise can also be considered. Another, alternative way to measure the same thing could be to take the difference of the corresponding data and reconstructed traces and compute the ratio of the powers in these residual traces and the data. Similar measures, with summations over sites and events only, can be also used to test the relative effectiveness of spectral factorization for individual events in a group or pairs of sensors and test alternative causal models of teleseismic P wave secondary arrival patterns in explaining the observed data (see Section 2.0).



A data matrix of P wave seismogram from a set of events observed at common sensors is being decomposed into source and site factors as described by the formula

$$Y_{ij}(\omega) = R_i(\omega) S_j(\omega)$$

This decomposition is verified by reconstructing the original data from the factors R and S.

FIGURE 3: Flow diagram of the spectral factorization process utilized in this report.

1.0 COHERENT PROCESSING OF REGIONAL SIGNALS AT SEISMIC ARRAYS

General Considerations

Obtaining source information from regional recordings is very important in treaty monitoring because of the concern about small, decoupled nuclear explosions possibly hidden in conventional firing patterns of quarrying operations. Thus far, little progress has been made, and practically no work done, in extracting information from regional waveforms by coherent processing, although spectral expressions of multiple-firing sequences have been discovered (Willis, 1963; Baumgardt and Ziegler, 1988). The disadvantage of the spectral and cepstral methods is that the phase information in the signals is discarded and that the modulation patterns depend on the similarity in the waveforms from the various individual shots making up the firing sequence. The advantage of such methods is that they are robust and do not otherwise depend on the details of propagation, unless multi-pathing occurs. In this report we shall discuss the general problem of regional waveform analysis and show how investigating the spectral structure of the data may help in recovering source information, in addition to that obtainable by other analysis methods.

A general conclusion that may be drawn from the numerous attempts of computing synthetic seismograms of regional arrivals, such as P_n , P_g , S_n and L_g , and comparing them to real data, is that it is quite impossible to compute. Green's functions with sufficient precision to synthetically reproduce detailed features of high-frequency regional waveforms use deterministic models. Waveforms of regional phases vary considerably with the locations of sensors, even across small arrays, such as NORESS. We do not have a sufficiently detailed knowledge of the geological structures to compute such waveforms, and even if we had such knowledge, we simply do not know how to compute synthetic seismograms for the complicated structures making up the earth's crust at the scale comparable to the short wavelengths involved. While it is possible to

obtain synthetic seismograms for long period and some standard short period seismograms that match observed waveforms in considerable detail, for regional seismograms, the best we can hope for is to match the overall characteristics of wave envelopes and relative phase amplitudes. Beyond attempting to match such gross characteristics of regional arrival, practically nothing has been done to utilize the information in the details of regional waveforms.

The question arises whether it will ever be possible to derive source related information from the detailed waveforms of regional seismograms, if we accept the fact that we shall never know the Green's functions. The answer to this question, based on the work to be presented below, is a qualified yes, although the possibilities seem to be limited due to the extreme variability of regional waveforms with source mechanism and the positions of the sources and receivers.

Before we present the results of our data analyses, it is necessary to describe some expected spectral characteristics of regional seismic arrivals from small explosions in the light of some elementary seismological considerations and observational facts. We know, for instance, that the time durations of source time functions of most quarry blasts are short, a few tenths of a second. In addition, spectral modulations observed for such events (Baumgardt and Ziegler, 1987) could not occur unless the subevents were very similar, so they could coherently interfere with each other. Moreover, since the spectral modulations for all the regional arrivals, P_n , P_g , S_n and L_g , are commonly similar (Figure 7), the spatial extent of such sources could not be large.

Otherwise, the modulations in the spectra would have been different for the various arrivals due to the differences in the delays in propagation, with the quite different phase velocities associated with each of these phases. Thus, in many cases, we may regard quarry blasts as point sources. We observe that the waveforms of regional arrivals vary considerably even over a small array. By reciprocity, we may expect that similarly small displacements of even identical sources will also cause differences in the waveforms if the source region has the same degree of lateral

variability in structures at the observing array. In order to utilize such information, the statistical nature of these inter-site transfer functions must thus be studied. One would expect, similarly to teleseismic site-transfer functions, that if the physical nature of the arrivals is the same, such as the case for teleseismic P, then they would interact with the geological structures near the recording sites in a similar fashion. Thus, we would expect the array spectral matrices to be factorable for events in limited source regions (Filson and Frasier, 1972; Der et al, 1987). The converse may be the case for some regional arrivals, such as Lg phases with different modal composition.

After these preliminary remarks, let us examine the general spectral structure of seismic arrivals in an arbitrary, heterogeneous anisotropic medium for various scenarios. Let us assume that we have source and receiver regions of limited spatial extent such that the dimensions of these regions are small, compared to the distance between them. Let r_i and r_j be the position vectors of the sources and the receivers in the two regions (Figure 2). The spectra of the observed seismograms from events can be written in the frequency domain by transcribing some known equations (Aki and Richards, 1980, p. 53) into the frequency domain:

$$F_{ij}(\omega) = \sum_{mn} M_{mni}(\omega) G_{mn}(\omega, r_i, r_j, d_i) \quad (5)$$

In this equation, the M_{mni} are the components of the moment tensor, each with its own source time function, and the G_{mn} are derivatives of Green's functions (they will be called Green's functions for simplicity in this report) associated with them. The index, i , is for the given source and j is for the sensor. In this expression, the index for component in Aki and Richards (1980), which is always vertical in this report, was dropped and the summation over moment tensor components is explicitly indicated, rather than implied by repetition of indices, in order to avoid confusion since some other indices will be repeated in the expressions in this report. The d_i refer to the dependence of the Green's functions on source depth, the receiver depth dependence is not indicated since the

receivers are assumed to be on the surface. This structure is equivalent to a multi-channel filtering problem in which we can consider a seismogram as a result of alternatively:

- a) Filtering the source inputs for each component of a moment tensor with filters corresponding to the Green's functions.
- b) Filtering the Green's functions with the six independent components of the moment tensor.

It is advantageous sometimes to look at the problem using the second interpretation since, as we pointed out above, we shall probably never know the Green's functions and any information we gain from the seismograms should depend only on the linear transfer function relationships among the various seismograms.

The relationship (5) is too general to be of much use; it cannot be factored in the sense of Equation (3) unless something is known or assumed about the spectral terms and factors in this expression. To see how this equation can lead to (3) and how Equation (4) can be utilized in some applications, we must consider some known facts and special situations. First of all, we know that the moment tensor components generally have a short finite impulse response (FIR), relative to the length of the regional seismograms, since most seismic sources we consider are of short duration. The Fourier transforms of short FIR functions will be denoted with lower case in the following discussion. Secondly, we found by experimenting with Wiener filters of various lengths that the inter-site transformation of waveforms at NORESS could not be efficiently performed using short FIR time domain filters. We know that by reciprocity the displacement of sources of the same order as the NORESS array diameter will destroy waveform similarity if the source region has the same degree of lateral structural heterogeneity as the NORESS site. We also assume for the time being, and will show later by data analyses, that the Green's functions factor into source and site factors for sources and sensors in limited areas. The rest is a straightforward application of linear

system theory to the analyses of single and multi-channel systems of linear systems consisting of short source function FIR filters (Box and Jenkins, 1978) assumed to be driven by "random" Green's functions. In the following, we describe several scenarios of practical significance. Due to the small inter-sensor coherence, we treat the recordings at the various sensors as independent realizations, replications, of the same random process.

We use the term "coherent processing" in this report for techniques that exploit the generalized factorability condition as defined above. This is somewhat different from the usual definition coherent processing techniques, such as beaming and F-K analyses, routinely applied to regional signals at seismic arrays (Mykkeltveit et al, 1983; Ingate et al, 1985; Kwaerna and Mykkeltveit, 1986) which basically depend on the idealized assumption of complete signal similarity. These processes and the regional array layouts were optimized for signals coming from arbitrary directions using the concept of averaged signal coherences vs. sensor distances and are applied only at inter-sensor distances and frequencies where the signal decorrelation due to site effects can be neglected. However, if they satisfy equations of the forms (3) and (4), regional signals across a regional array are much more "coherent," in a more general sense, if we analyze regional arrivals from limited source regions. Let us consider a few special adaptations of Equation (5) to various practical situations.

In the case of a pair of collocated events with different source time functions, but identical source mechanisms and depths, Equation (5) can be rewritten as

$$F_{ij}(\omega) = \left[\sum_{mn} M_{mn} G_{mn}(\omega, r_j) \right] s_i(\omega) \quad (6)$$

This system can, thus, be modeled by two linear systems consisting of two different source time functions driven by identical "random" (Green's function) "inputs," the expression in the

bracket in Equation (6). The only difference between the two sets of seismograms is that a different source time function and the spectra are factorable in the sense of Equation (3), if we ignore the noise term. Since the source locations and depths are assumed to be the same, the G_{mn} will depend only on r_j , the receiver locations, and at each site we shall have another independent realization of the same system. We must note that, contrary to some often expressed beliefs, this does not imply that the waveforms from closely-spaced events will have to be similar or even have high average correlation coefficients between waveforms. It is quite easy to have essentially zero time domain correlation coefficients with a suitable selection of the two source time functions.

A commonly observed phenomenon for numerous quarry blasts is that the spectral modulation is the same for all regional arrivals (Baumgardt and Ziegler, 1988), even as seen at several regional arrays. This situation corresponds to the situation described by Equation (6). This implies a purely temporal modulation, without any spatial structure for the source and identical combination of Green's functions. Without waveform similarity for the individual subevents, no constructive and destructive interference of individual frequency components and spectral modulation could occur. Various scenarios involving combined temporal-spatial shot configurations of shots can easily be simulated and such are being actually applied for vibration control in quarrying operations (Anderson and Stump, 1989).

For this situation, the site functions will be identical for all the events, since the modal makeup of the wavetypes for a given regional phase for collocated events with the same mechanism and depth are expected to be the same. The two outputs will then be coherent, since it will be possible to transform one into the other (at all sensors) with a filter that is essentially s_1/s_2 , or its reciprocal. Except for some degenerate cases, this filter will generally have a short impulse response. The existence of short FIR transfer function implies that one will have a high inter-event coherence

$$C = \frac{|P_{ij}|}{\sqrt{P_{ii} P_{jj}}} \quad (7)$$

between two events i and j , in the case of low background noise.

Central to this idea is the estimation procedure for the power spectral components, P_{ij} . These must be computed by some smoothing procedure, such as smoothing the dot products of the signal Fourier transforms denoted as vectors f , such that

$$P_{ij}(\omega) = \sum_s \overline{f_i(\omega) f_j^*(\omega)} \quad (8)$$

where the overbar denotes spectral smoothing, the star denotes complex conjugation and the summing of smoothed products is performed over sensors. Smoothing can be accomplished in various ways, by actually smoothing the spectra, by averaging over shorter time windows, or some combination of the two. In our case, we use the combination of spectral smoothing and averaging over array sites. The equivalent time-bandwidth product (TBWP) of the result can be computed by multiplying together the spectral averaging bandwidth B , the total time length of the data used for each array site T and the number of array sites N . In any coherence measurement some decision must be made concerning the bandwidth to be used. High TBWP implies high stability of the coherence results; with a given amount of data this can be traded-off against the resolution in spectral detail (Bendat and Piersol, 1966; Shumway, 1988). In the case discussed here, we can assume that the waveform differences are associated with different effective source functions, i.e., firing sequences. As we mentioned before, these generally have very short time durations. The amount of smoothing that can be applied in coherence calculations depends on the time length of the impulse response of the transfer function between the two time-series. As a rule of thumb, one can smooth over a bandwidth of $1/T_i$ where T_i is the duration of such an impulse

response. This implies that heavy spectral smoothing may be applied in the calculation of C above if the differences in waveforms are mostly due to different firing sequences. For further discussions of the particulars of coherence calculations, we refer the reader to Shumway (1988, pp. 70-73).

The second case we consider is that of two or more events with identical source mechanisms and depths, but with larger differences in source location. In this case, the spectra of a regional arrival from these events may be still factorable, as described by the equation

$$F_{ij}(\omega) = \left[\sum_{mn} M_{mn} G_{mn}(\omega, r_j) \right] S_i(\omega, r_i) s_i(\omega) \quad (9)$$

but any pair of events is no longer coherent in the sense of Equations (7) and (8). The inter-event transfer function is no longer characterized by a short FIR filter because of the factor $S_i(\omega)$ now implies the longer FIR filter due to source dislocation (a reciprocal equivalent of array site effects).

In the case of collocated events with different source mechanisms, Equation (5) can be rewritten in yet another form

$$F_{ij}(\omega) = \sum_{mn} m_{mni}(\omega) G_{mn}(\omega, r_j) \quad (10)$$

In this case, the waveforms of individual events will not be coherent in the sense of Equation (6) and (10) is not factorable either. Moreover, the spectra of the superpositions of individual shots with different mechanisms will not be modulated in any easily predictable fashion. A possible scenario of such a situation in quarry blasting is a mix of shots, some of which may be applied to a vertical rock face (shear source) and some buried under a horizontal surface, both kinds of shots

being close to the surface at roughly the same depth but involving the various $G_{ij}(\omega)$ with different weights.

Note that the components of the moment tensors in this equation are written with a lower case to designate the fact that they are short FIR filters. This is a multi-channel filtering scenario and, as long as the six independent Green's functions are common to a set of any seven events, *they will be coherent in the multiple coherence sense*, i.e., we shall be able to reconstruct the waveform of the i -th time series from the rest if all have distinctly different source mechanisms (Bendat and Piersol, 1966).

We believe that this is a worst case scenario, since not all six independent G will contribute significantly to the waveforms and in many cases only a few may be important. In such cases, multiple coherences with lesser number of events may attain relatively high values that are significantly different from zero. Thus, no matter how complex the source mechanisms may be, it will be possible to "calibrate" parts of a quarry with a small number of events and the high multiple coherences will identify all subsequent events which are roughly at the same depth and location within that quarry. In this study we shall not present any multiple coherence results.

The last case is when the events are too far from each other so that the site effects at the same sensors are all different and we are back to the general Equation (5) again. This case is analogous of testing outputs of several different systems with independent random inputs for coherence. These should test as not being significantly different from zero and nothing more can be said about these events. This case also covers all events with different depths. If all G_{mn} are different, then none of the single and multiple coherences between that event and the events at a "calibrated" quarry will be high.

The last case corresponds to the practically important situation from the monitoring point of view when an attempt is made to hide a decoupled, larger explosion among normal quarry blasts, presumably at significantly *different source depths*, in a quarry. In this case, the lack of single or multiple coherence and factorability could be used as a criterion for detecting such suspicious events. Given the fact that decoupled, non-chemical explosions have to be buried deeper than conventional explosives in standard quarrying procedures, and that the effective mechanisms for the two types of events will be no doubt different, it does not seem to be very easy to mix the two types of explosions in order to hide testing.

The advantage of applying simple linear system analysis methods is that one does not need to know the Green's functions or the moment tensor time functions, which are next to impossible to compute with sufficient realism for regional arrivals. We simply test the multi-sensor data, treated as independent realizations of the same processes, for the existence of linear transfer function relationships of various types described above. The types of relationships found can be related to various relative source mechanism and location scenarios. This approach has the advantage that it can employ some simple, standard time-series analysis techniques and, unlike most methods applied to regional arrivals, exploit detailed regional seismic waveform information. Theoretical developments, conceptualizations and observational results of a similar nature, based on linear system theory, were also presented in a forthcoming report by Harris (1989).

***A summary of the diagnostics for grouping of events with respect to location
mechanism and/or source depth***

A short summary of the expected features of various scenarios discussed above is as follows:

- a) Events with very similar or identical waveforms for all regional arrivals - collocated events with closely identical source time functions.

- b) Factorable, inter-event transfer functions can be characterized by relatively short FIR wavelet shaping filters (Robinson, 1967) and these are valid for *several* regional phases, inter-event coherences are high - closely-spaced events with similar source mechanisms and source depths, but different source time functions.
- c) Factorable, but short, FIR filters cannot describe the inter-event transfer functions (low inter-event coherences) - events with similar mechanisms and depths, still grouped tightly, but not very closely spaced.
- d) Not factorable, but high multiple coherences within a larger group of events - closely spaced events with different mechanisms.
- e) Not factorable, low, multiple coherences - any combination of different depths and/or large spatial separations.

Analyses of NORESS Data from Quarry Blasts in Scandinavia

Coherence and cross-filtering analyses

In the following, we shall demonstrate by analyses of actual regional phases that many of the phenomena and properties predicted above are actually exhibited by regional data. Properties, such as spectral factorability for regional arrivals, cannot be taken for granted just on the basis of theoretical speculations such as those presented above. We were pleasantly surprised to find that many of our expectations were confirmed despite the extremely complex nature of regional phases and the crustal structures through which they propagate.

Our data came from NORESS recordings of events, listed in Tables I and II, identified as quarry blasts at the Titania mine and various Estonian mines named E1, E4 and E9. We have also looked at one event at the Blasjo dam site. We do not know about the location accuracy of these

events or the reasons, other than location, for their association with any particular mine. The general locations of the events analyzed are shown in Figure 4.

In order to apply any of the ideas above, we must first verify the applicability of the factorability condition for any data set. We have applied the multi-channel factorization technique described by Shumway and Der (1985) and Der et al (1987; 1990) to two data sets, the Pn arrivals from this group of Titania mine blasts and the Lg arrivals from a set of mine blasts at various Estonian mines. The decomposition of data into source and site factors is, of course, not unique (see Der et al, 1987), but this is not a major concern here. We merely want to test for the existence of factorability, one of our diagnostics for source scenarios, by reconstructing the complete set of original waveforms from the much smaller set of estimated source and site spectral factors and comparing the result to the original data. High similarity verifies that the data has the spectral structure described by Equation (3). Figures 5 and 6 show some representative time domain examples of these reconstructions for Pn from quarry blasts at the Titania mine and Lg phases from the Estonian E4 mine, respectively. All of these have similar qualities within each set (showing whole data sets would simply not be practical because of the large number of traces involved). Typically, the correlation coefficients between the pairs of original and reconstructed traces were near or above 0.8, which is not as good as in the teleseismic cases for P waves, but still respectable, considering the high signal frequencies, up to 15 Hz, we utilized here and the high degree of crustal heterogeneity at the wavelengths involved and the fact that the recordings were not noise-free. Note that the waveforms are quite different at the various sensors for the same event and for the various events at the same sensors. Joint factorization of the Titania events and the Blasjo event did not result in acceptable reconstructions, showing that an azimuth difference of 10° is too large for using the same site factors. In all the work we present in this report, we have

TABLE I: List of "Titania" Events

<u>Event</u>	<u>Date</u>	<u>Origin Time</u>	<u>Latitude</u>	<u>Longitude</u>	<u>Magnitude</u>
Titania 1	14 Feb 86	14:13:24.9	58.3	6.4	2.7
Titania 2	14 Feb 86*	17:54:10.6	58.3	6.4	2.3
Titania 3	07 Jan 86	14:14:28.9	58.3	6.4	2.2
Titania 4	17 Jan 86#	14:11:01.5	58.3	6.4	2.7

* Probably removed from or not at the same part of quarry.

Reference event (unmodulated).

TABLE II: List of "Estonia" Events

<u>Event</u>	<u>Date</u>	<u>Origin Time</u>	<u>Latitude</u>	<u>Longitude</u>	<u>Magnitude</u>
E4-1	19 Jan 88	11:55:35.0	59.3	27.2	2.5
E4-2	20 Jan 88	12:23:06.0	59.3	27.2	2.5
E4-3	21 Jan 88	11:25:30.0	59.3	27.2	2.4
E4-4	26 Jan 88	09:55:37.0	59.3	27.2	2.4
E1-1	19 Jan 88	11:50:50.0	59.3	24.4	2.5
E1-2	21 Jan 88	12:53:23.0	59.3	24.4	2.2

Location of the quarries

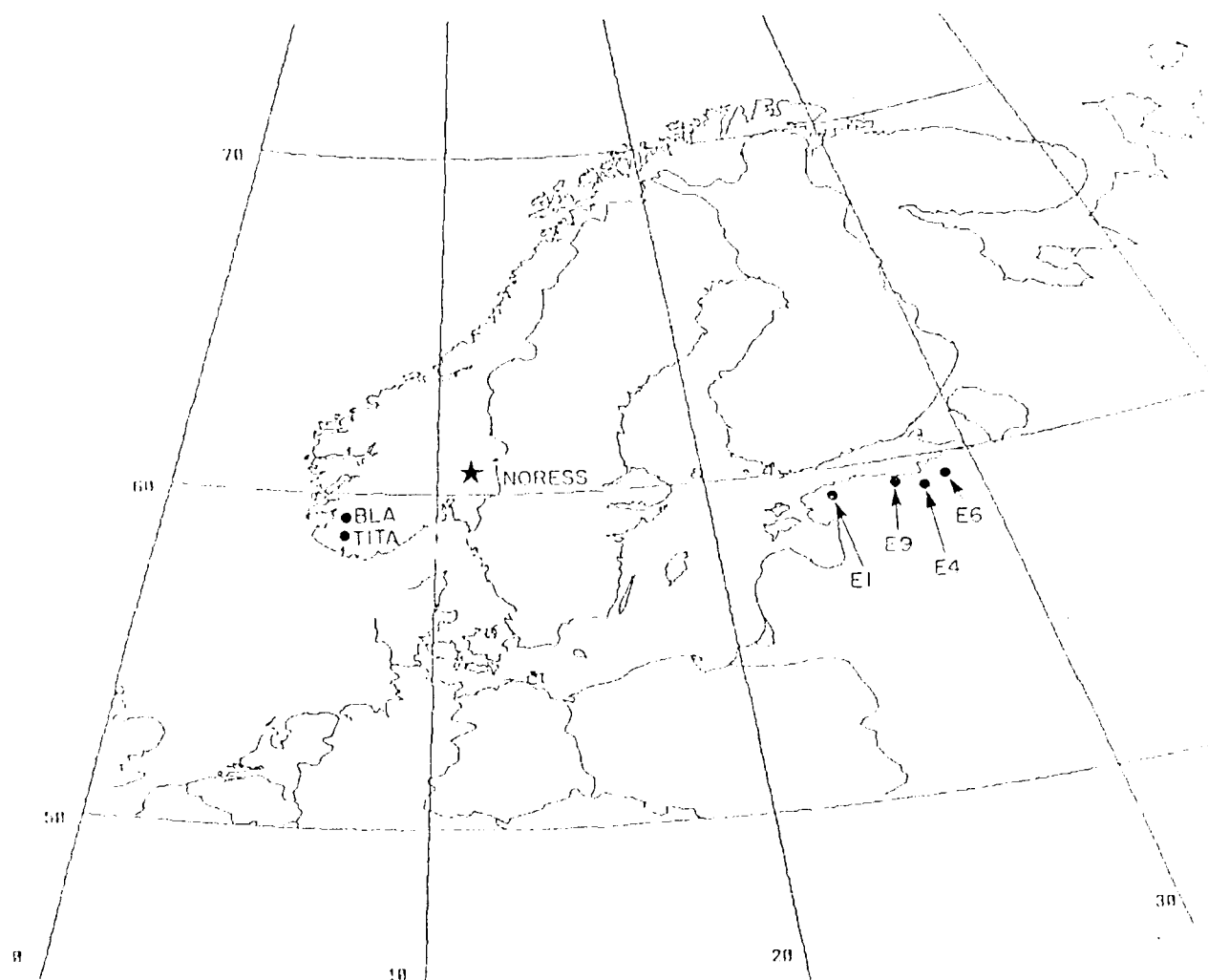


FIGURE 4: Map of Scandinavia with the location of NORESS and Titania, Blasjo and the Estonian mines studied.

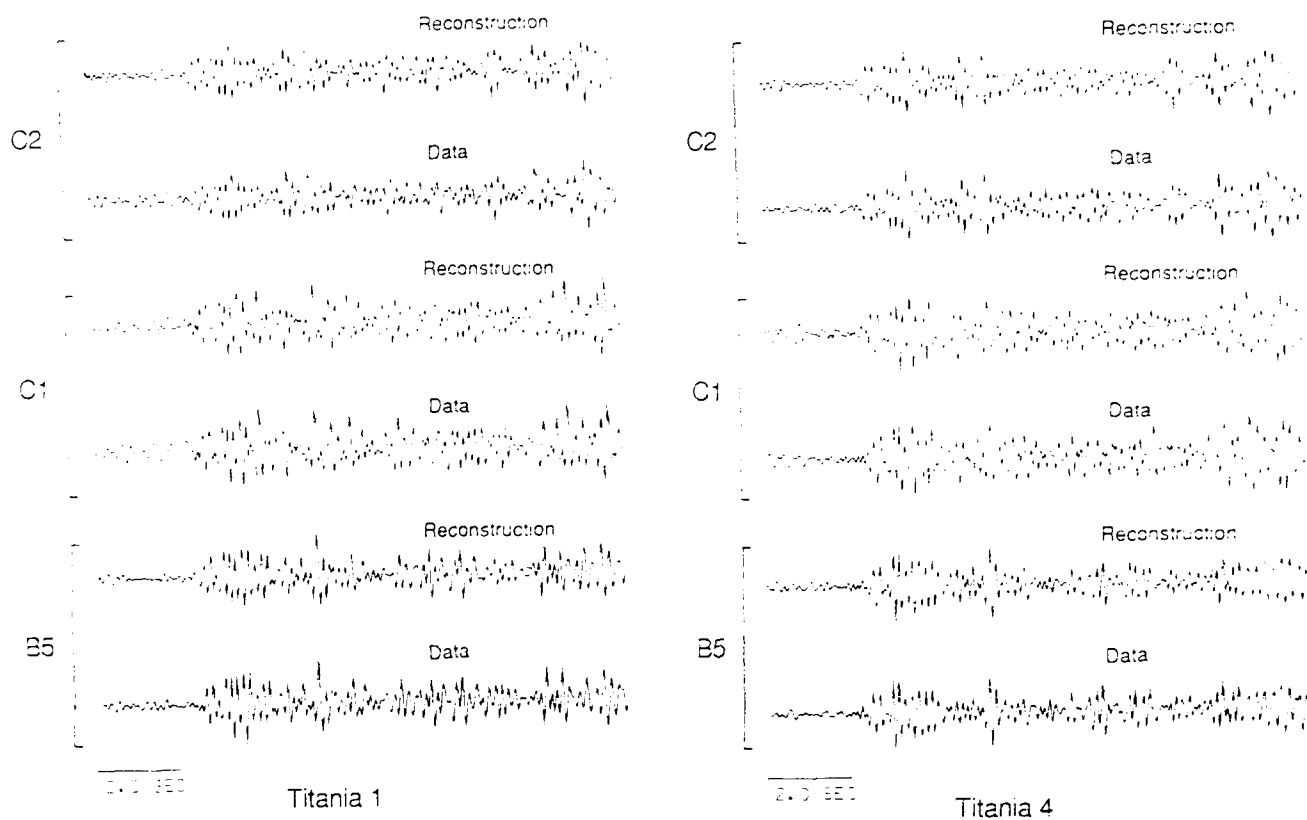


FIGURE 5: a) Selected reconstructed and data traces of Pn arrivals from the Titania1 event. b) The same for the Titania4 event. The designation C2 refers to the second sensor in the C ring of NORESS, etc.

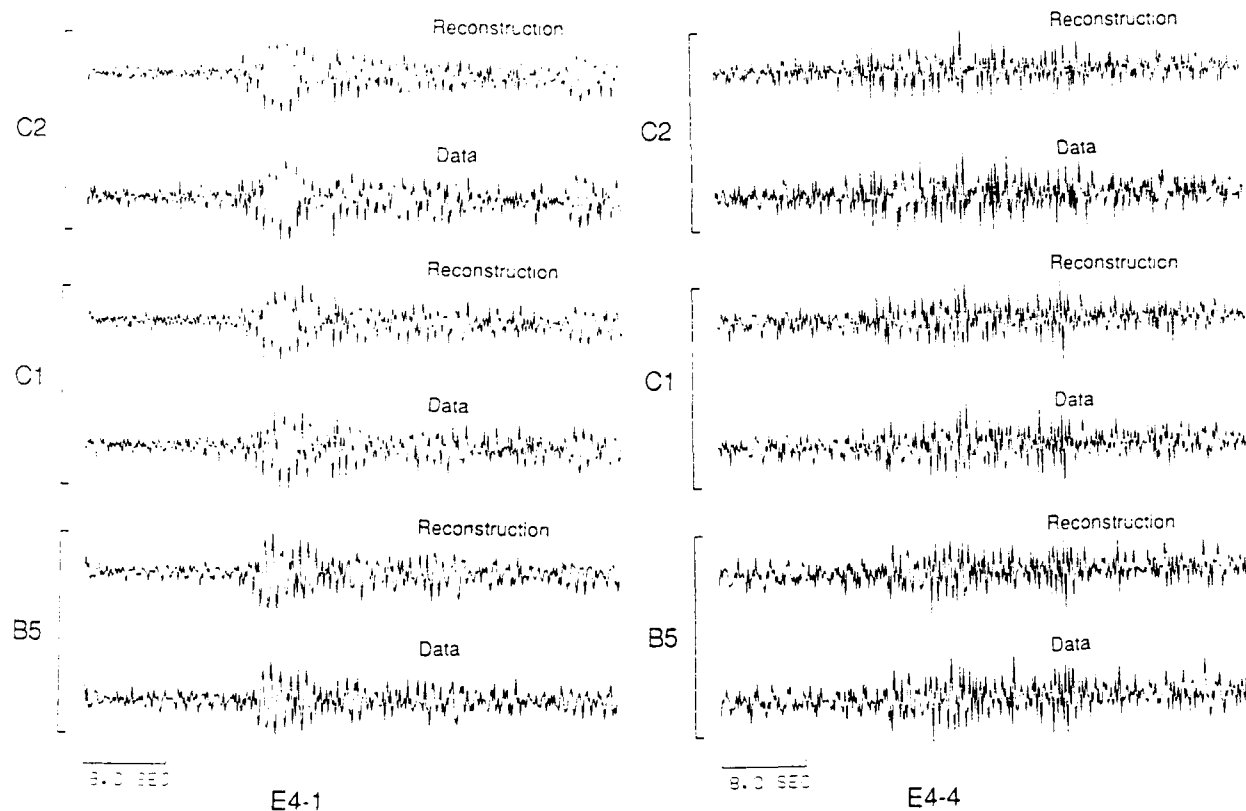


FIGURE 6: a) Selected reconstructed and data traces of Lg arrivals from the E4-1 event. b) The same for the E4-4 event. The designation C2 refers to the second sensor in the C ring of NORESS, etc.

used 12 sensors of NORESS chosen such that they were roughly evenly distributed over the area of the array.

In Figure 18, we show some factoring results in terms of coherences for a group of FENNOLORA shots at NORSAR subarray 3C. The efficiency of factoring at this subarray with 5 km sensor spacing indicates that regional arrays *larger than NORESS* may be effective when the more general concept of signal coherence, implied by Equation (3), is applied. For instance, site-equalization filtering could be applied at such arrays prior to beaming or optimum filtering, thus leading to better estimation of source characteristics.

Starting with the Pn data from the Titania mine, let us assume initially that all these events had the same source mechanism and/or location and test the idea that the differences in waveforms are totally attributable to differences in source functions $s_i(\omega)$ implied in the firing sequences (Equation 6). Inspecting the spectra of mine blasts from the Titania mine in Norway at NORESS, it can be observed that regional phases from some of these events are strongly modulated, while spectra of some others are quite smooth (Figure 7). These modulation features are similar for all phases, *Pn*, *Pg*, *Sn* and *Lg*. This points to a common, *temporal* modulation for each event, rather than to a pattern imposed by the spatial configuration of charges, since in the latter case we should see different modulation patterns for the various regional phases which possess notably different phase velocities. Although the lack of modulation does not rule out some very complex spatio-temporal modulation patterns of the source (although these must be quite unlikely), such that the spectral manifestations of it are suppressed, it is reasonable to assume that the spectrally unmodulated quarry blasts have simple impulsive source time functions or very small delays while the modulated ones have been ripple-fired.

Let us compute now the inter-event coherences according to equations (5) and (6) above, summing the smoothed auto- and cross-spectral estimates over sites only, for Pn phases from

several pairs of these events including the relatively unmodulated one. The results show (Figure 8) that the pairs Titania4-1 and Titania4-3 have relatively high average coherences, indicating nearly identical source mechanism and/or location, while the pair Titania4-2 has lower coherence, indicating that event Titania3 has probably a different mechanism or location. Although the S/N ratio was the also the lowest for Event 2, this coherence still seems to be still too low for a coherent signal. The TBWP for these coherences was at least 120.

Let us hypothesize now that the unmodulated event Titania4 is a simple one, a single shot. Consequently, the time domain impulse response of the moving average (MA) filter that can

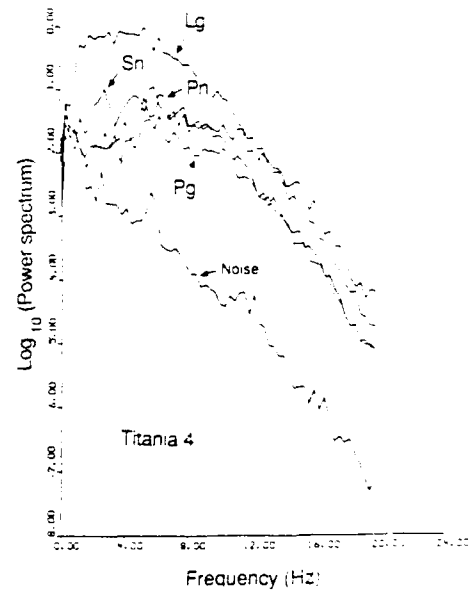
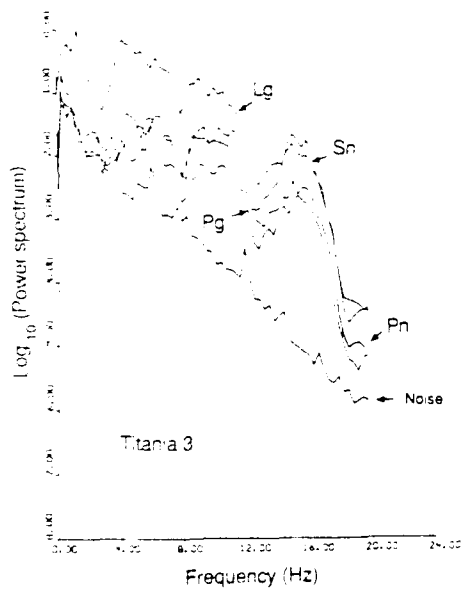
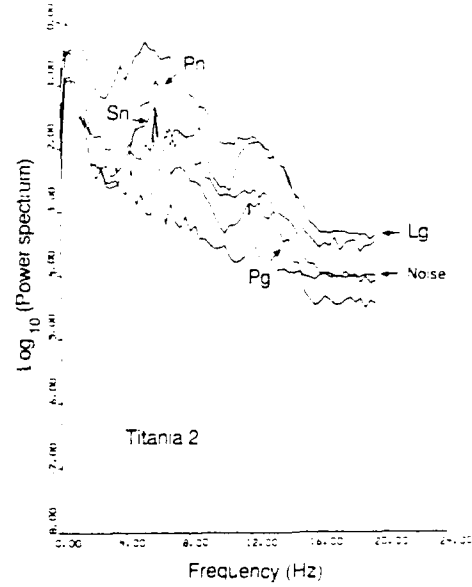
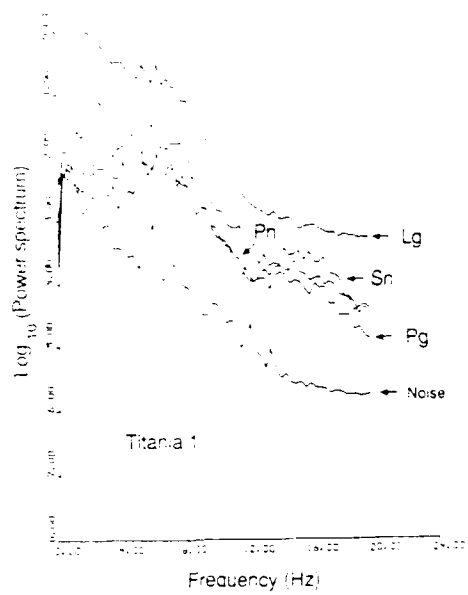


FIGURE 7: Spectra for various regional arrivals from the Titania mine. Note that the spectral modulation is similar, regardless of the type of arrival.

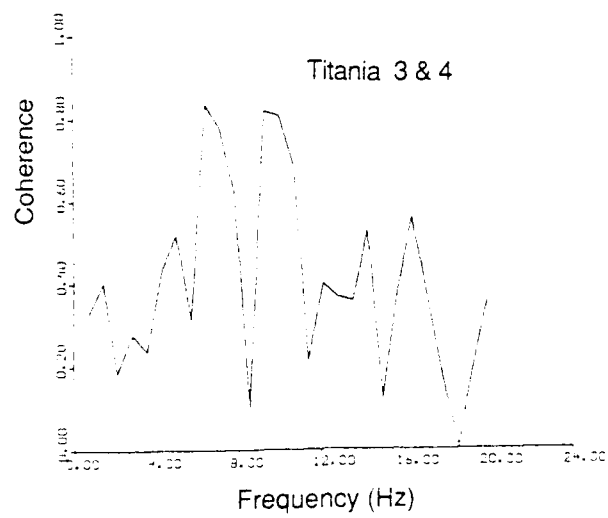
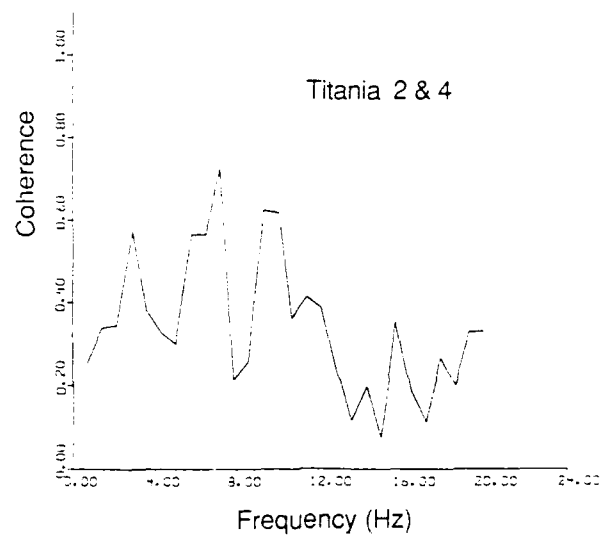
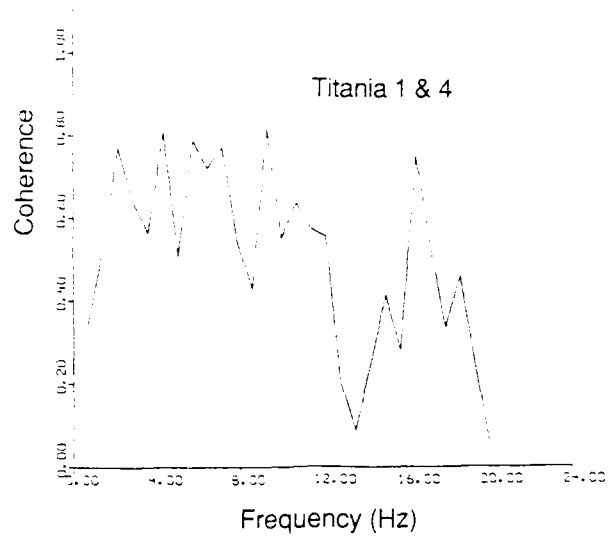


FIGURE 8: Inter-event coherences for Pn arrivals from the Titania mine.

transform the waveforms of this event to those of the Titania1 must be a band-limited representation of the firing sequence. Therefore, we designed a Wiener filter to transform P_n waveforms of event Titania4 into those of event Titania1 at all sensors of NORESS. Prior to applying this technique, we wanted to ensure that the traces processed are as free as possible from background noise and other distortions of the spectrum by applying a common, minimum phase band-pass filter to all traces of both events that emphasized the energy and flattened the spectra in the 3 - 15 Hz frequency band where the signal-to-noise ratio was higher.

Computation of time-domain MA type filters can be easily accomplished by several well-known algorithms, using computer codes widely available (Marple, 1987). Time domain design is convenient because we want to limit the length of the filter. The P_n arrivals were lined up for both events, windowed and tapered, and the auto- and cross-correlation functions needed by the filter design algorithms were computed by ensemble-averaging these correlation functions over sites. The ensemble-averaging process of correlation functions over common sites suppresses the effects of the site functions and much reduces those of the ambient noise. The length of the portion of the cross-correlation function with highest amplitude gave a good indication of the maximum length of the ripple-firing sequence, since the time length of the large amplitudes in this function cannot exceed this length. For the cases discussed, this upper limit is roughly of the order of .5 seconds. The compound correlation functions constitute the inputs to the Levinson algorithm used for the computation of the cross-equalizing Wiener filter, consisting of 31 weights.

Subsequently, the filter was applied to the simple event to derive waveforms of the complex events at all sites. A set of traces showing the representative improvement between the two events at common sensors are shown in Figure 9. [Note that the original waveforms are much different for the two events and waveforms became more similar.] Nevertheless, the increase in the time domain correlation coefficients was only modest, from 0.59 to 0.75 for the first pair, and 0.49 to 0.57 for the second. This indicates that either we need a longer filter or that the event pairs

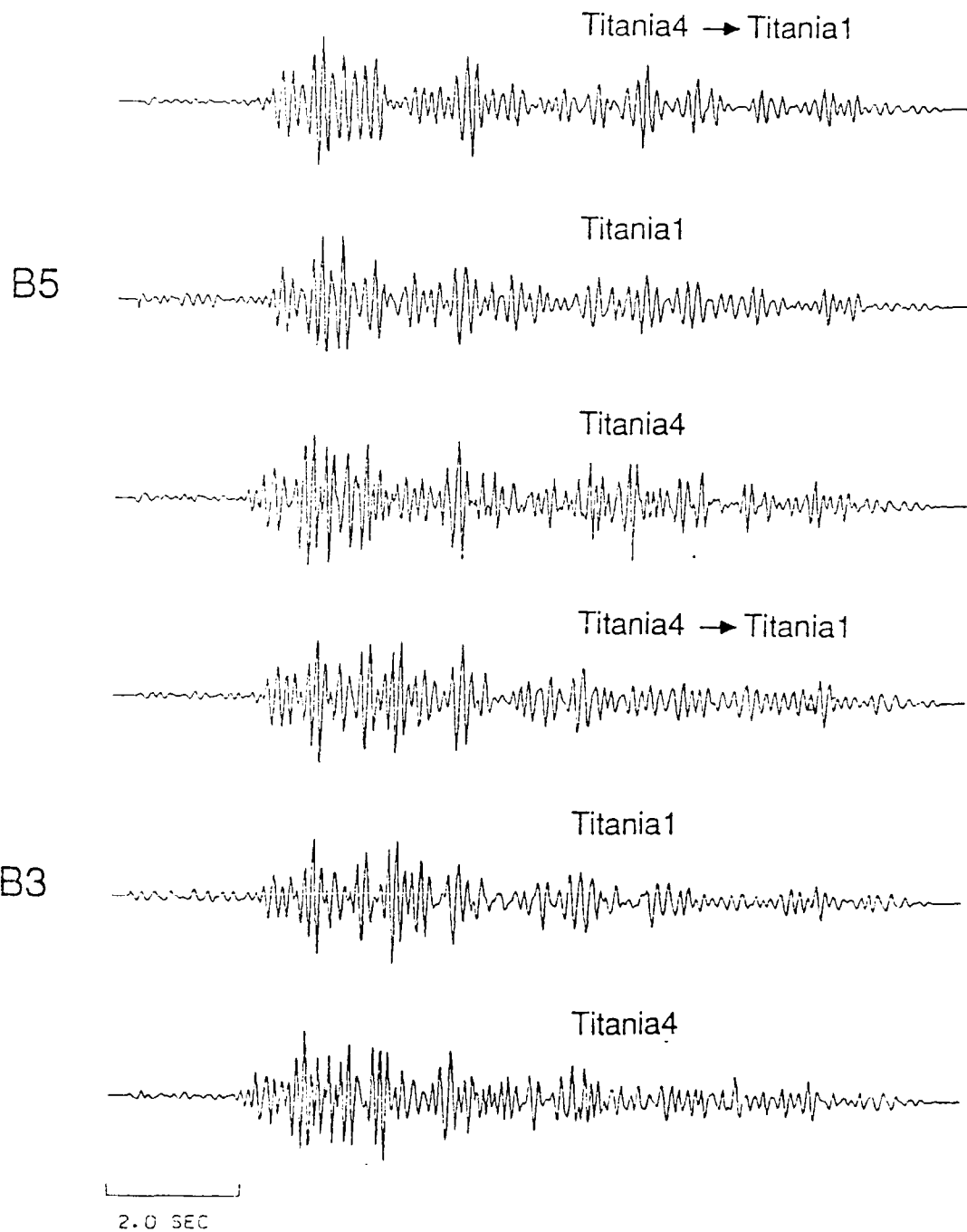


FIGURE 9: a) Wiener filtering results for transforming Event Titania4 into Event Titania1.

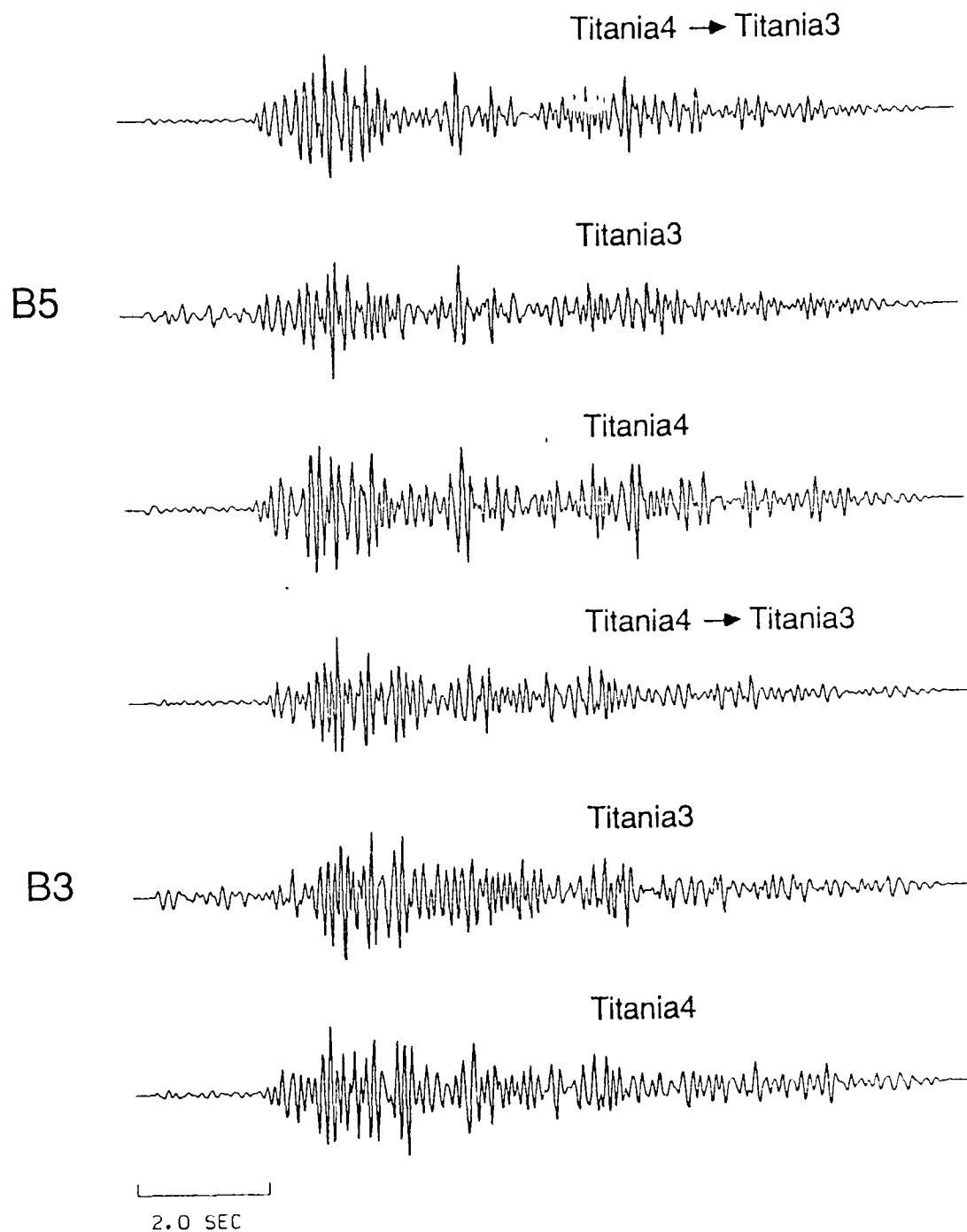


FIGURE 9: b) Wiener filtering results for transforming Event Titania4 into Event Titania3.

are too far from each other and, thus, we cannot attribute the waveform difference entirely to the source time functions. The same method did not work at all for the pair Titania4-2.

We have also applied the cross-equalization for the *whole wavetrains*, consisting of all the regional arrivals of events Titania4-1. The processing resulted in a spectacular increase of the correlation coefficients between the two events from .08 to .65 over the whole set of sensors, again confirming that the waveforms of these events are closely related.

Having established that such techniques may be suitable to identify groups of events with nearly identical mechanisms and/or locations, we examined the nature of the relative inter-site transfer functions for the same event. We know from spectral factorization that such transfer functions exist, and they are consistent event to event. Otherwise, we would not have been able to jointly deconvolve and reconstruct all these events. It would be desirable if these transfer functions would be simple, similarly to the inter-event transfer functions for the coherent event pair, because then relative displacement over distances of the order of the NORESS diameter would not destroy the inter-event coherence (applying the principles of reciprocity). In that case, the lack of coherence among events in a limited source region observed at an array would be mostly due to differences in source mechanisms.

Unfortunately, this is not the case. We have tried to design short, 31 point, time domain filters for equalizing Pn waveforms at sensors D1 and D5 for the suite of four events, but they essentially failed to produce even remotely similar waveforms. Thus, the inter-site transfer functions are generally complex, even over the small NORESS diameter, with very long time domain impulse responses. Applying the reciprocity argument, this implies that a comparably small displacement in the location of a source would destroy the waveform similarity, assuming that the source region and the NORESS site are similar in the degree of structural heterogeneity.

Site equalization processing

A major problem in locating regional events is that the first arrivals are often small and buried in noise and that most phases are emergent, without clearly defined arrival times. Azimuths estimated from F-K analyses are often not very accurate, since the site effects tend to destroy the plane wave character of the signals, thus broadening the main lobes of array response patterns. There are conflicting demands of keeping the array apertures small for ensuring signal similarity and increasing the directional resolution of the arrays. The fact that the site transfer functions are consistent, albeit not simple, still leaves open the possibility of utilizing this internal consistency for refining the estimation of *relative* azimuths among closely spaced events. If the forms of the inter-site transfer functions do not change much with small azimuth changes, except for some small time shifts, then such a property could be exploited. To test this idea we have band-pass filtered the four Titania events to emphasize the band with the maximum signal-to-noise ratio, between 3-10 Hz. Subsequently, we have taken the frequency domain site factors derived from the multi-channel deconvolution calculations and multiplied the Fourier transform of trace D1 with the site factor of D5 and vice versa. This is basically an intercorrelation technique applied to the broadband site (rather than event) equalization. The resulting spectra were then correlated in the frequency domain and transformed back into the time domain

$$\Phi(t) = F^{-1} \left| d_1(\omega) R_5(\omega) (d_5(\omega) R_1(\omega))^* \right| \quad (9)$$

to view the cross-correlation function. In this expression, the d's are the Fourier transforms of the traces and the R's are the site transfer functions. The results for three of the events are shown in Figures 7 and 8. Event 2 was too noisy. In inspecting these figures, we must point out that the results of cross-equalization do not have to look like normal seismograms, with clearly defined phases. In multiplying with the complex site factors we essentially perform a circular convolution with considerable wraparound effect. It is interesting to note that the correlation peak for event

Titania4 is not lined up with those of Titania3 and Titania1 (Figure 10), indicating the possibility of a small time shift. Figure 11 demonstrates that the site-equalized trace waveforms indeed became quite similar. The shift in the peak does not seem to be associated with noise or mismatch, since all cross-correlation functions for this set of events have a well-defined, single maximum with little ambiguity in value of the time shift.

The same process was repeated with the recordings of Lg phases from quarry blasts in Estonia as recorded at NORESS. The Lg phases of the Estonia mine blasts are somewhat noisy and the S/N ratio is only good below 6 Hz; the rest of the phases are buried deeper in noise than those for the Titania mines. Applying the process to four E4 mine events, we obtained good trace equalizations, with all correlation peaks lined up at zero lag (Figure 12). Using four events from E4 and two from E1 mines in a joint site-equalization process, we have found that the efficiency of the inter-site equalization drastically deteriorated, as indicated by the decrease in the correlation coefficients between equalized traces (Figure 13, left side). The correlation peaks are still generally at the same times, but one of the peaks (for event E1-2) is shifted in time. The decrease in site-equalization efficiency may be attributed to the fact that mines E4 and E1 are too far from each other to have identical site functions at NORESS. The waveform similarity is not even visible for this set (Figure 13, right side).

Given the fact that after applying some cross-equalization treatment to the outputs of a pair of sensors located at the extremities of a small array for events in some limited source areas (not the two Estonia mines together), the waveforms become quite similar, it may not be justifiable to limit the sizes of regional arrays to a few kilometers. It appears that regional signals from limited source regions are actually "coherent," in the sense of a broader definition of this term, over much larger

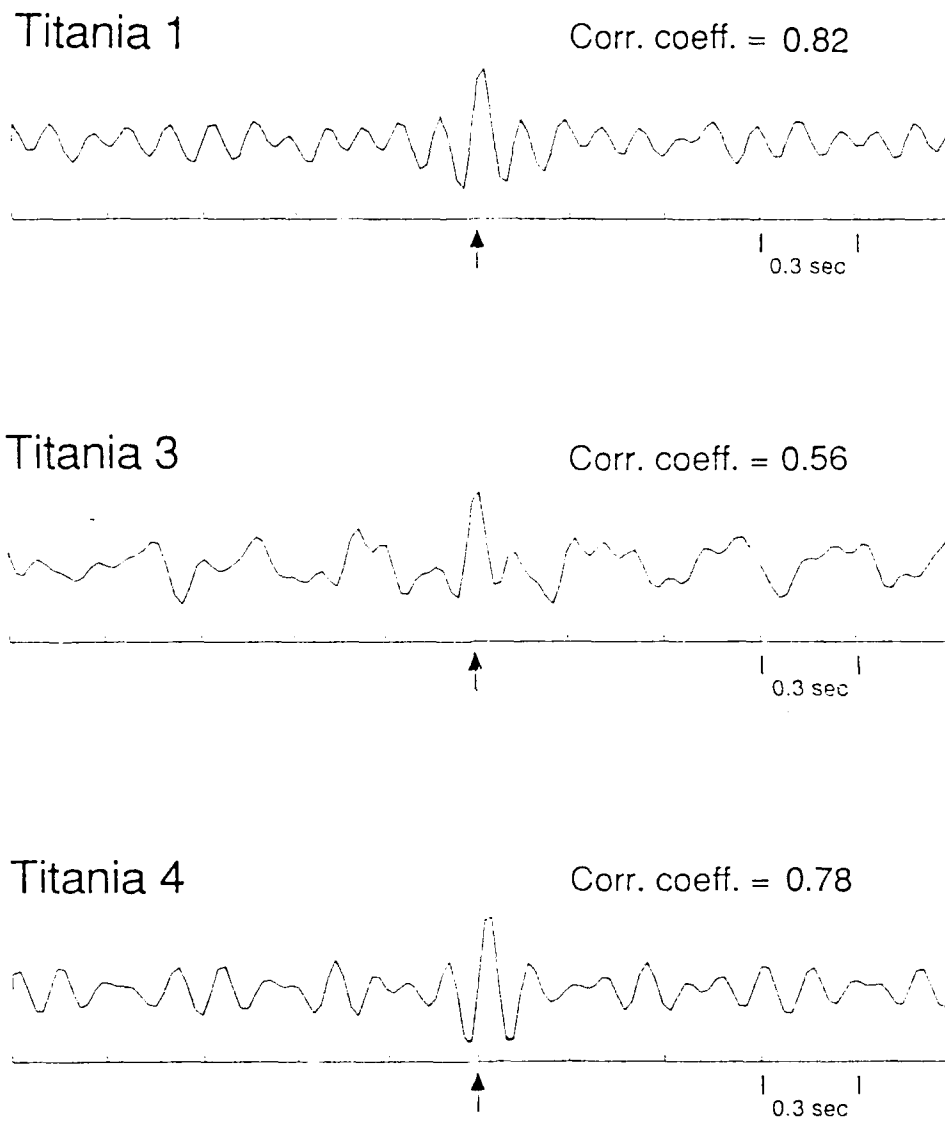


FIGURE 10: Cross-correlations of the site-equalized traces of Pn between sensors D1 and D5 for selected Titania events.

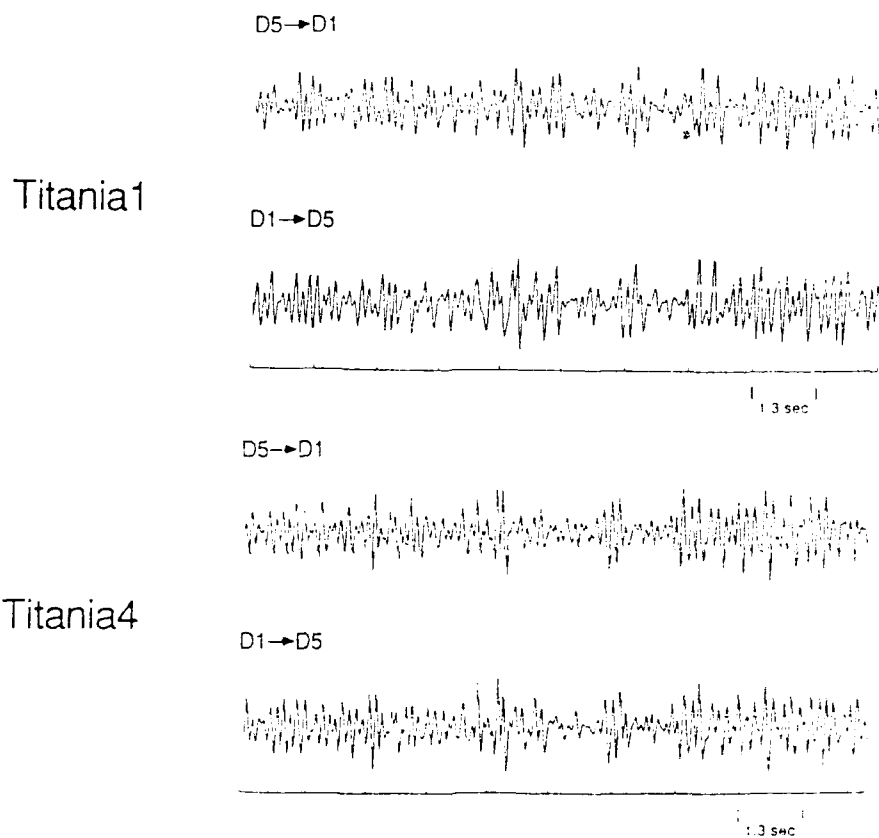
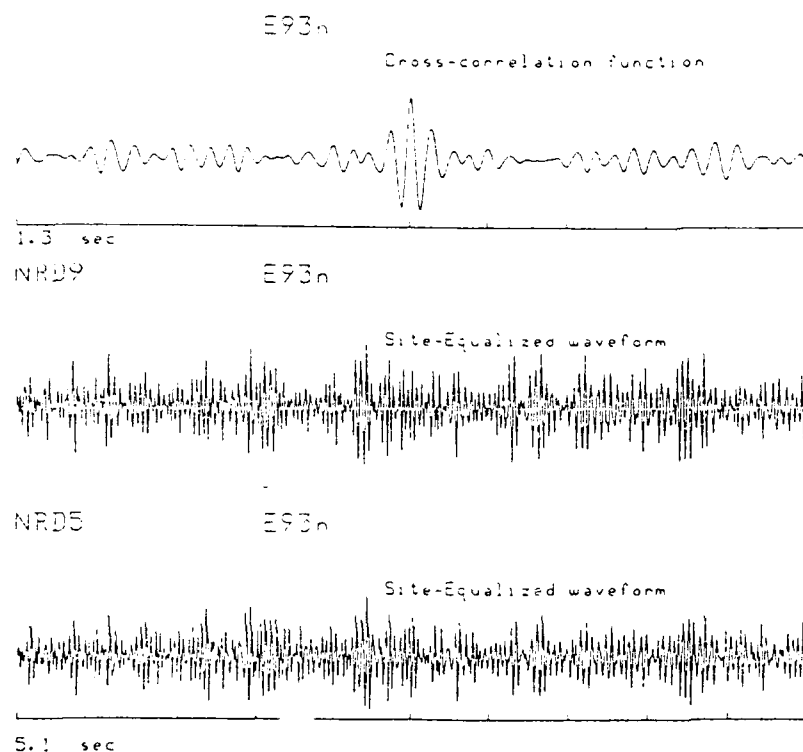


FIGURE 11: Site-equalized Pn traces for selected Titania events between sensors D1 and D5.



**Site-equalization
results for Lg
from the
Estonian mine
blast E93**

**Cross-correlation
function
&
Site-equalized trace
pair**

**Correlation coefficient
= 0.9**

FIGURE 12: Cross-correlation of the site-equalized traces and the equalized traces of Lg between sensors D1 and D5 for the E9 Event. Note the excellent similarity between the cross-equalized traces.

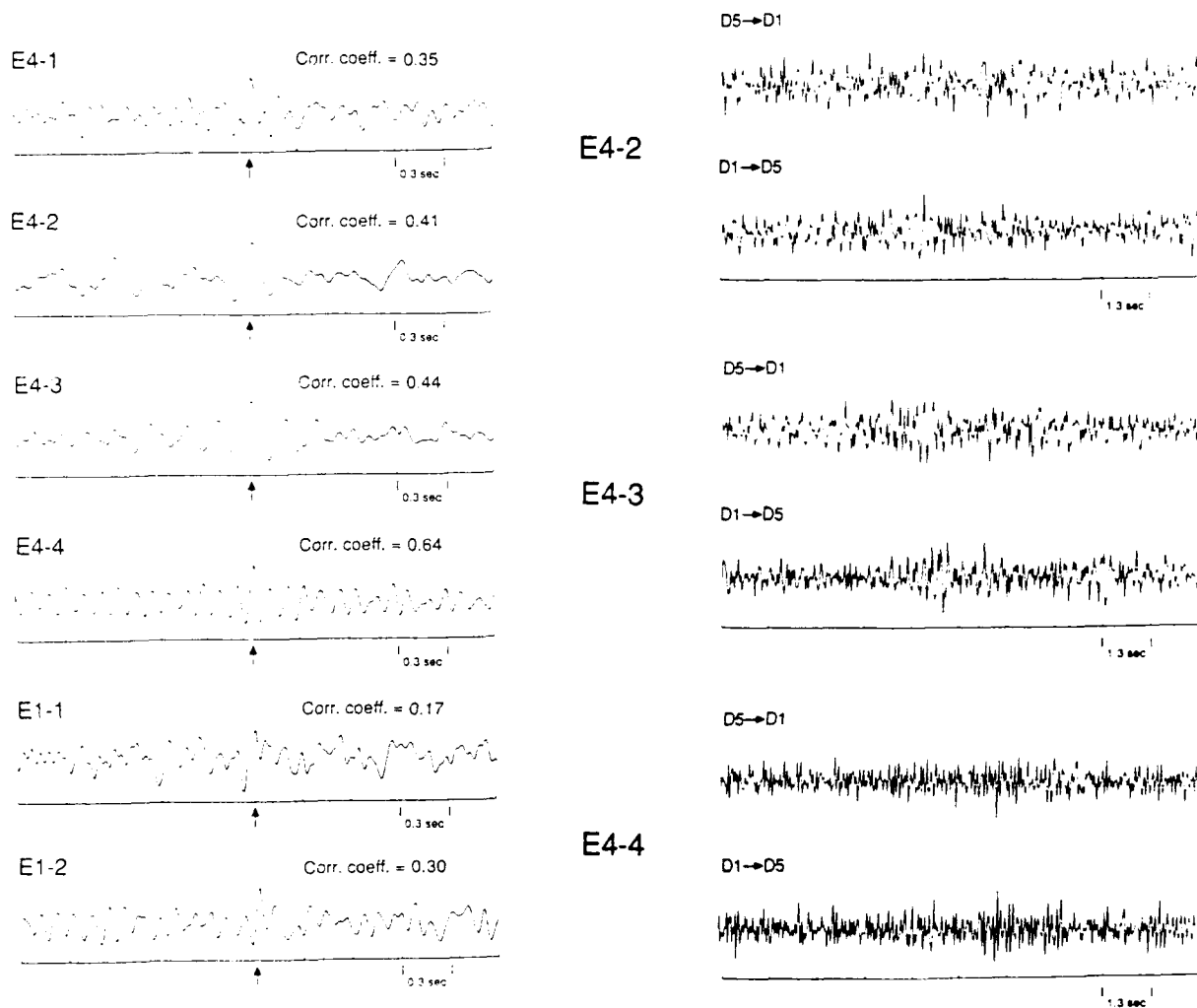


FIGURE 13: Results of site-equalization when spectral factors from joint factorization of E1 and E4 Events were utilized. Although the cross-correlations still have peaks at the proper alignment with reduced correlation coefficients, (a) the efficiency of site-equalization is greatly degraded as evidenced by the poor similarity of the site-equalized traces (b).

distances between sensors. Clearly, the maximum array diameters dictated by the average waveform correlation properties (Mykkeltveit et al, 1983; Der et al, 1988) do not apply here. It could be fruitful to test and develop similar techniques using data from small arrays larger than NORESS.

Factorizability studies and coherence grouping of Estonian mine blasts

Thus far, we have only presented various time domain results using inter-event and inter-site filtering and factorization, demonstrating that there exists a remarkable degree of coherency in the detailed waveforms of regional Pg and Lg arrivals. In the following, we test the effectiveness of spectral factorization for Lg phases from Estonian mine blasts by measuring the efficiency of reconstructions of data from the estimated site and event factors for various groupings of these events. After factoring and reconstructing the waveforms of various groups of events, we compute the coherence measure (4) between the data and reconstructions for each event, using the data for all sensors in the 2-6 Hz band where the S/N ratio was the best summing only over sites. The S/N ratios for the chosen events were such that, in this frequency band, (4) should have resulted in coherences of at least 0.9, had the factoring on the signal part been effective for all events. The statistic measures the similarity of the reconstructions vs. the original data. We are not interested in either the source or site factors themselves, which we have no way to interpret, only in the efficiency of the factorability. It is expected that events with identical site factors (similar Lg modal compositions - hence similar mechanisms and depths) will factor efficiently. The converse is also true, events with markedly different mechanisms, depth and location will not factor well when grouped with those that are close in these parameters.

We found examples that confirm types of behavior that we expect on physical-theoretical grounds. In Figure 14, we show a set of coherences computed with equation (4) summing over sites only for any given event, for four events, three at the E9 mine and one at the E4 mine. The

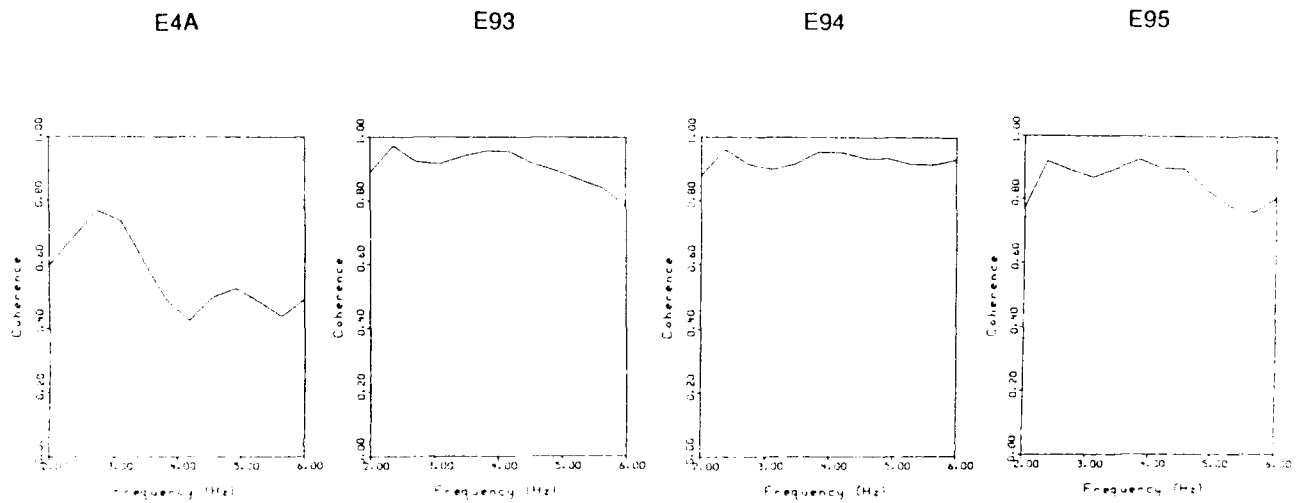


FIGURE 14: Site-averaged coherence results from the joint factorization of three E9 events and one E4 event.

E4 mine is only about 0.2 degrees off in azimuth at NORESS, but is 110 km distant from the E9 mine. The coherence for the E4 mine, when factored with the three E9 events, is visibly less than for the E9 group. Apparently, the site effects for this event are different, possibly because of the differences in the nature of Lg wavetrain. This example shows that, in spite of the very small difference in azimuth that could not possibly have been resolved from the Lg by the NORESS array (Harris, 1990), we can show that something is different about this event utilizing its Lg phase alone. This case has limited practical significance, since we could locate this blast at a different mine from other sources.

A more interesting observation is that not all Lg phases from quarry blasts that were listed to have been fired at the E9 mine factor efficiently when grouped together. We have found two factorable groups. Figure 15 shows the factorization efficiency results for three E9 events from one of the groups (on the right) factored with one from the other group (left). The figure shows that there is something different about this event on the left and that the coherence, instead of being near 0.9 as expected based on the prior estimate of the S/N ratio, is closer to 0.6. In order to find what is different between the two groups we went back, after the fact of their discovery, to examine the bandpass-filtered trace envelopes for all the E9 events. We have found that with regard to the envelope shapes of Lg, they also fall into two subtly different groups (Figures 16 and 17). For Type 1 (corresponding to coherence diagrams on the right in Figures 16 and 17), the Lg reaches a maximum suddenly and decreases gradually, while for Type 2, it has a gradual beginning and reaches the maximum later. The timing of the discernable phases does not seem to be different, thus agreeing with the idea that they were at the same mine. The first impression was that it may be a difference in the signal-to-noise ratios that could cause the differences in the coherences. Indeed, the Type I as a group is less noisy. But if we compare the S/N in Lg for events in Type II and E95, they are not much different. This points to the alternative interpretation that the modal compositions of the Lg phases in the two groups were different (and thus, their

mechanisms). The other possibility that the events were mislocated cannot be ruled out either, since this occurs occasionally.

The question of optimum array size for regional events was touched on previously. An interesting observation concerning the factorization of Pn phases is shown in Figure 18. These are coherence results (site- and event-averaged) for a group of closely spaced FENNOLORA profiling shots at the 3C subarray of NORSAR. Given the large spacing of these sensors (~5 km), this shows that the waveforms of these events are "coherent" in a wider sense.

These results show that simple joint analyses of waveforms of regional arrivals from groups of events can potentially be quite useful for ascertaining what activities take place within small source regions and that evasion attempts may be detectable. What is needed in the future is to obtain some "ground truth" regarding operations in the quarries from which recordings of seismic waves are available and verify our theoretical expectations. Such information is now being collected for the Scandinavian area (S. Mykkeltveit, personal communication) and should be utilized in future studies of this type.

Our work during the last two years demonstrated that the expected properties described above are indeed exhibited by real data. In particular, the factorability concept, a key feature for the kinds of analyses we propose, is valid for the Pn and Lg phases recorded at regional distances at NORESS, as evidenced by comparisons of some reconstructed waveforms with actual Pn and Lg phases in Figure 2. We have also found that Pn waveforms of some event pairs at the Titania mine can be transformed into each other simultaneously at all sensors with simple common short FIR filters (Figure 3). For the same event pair a single short filter designed from the whole seismogram increased the waveform similarity, expressed in terms of the site-averaged correlation coefficient from 0.04 to near 0.7, the whole set of arrivals. For other event pairs, this could not be

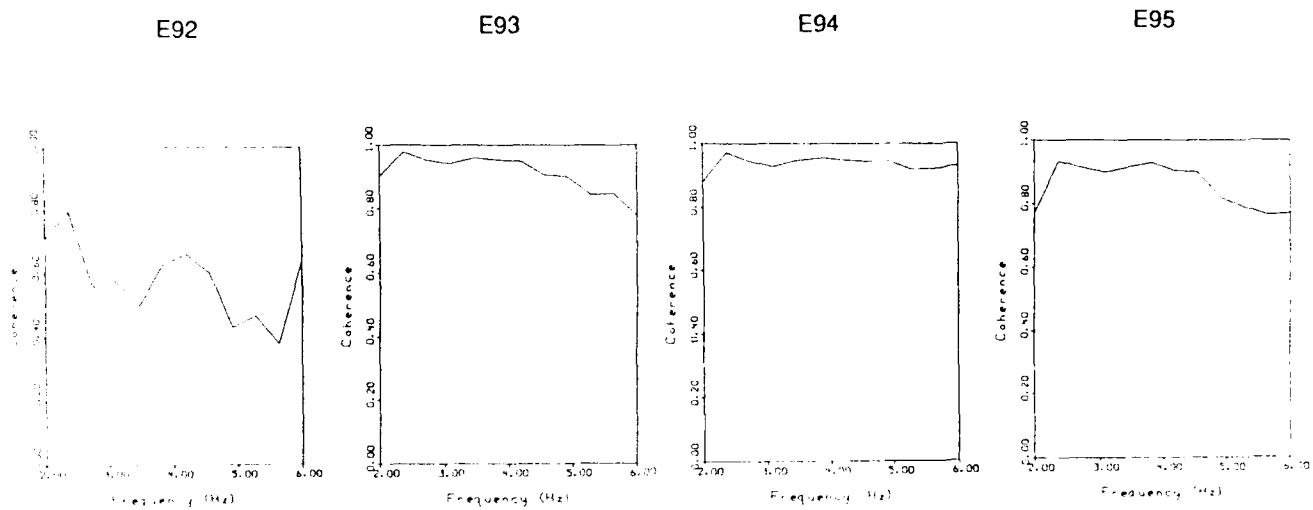


FIGURE 15: Site-averaged coherence results from the joint factorization of four E9 events with reconstructions of one event being much less similar to the original data than the others.

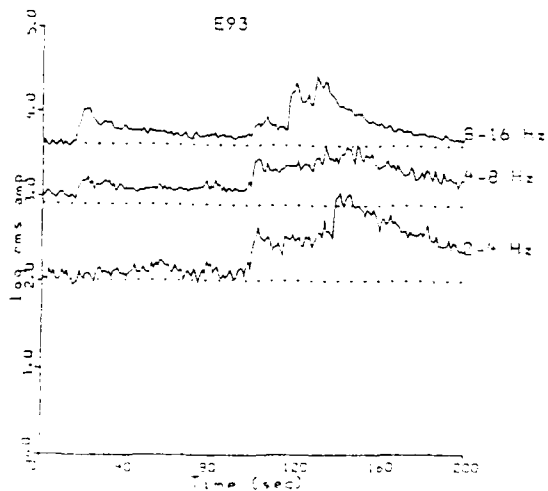
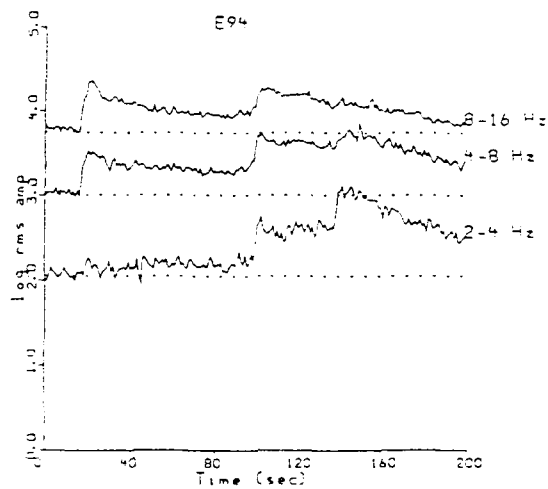
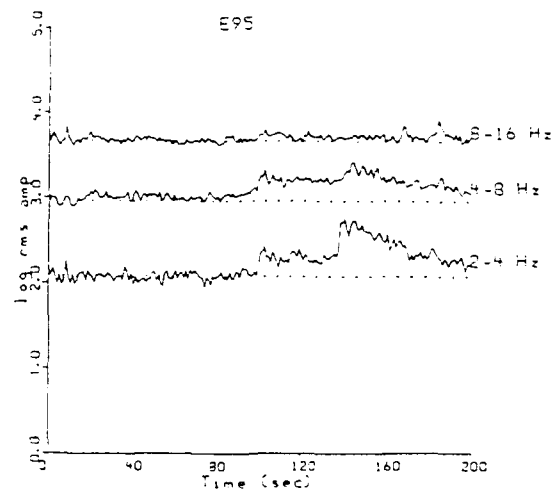


FIGURE 16: Envelopes of band-pass filtered traces Type I of E9 Event.

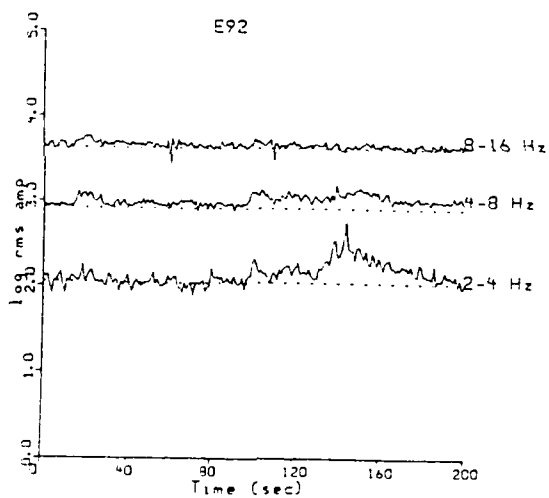
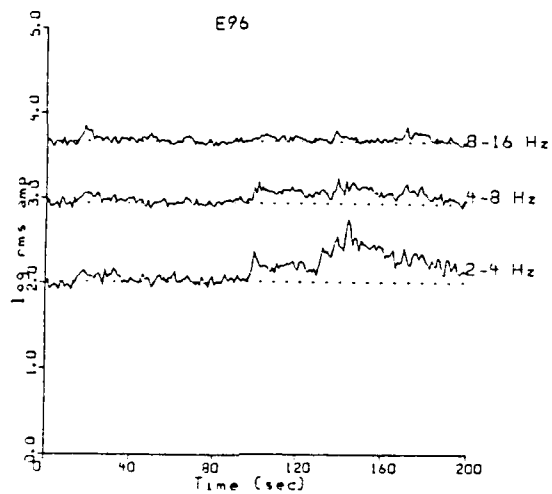


FIGURE 17: Envelopes of band-pass filtered traces Type II of Event E9. Even though these events seem to be noisier than those of Figure 16, the S/N ratio for Lg for these events is about the same as for E9.

FENNOLORA shot group D

6 sensors

4 shots

DOF=224

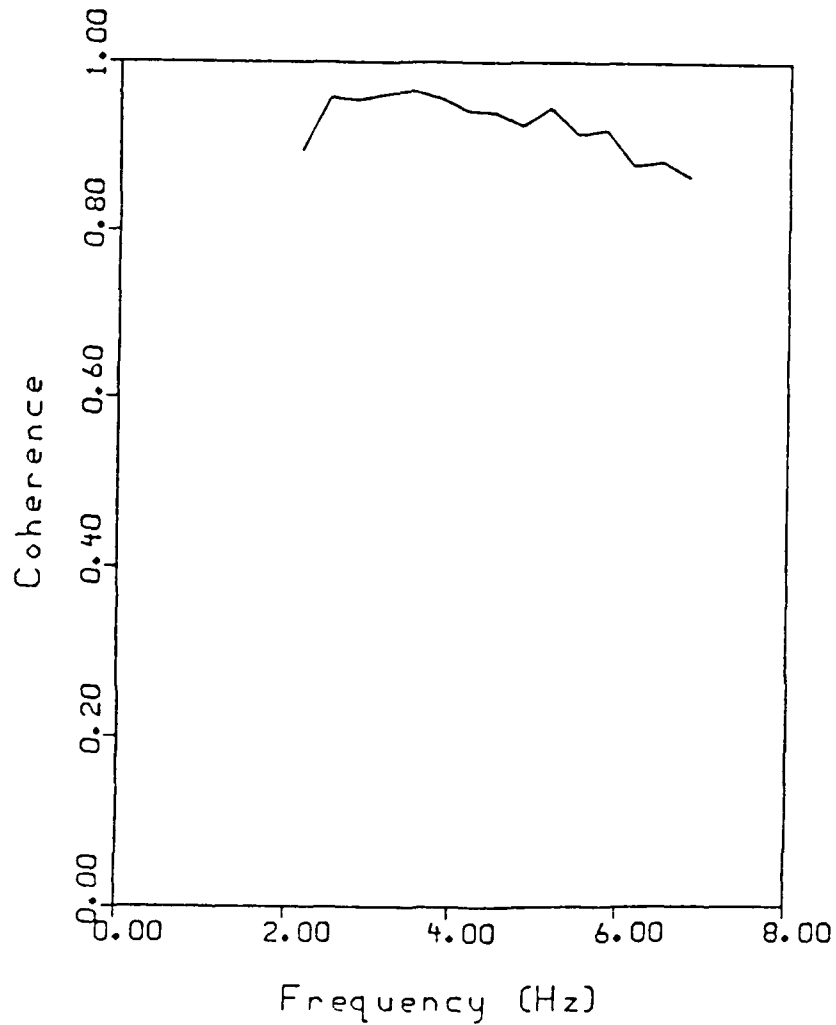


FIGURE 18: Coherences demonstrating the high factorization efficiency - 90 to 95% of the energy accounted for, across the 3C subarray of NORSAR, of the Pn phases from a group of closely located FENNOLORA profiling shots. What is noteworthy about this is the relatively large spacing, about 5 km, of the subarray sensors.

done despite the fact that all would factor well for individual arrivals. Moreover, we have found that events at the Estonian mine, designated as E9, fell into two categories with respect to the effectiveness of factorability. The Lg phases from some events, while still located at the same mine, did not reconstruct well when factored with a group of others (Figure 4). On closer examination, we have found that these had slightly different Lg envelope shapes, a feature that was very subtle and could have gone unnoticed. This may point to a different model composition for their Lg phases (and source mechanism).

Summary of the Processing Results for Regional Array Data

In this study of regional seismic waveforms, extending the concept of spectral factorability of teleseismic body wave data (Filson and Frasier, 1972), we have demonstrated that spectra of regional phases can also be decomposed into source and recording site factors, provided that the signals originated from a limited source region. Groups of events located close to each other can be identified by the fact that their waveforms can be reconstructed from their spectral source and site factors. This opens the way for relative source studies, even though the Green's functions may not be known well enough to model their waveforms deterministically.

In addition to the validation of the factorability concept, it was also found that events within such factorable groups could be further subdivided, according to relative inter-event coherence among them. The events which show high coherence probably are both close to each other and have very similar source mechanisms, although their source time functions may be different enough to make their waveforms dissimilar. The opposite must be true for events that do not show high coherence. Cross-event equalization-filtering between coherent events, using short time domain filters resulted in increases in waveform similarity, and no such increase seemed possible between event pairs with low inter-event coherence.

Site-transfer functions between sensors located at the extreme ends of NORESS appear to be complex, describable only with transfer functions with impulse responses longer than a second. Assuming the same degree of crustal heterogeneity for a source region, this may imply changes in waveforms similar in nature over small displacements of source location. Further work needs to be done in exploring the nature of such transfer functions. The work presented demonstrates that there is a considerable amount of relative source and path information that may be extracted from regional data, applying fairly standard, simple coherent time-series processing methods without requiring the knowledge or sophisticated modeling of propagation characteristics.

2.0 FURTHER ANALYSES OF DECONVOLUTION RESULTS

General Discussion

Waveforms of teleseismic P waves carry a considerable amount of information about the source and path, but such information is often hidden by extraneous effects, such as background noise, near receiver-scattering (Gupta, 1989) and waveform distortion, and near source-scattering of surface waves into P waves (Lay, 1985). Since waveforms are complex, it is not possible to see, by mere visual inspection of waveforms, any consistent, repeating frequency domain patterns diagnostic of sources and common sites. Such patterns exist, nevertheless, and this is evidenced by the factorability of spectra of closely spaced events observed at common sets of sensors. We are interested in the waveforms of P waves from explosions in particular, although waveforms from earthquakes are also important for effective discrimination.

In yield estimation, we are interested in the particulars of teleseismic P waveforms and their effects on the magnitude estimates. We would like to know whether surface reflections are present and what effects they have on the P wave amplitudes. The mere notion of a P and pP "pulse" with a small, a few tenths of a second, time delay between them carries the implication that the signal has some effective bandwidth B_e (see a definition of this concept in the introduction of this report), since no pulses can be constructed from narrowband data, and no time delays of that order can be resolved with severely band limited data. On the other hand, seismic signals often have strongly peaked spectra and small B_e predetermined by the instrument and Q along the paths. Therefore, some data processing is required to recover information over the maximum available bandwidth with acceptable S/N ratio as outlined by Equation (1). The most common way to accomplish this in geophysics is to apply some kind of signal deconvolution (Bakun and Johnson, 1973; Douglas, 1981; Der et al, 1987).

Various deterministic models of P waveforms from nuclear explosions have been proposed and used in attempts to resolve multiple arrivals. Curiously, few attempts were made to verify the consistency of these models with the data, although such verification is quite possible using all the information available in the data. There are three basic models of the P waves from explosions that we can test:

- a) The most restrictive (P+pP) model assumes that the P waves consist of convolutions of a sequence, consisting of a positive P and a delayed negative pP pulse (of identical shapes), convolved with some time domain impulse response functions of the individual sites, attenuation operator and instrument response. Other secondary arrivals are assumed to be negligible at least in the first five seconds of the P wave.
- b) This model is a more general one and it assumes that the site function concept is still valid, but the source function is of a more general shape, i.e., it may contain non-linear distortions of the P and pP pulses and additional arrivals such as spall. The spectra $F_{ij}(\omega)$ of a suite of N events (indexed by i) recorded at a set of M sites (indexed by j), can be factored in the standard manner.

$$F_{ij}(\omega) = S_i(\omega) R_j(\omega)$$

where the S_i and R_j are the source and recording site spectral factors, respectively. Generally, it is advantageous if the data set has a high redundancy $MN-M-N$ and thus, the number of total data far exceeds the sum of factors to be estimated.

Site effects have been found to be quite variable at some arrays (NORSAR, LASA), thus making the extraction of meaningful source information from waveforms recorded at individual sensors difficult. At other array locations (such as the UK arrays), site effects were found to be less important, apparently due to the care in the selection, using pre-siting surveys, of these array sites. It is reasonable to assume that the effects of the site impulse response function may be reduced by averaging the data from numerous

sites, especially for larger teleseismic arrays. This is the assumption made in the multi-channel deconvolution method developed by Der et al (1987) and the phaseless seismogram methodology of the UK group (Douglas, 1981; Stewart and Douglas, 1983). It has been shown, on the other hand, that crustal P wave responses may contain various converted phases that may not average out (Owens et al, 1987). Nevertheless, such phases are commonly late and have small amplitudes on the vertical components and thus, should not unduly interfere with the assessments of early arriving large arrivals such as pP.

- c) The third model is the most general one and does not even presuppose the existence of factorability. This situation may occur if we analyze data for a suite of explosions recorded at a network of stations surrounding a test site when the waveforms radiated in the various directions are quite different for at least some of the events in a group being factorized. In this case, the spectral factorization of a suite of events as defined above will not work unless all the events have similar radiation symmetries.

There are some statistically easily testable consequences to each model. If we adopt Model a) by inter-correlating waveforms of pairs of events using some best estimates of P and pP parameters (this should make the waveforms of a pair of events nearly identical at the same stations), the validity of this signal model could be easily tested quantitatively. Assuming that each seismic trace consists of a convolution of a site impulse response function, a source pulse $s(t)$ and a double pulse sequence due to a direct P and a pP, $P(t)$, then two seismograms recorded at the same site with the site function $r(t)$ for two different nuclear explosions can be written as

$$t_1(t) = s_1(t) * P_1(t) * r(t) \quad (10)$$

$$t_2(t) = s_2(t) * P_2(t) * r(t)$$

Where * denotes convolution. If we convolve each of these seismograms with the source pulse and the P+pP pulse of the other event in the chosen pair of explosions, then after this "inter-correlation," the two events should produce *identical waveforms* at the same sites (Mellman and Kaufman, 1981; Lay, 1985). Thus,

$$t_1(t) * s_2(t) * P_2(t) = t_2(t) * s_1(t) * P_1(t) = s_1(t) * s_2(t) * P_1(t) * P_2(t) * r(t) \quad (11)$$

The similarity of the two suites of traces then could be tested quantitatively by computing a coherence measure such as that given in Equation (4) in the beginning of this report.

These coherences should be close to unity for high S/N events if Model a) is valid and the pP parameters, delays and relative amplitudes were correct. If we find that we cannot account for most of the power in the P waves over *a sufficiently broad frequency band* by this model using *any* plausible P and pP parameter combinations, i.e., the coherences turn out to be considerably and significantly below unity, then we must reject Model a). Model b) requires only that the spectra factor into general source and site factors and that the reconstructions of the waveforms from these factors must be coherent with the original data. For testing this model over a large matrix of seismograms, we use the form given in Equation (4) in the introduction of this report and we have to accumulate the smoothed cross-products of Fourier transforms *over all data vs. reconstruction pairs* for all the jointly-factored events in the same manner (Figure 19a). In measuring this coherence, we must also adjust the degrees of freedom so that we take into account the fact that we have already estimated the site and source factors from the same data. It is also possible to test the data-reconstruction similarity only over a single event for all sites or a single site for all available events by performing the additions only over sites or events, respectively, as it was done in Section 1.0 for regional events. Failure to get high values of *C* in this test would eliminate Model b) also for the given set of events. As opposed to simple trace comparisons, the coherence

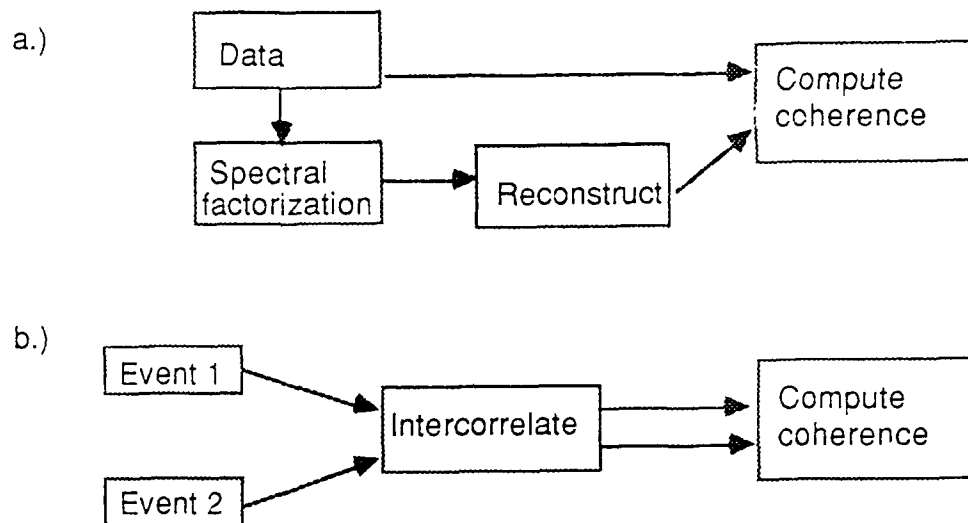


FIGURE 19: Methods for testing the efficiency (portion of energy accounted for). a) By spectral factorization. b) By the P+pP model.

measurement described above is not as sensitive to minor differences in the assumed source models such as those most widely used (von Seggern-Blandford, 1972; Mueller-Murphy, 1971; and Lay, 1985). Thus, any results would not be affected if one did not use the same source pulse models as the authors of the original papers being evaluated below and this approach allows us more flexibility.

In case Model a) is found to be not valid, we can no longer assume that the spectral (or cepstral) methods will yield reliable or meaningful estimates of "pP" parameters, since multiple arrivals consisting of P, pP, spall and other arrivals will affect the spectral and cepstral analyses in very complex and generally intractable ways, even though pP phases may be consistently present at all stations. Moreover, shapes of absolute values of spectra discarded all the phase information in the signals already and are not uniquely invertible. For instance, the spectra are unchanged by reversing the polarity or time sequence of the time-series or filtering them with dispersive filters with flat amplitude response that shift the phase only. In the case the P wave spectra do not factor over all the sensors, (case c), it is hard to talk about any meaningful "pP" consistent over the network of stations. If Model b) is valid, then we can still estimate the source time function. In the case of c) not much can be done except that we may still use small arrays to stack deconvolutions at the individual sensors over which factorability holds to look at the source from various directions.

It must be pointed out that, although our understanding of the physical processes that follow nuclear explosions is poor, it is not very likely that the P+pP model could adequately characterize P waves from nuclear explosions. Non-linear processes, such as spalling, strain release, block motion and screening of P waves by zones of damaged rock (McLaughlin et al, 1988; Barker et al, 1990; Douglas and Hudson, 1990) are likely to result in complex waveforms resulting from multiple secondary arrivals besides the pulse that can be interpreted as pP (Douglas, 1981). Despite this, it is still likely that the sizes of first P pulses, if they can be isolated, will be

relatively uncontaminated and can be used for measuring yields (Douglas et al 1987; Stewart and Douglas, 1983). Alternatively, corrections to the conventional m_b , based on the deconvolution results, could be conceivably derived.

Arguments in Favor of Deconvolution Results

Despite the sometimes counter-intuitive and complex nature of the waveforms derived from multi-channel deconvolution, physical arguments can be made for the claim that these represent real features of the source-related radiation. These arguments can be summarized as follows:

- a) Explosions in hard rock with flat overlying topography generally have a good "pP" feature.
- b) The cratering explosion at Kazakh did not have a good pP.
- c) Explosions in areas with complex topography (Degelen and Algeria) have poor and/or azimuthally strongly varying pP phases.
- d) Combined t^* and pP effects estimated from spectral Q studies and deconvolutions result in magnitude-yield relationships that seem to agree with those observed for explosions with known yield (see detailed discussion later in this report).
- e) Small, middle-sized earthquakes deconvolved in the same manner (or equivalently broadband seismograms) often show clear, simple pP and sP pulses one would expect for point sources. This shows that the deconvolution method does not give spurious waveforms for simple sources.
- f) The spectral factorization model accounts for 90 to 95% of the signal energy over broad frequency bands (1-6 Hz where the S/N allows it) in the multi-sensor seismogram assemble why source estimation procedures based other models account for much less.

Figure 20 illustrates some typical deconvolution results from a few major test sites referred to above and Figure 21 illustrates the validity of item f), above.

Tests of Some pP Results from the Literature

Estimates for pP parameters for a set of Pahute Mesa explosions were computed by Lay (1985) and Murphy (1989). The methods applied were different: Lay used a version of the inter-correlation method developed by Mellman and Kaufman (1980) which maximizes the time domain correlation coefficient between suites of inter-correlated traces, while Murphy used the shapes of network-averaged spectra to estimate the pP parameters. In Murphy's work the spectral estimates are computed in a theoretically quite intractable, unconventional fashion by using sets of bandpass filters and picking the maximum amplitude within the first five seconds of the filtered signal. Appendix C describes an implementation of the MCD method in the X winds environment. We see no advantages for such unproven procedures in view of the many existing spectral estimation methods with well-understood characteristics (Marple, 1987). Moreover, the physical meaning of such a spectral measure is not clear and is further obscured by elaborate and non-physical correction and station averaging schemes applied, allegedly, to compensate for path t^* , station effects and pP. Instead of attempting to analyze these physically and statistically intractable procedures we shall concentrate on checking some of their consequences with regard to pP parameters.

In order to test the validity of Murphy's results for pP parameters for Pahute Mesa events (Murphy, 1989) from network-averaged spectra (NAS), we have used the inter-correlation method of Lay (1985), implemented as shown in Figure 19. Since the two source pulse models are not very different, our conclusions are not affected much by the fact that we used the von Seggern-Blandford pulse.

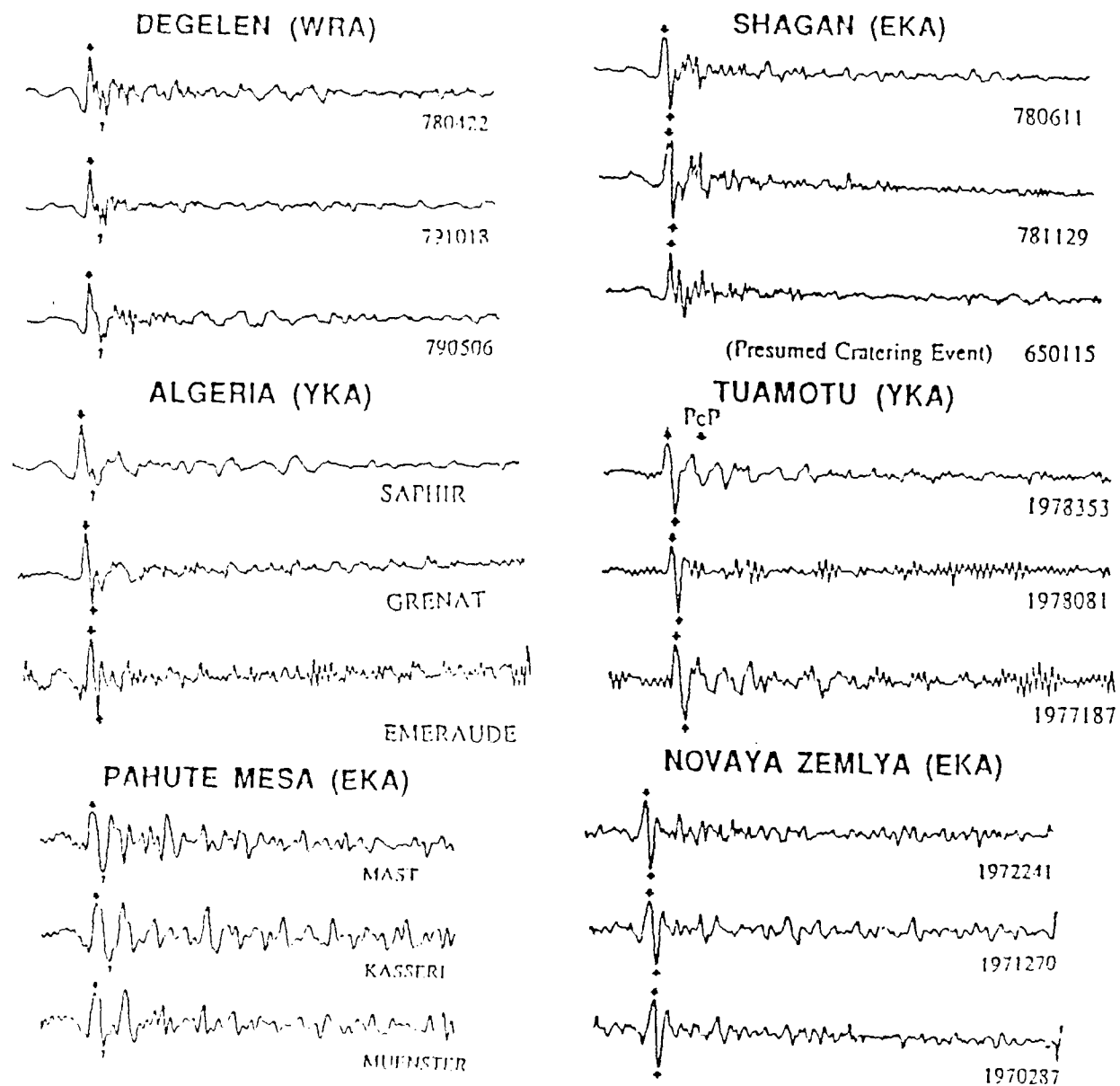


FIGURE 20: Some typical deconvolution results for various test sites.

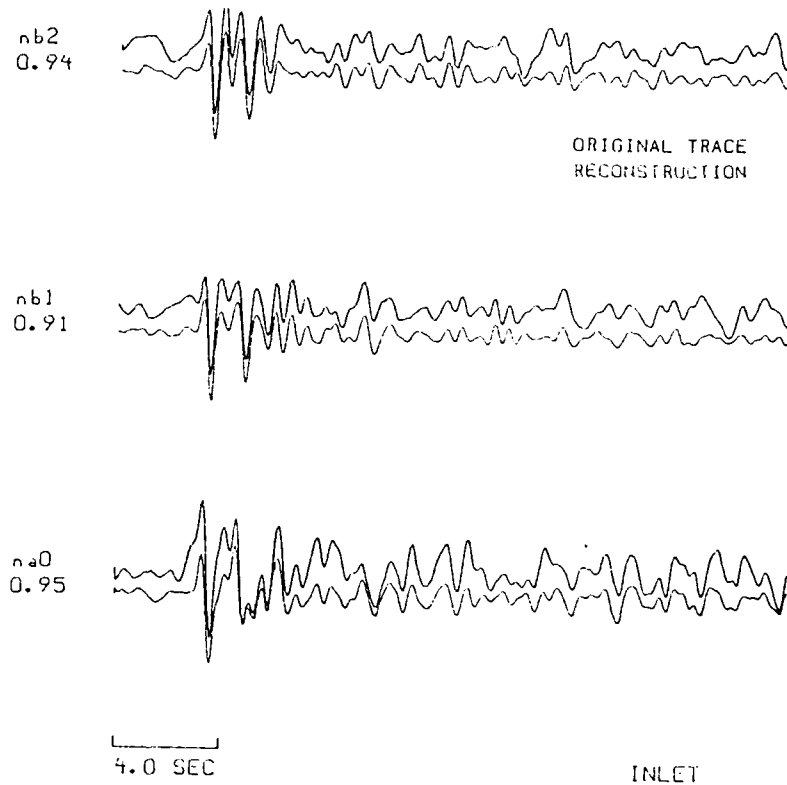


FIGURE 21: Data and reconstructions using the spectral factorization method.

We have attempted to verify Murphy's pP parameters by inter-correlating multi-sensor NORSAR data for the same Pahute Mesa explosions. Using NORSAR data had the advantages that the same events were digitally recorded over the array and that the instrumental response at NORSAR results in waveforms truly broadband in nature, as opposed to the narrowband instruments of the WWSSN network, utilized by Murphy (1989) and Lay (1985) where the bandwidth was further reduced by hand-digitization. Inter-correlation reintroduces the phase information in the signals that was discarded by the computation of network-averaged spectra and provides a conclusive test for the implicitly assumed P+pP model. We approximately compensated the source waveforms for source-scaling by using a cube-root scaled von Seggern-Blandford model, deconvolving the source waveform appropriate to one of the events and applied to it the one that was appropriate to the other. In accordance with the time windows used in both inter-correlation and NAS methodology, we computed our correlation coefficients, using a five second window encompassing only the first part of the P wavetrains at the various sensors. Figure 22 shows some of the waveform inter-correlation results for two pairs of nuclear explosions. The wavetrains that resulted from the procedure for the pairs of events as seen at the same sensors are not similar at all, not even in the first five seconds, thus, indicating that either Model a) or the pP parameters of Murphy (1989), *or both*, are not correct. Tabulating the time domain correlation coefficients (Table III) demonstrates the fact that the pP parameters derived by Murphy from network averaged spectra and/or the assumption of the simple P+pP model cannot be reconciled with the NORSAR data. Contrary to the expectation for a correct model, the correlation coefficients do not increase significantly after inter-correlation and in one case they decrease. In computing the time domain correlation coefficients, we have allowed for the possibility that the event waveforms may not have been lined up in time properly and used a five second time window for estimating the correlation coefficients in order to conform with the window used by Murphy for computing the network-averaged spectra. We have, thus tried to find the best time delay with the highest correlation coefficient by shifting *all the waveforms*, using the same delays for all traces for one event. The resulting best correlation coefficients are presented in this report. To estimate how

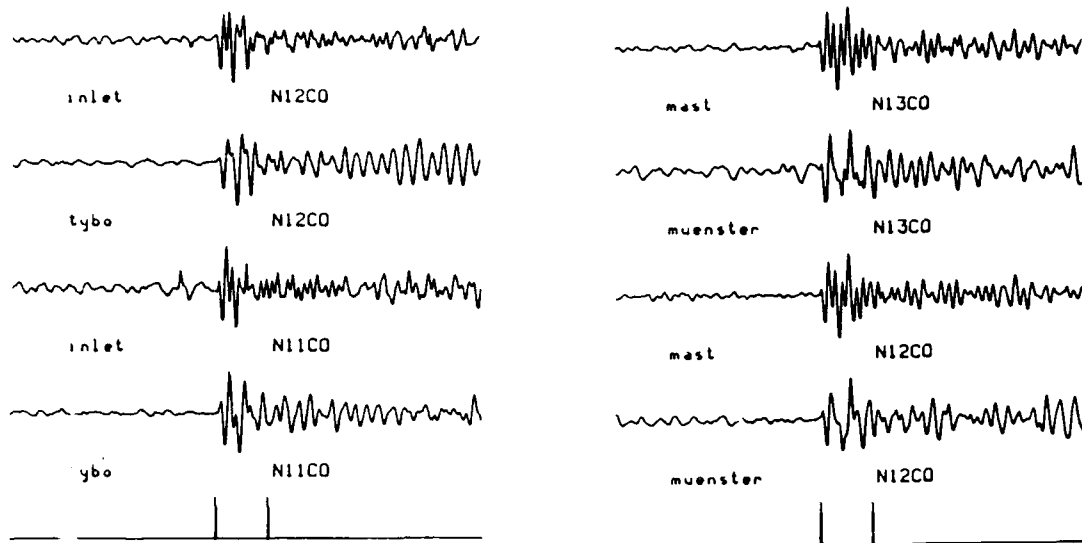


FIGURE 22: Waveform inter-correlation results at NORSAR using Murphy's (1989) pP parameters for Pahute Mesa events. The waveforms at the same sensors should be identical, but they are not indicating that the P+pP model and/or the pP parameters are invalid.

TABLE III: Intercorrelation Results with pP Parameters Derived from Spectra

Event Pair	Average Correlation Coefficient	
	Before	After
Muenster/Inlet	0.234	0.349
Almendo/Mast	0.570	0.619
Tybo/Inlet	0.577	0.552
Muenster/Mast	0.336	0.521

much power is accounted for by the pP parameters and the P+pP model, we have computed a heavily-smoothed, site-averaged coherence estimate between the inter-correlated P waveforms at NORSAR for a few pairs of events. The time window used was again five seconds in length for consistency with both the NAS and inter-correlation methodology. The result for three pairs of events are shown with the dashed lines in Figure 23, in the middle row. Compared with the factoring results, which account for more than 95% of the energy of P waves, the results from network averaged spectra account for much less. For comparison, we also show a similar analysis for data vs. reconstruction pairs after multi-channel deconvolution for a sample of Kazakh events on the right of the figure (NTS events would give similar results, since typical correlation coefficients between data and reconstructions are near 0.9) at EKA, taking into account that the degrees of freedom in this case are *decreased* by the fact that the site and source factors were estimated from the same data. We have set the degrees of freedom in both cases near 200, thus both are comparable. Any small differences between the von Seggern-Blandford and Mueller-Murphy models should also cancel in this analysis for the Muenster/Mast pair, since coherence analyses allow for the existence of simple transfer functions. The comparison shows that spectral factoring accounts for about 90% of the total signal energy even in this very wide (0.5 - 6) Hz band in the first five seconds of the P waves. We must note, however, that even if we had used the customary window of 25 *seconds* for coherence estimation, the spectral factorization would have still accounted for about the same percentage of total energy. These findings indicate that the P+pP model and/or the pP parameters derived by Murphy for Pahute Mesa are not correct. We believe that the cause of the poor performance of the inter-correlation and NAS is due to the fact that source waveforms of nuclear explosions from Pahute Mesa are more complex and cannot be explained by the simplistic P+pP model.

Lay (1985), using a WWSSN data set similar to that of Murphy (1989), also estimated a set of pP parameters for essentially the same set of Pahute Mesa explosions using the inter-correlation method. In addition to the high t^* along the paths from NTS (Der et al, 1985) and the

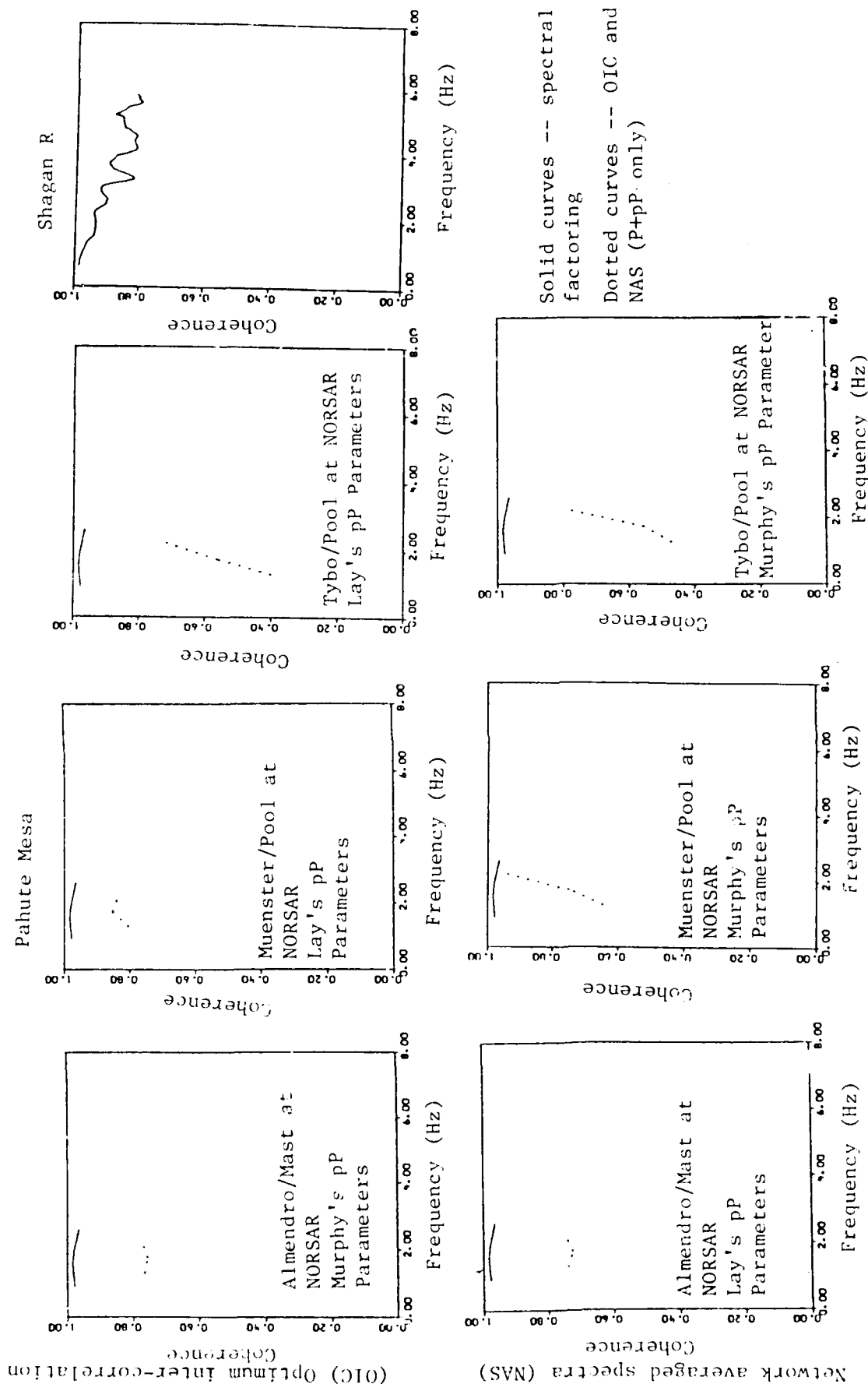


FIGURE 23: Portion of P wave energy in Pahute Mesa events accounted for at NORSAR by Lay's (top row), Murphy's pP parameters (second row) all shown by dashed lines. The energy accounted for in Pahute Mesa events by spectral factorization (multi-channel deconvolution) is shown by solid lines in the first two rows. The bottom graph shows the average value of the same for Kazakh events obtained by spectral factorization.

narrowband response of the WWSSN instruments, the effective bandwidth utilized in his analysis was further reduced by reapplying a source spectrum with narrowband characteristics (Hartzell et al, 1983). The inter-correlations resulted in some extremely narrowband wavelets which are essentially strongly-tapered sinusoidal transients. Typically, he obtained time domain correlation coefficients above 0.8, but only a few exceeded 0.9. The waveform examples in the 1985 paper are nonrepresentative since mostly those with the highest coefficients are shown. These relatively high coefficients, on the other hand, are to be expected for even random wavelets with narrow bandwidth, since sample correlation coefficients for severely band-limited data (low degrees of freedom) are strongly biased towards high values (Der et al, 1983; Bendat and Piersol, 1966).

Moreover, some waveforms have been shifted *individually* in time to achieve the "best fit" in such a manner that the first arrivals no longer coincide. We are unable to think of any justification for such a procedure, since it conflicts with the basic signal model assumed. The optimization in Lay's study was performed by fixing the parameters of one event and determining the pP of the other relative to it. Lay's results were non-unique because they depended strongly on the choices of the pP parameters for the "master" event. Thus, there are several sets of mutually incompatible results for the same events.

We have used the same NORSAR data for testing the best pP parameters (those with the highest correlation coefficients) derived by Lay. The results (top row in Figure 4) again show that the P+pP model does not account for a significant portion of the total P wave energy in the first five seconds at the NORSAR array although it does generally better than Murphy's parameters. This is not surprising since Lay's methodology takes the signal phase information into account while Murphy's does not and was designed to maximize the correlation coefficient. The coherence analyses only used the first five seconds of the signal to conform with the quite reasonable assumption, made by both Murphy and Lay, that the latter part of the signal mostly contains scattered waves and has nothing to do with the source processes. From the preceding, we must

conclude that we find no support from NORSAR data analyses for the P+pP signal model or the pP parameters derived from it.

In order to test the pP results of Murphy and Lay over a larger network addition to NORSAR data, we also acquired sets of hand-digitized WWSSN data, which contain the same seismograms as those used by Murphy (1989) and Lay (1985). Performing inter-correlations on suites of waveforms using the two sets of pP parameter estimates, we have arrived at the results shown in Table IV. The inter-correlations generally increased the correlation coefficients for both sets of pP parameters. In order to test the significance of these increases, we have computed the effective mean-square bandwidth defined in Equation (2) for our data sets. We estimated the confidence limits for the correlation coefficients using the computed values of B_e and the algorithms in Bendat and Piersol (1966). Only in one case is the increase in correlation coefficient is significant statistically, in two cases it is marginal, close to the 95% confidence limit, and in four cases it is not significant. It is interesting to note that the effective bandwidth for such data is only 0.3 Hz, and after we reimposed the source frequency spectrum the second time in the manner of the original inter-correlation paper (Lay, 1985) this bandwidth further decreased to 0.15-0.18 Hz. The small B_e are the results of the low path Q for teleseismic P waves from NTS (Der et al, 1985) and the narrow spectral response of short period WWSSN instruments. The above results should vividly illustrate the dangers of applying time domain analysis methods to severely band-limited data.

**TABLE IV: Intercorrelation Results with WWSSN Data Using
Published pP Parameters for Pahute Events**

Event Pair	Method	Corr. Coeff. before	Corr. coeff. after	Significant?
Estuary/Mast	NAS	0.378	0.458	No
	OIC	0.378	0.588	No
	OICS	0.398	0.697	Marginal
Mast/Tybo	NAS	0.639	0.660	No
	OIC	0.639	0.660	No
	OICS	0.659	0.681	No
Estuary/Tybo	NAS	0.563	0.670	Marginal
	OIC	0.563	0.730	Yes

The results discussed above prove that the P+pP model does not explain a significant portion of the signal energy and that the sometimes unexplained complexities in the source waveforms shown in the deconvolved P waves *are needed for explaining the data* and accounting for the energy in the signal in a broader frequency band. It appears that the pP parameters derived by Murphy (1989) and Lay (1985) cannot be substantiated and are probably artifacts. Any results from spectral estimation for pP parameters can also be questioned on the basis that spectra are not invertible unless we know *a priori* that the P+pP model is valid. The results of Lay (1985) fit the data better, but the large residual power unexplained by the P+pP model from both studies indicates that P waves from Pahute Mesa are quite complex and that the complex source time functions resulting from the deconvolutions are necessary to account for the broadband spectral structure of the data. The bandwidth reduction associated with Lay's (1985) procedures make them fail most tests for statistical significance. Therefore, for Pahute Mesa explosions the P+pP model fails the test. The P+pP model, on the other hand, may be reconciled with the Kazakh data better, since the deconvolved source functions of these events are simpler, although possible additional smaller "spall" phase and other arrivals may also be present in many of the deconvolutions besides the "pP". Nevertheless, since the deconvolution results must be inspected first to confirm these notions, we see no reason to use the other two methods, we have just evaluated for Kazakh data either.

Deconvolution and its Consequences with Respect to Magnitude-Yield

All the discussions about the nature of P waves is of academic interest only unless the secondary arrivals have an appreciable effect on the wave amplitudes and thus the yield estimates. The motivation for developing our multi-channel deconvolution method was to gain information about seismic sources, most notably, nuclear explosions and to improve yield estimation procedures. In the past, our ideas about the waveforms radiated from nuclear explosions were based more on theoretical preconceptions than on observational facts. Therefore, we still do not

know what the radiated waveforms from nuclear explosions would look like if we had sensors embedded in the medium outside the elastic radius. The results from our deconvolutions revealed that not all nuclear explosions seem to have a "pP" reflection. Explosions at Shagan, Sinkiang and Novaya Zemlya generally have a pronounced pP, while those at Pahute Mesa, Ahaggar and Degelen do not. All work on "pP" is only of academic interest unless the result can be used for yield estimation. The question is whether we still could assume that the first pulse in the deconvolved wavetrain still scales with yield, such that the amplitude of the total P wave is approximately determined by the superposition of the wavelets from this first pulse and a pP. If so, then the pP will have a strong effect on P wave amplitudes and hence on yield estimates. We can expect then that for test sites where the pP is generated the wave amplitude will generally be reinforced. Thus, in addition to the biases due to Q, we may have to deal with biases associated with pP.

In our previous work, we have done some simulations of magnitude-yield (using conventional m_b) relationships by using the von Seggern-Blandford (1972) source model in conjunction with a constant "effective" t^* operator, a WWSSN short period instrument response and the assumption that the first, direct pulse scales directly with yield. Due to the frequency spectra of the von Seggern-Blandford source the attenuation effect was strongly yield-dependent resulting in curved rather than straight line magnitude-log (yield) relationships. In this, we have followed similar work done previously to justify the basis for magnitude yield formulas using some physical model. In the simulations we have assumed, based on generalized deconvolution results, that only Shagan events had a pP and that the t^* differences conformed with those found from spectral studies of P waves (Der et al, 1985). The waveforms resulting from the simulations were subjected to the usual body wave calculation procedures and were plotted in Figure 24. The two sets of curves resulted by assuming that the recording station was situated in a shield area (a) or in a tectonic area (b) with higher mantle attenuation. The attenuation related source biases would be more visible with recording stations situated in shields, since through a second pass through

high Q mantle the differentials in the wave amplitudes would be preserved. In the case of stations over a low Q mantle, the differential would be decreased due to the relative removal of the high frequency components of signals. The curves in Figure A1 did not have any confirmation in the real data at the time they were produced, in fact the authors of the original report (Der et al, 1987) were themselves quite skeptical of the relevance of such results. According to these figures, the combined effect of Q and pP effects would result in very large biases that increased with decreasing yields. There would be a negative offset between the Degelen and Shagan test sites and the NTS-Shagan bias would be much higher than that anyone would have thought to be reasonable. On the other hand, no data to refute such predictions were available either, there were no compiled measurements of the kind for WSSN stations alone, these stations were (and still are not) classified into low and high Q stations, and finally, there were no yields announced for most Soviet nuclear explosions. The then available body wave magnitude data were compounded from measurements on a variety of instruments and networks, often using empirical relative scalar additive terms for equalizing the body wave magnitudes among the various types of instruments, which cannot possibly take care of all the possible *physical effects* of attenuation and pP. The simple linear empirical magnitude-yield relationships characterized with the intercept and slope parameters and with constant "bias" and offsets among test sites thus, had no physical justifications based on any physical model.

We have also repeated the same kind of calculations using the Mueller and Murphy source model and a shield station assumption (Mueller and Murphy, 1971; Murphy, 1977). This model differs from the VSB model in that the source depends on the depth explicitly and in that the source time scaling is less dependent on yield. Results of some of these calculations are shown in Figure 25. Note the large NTS-Kazakh bias and the Degelen negative offset relative to Shagan. In contrast to Figure 25, the M_S - m_b lines have little curvature and the biases increase only slightly with decreasing yield. The latter features are more in agreement with regression results on real data reported in the literature.

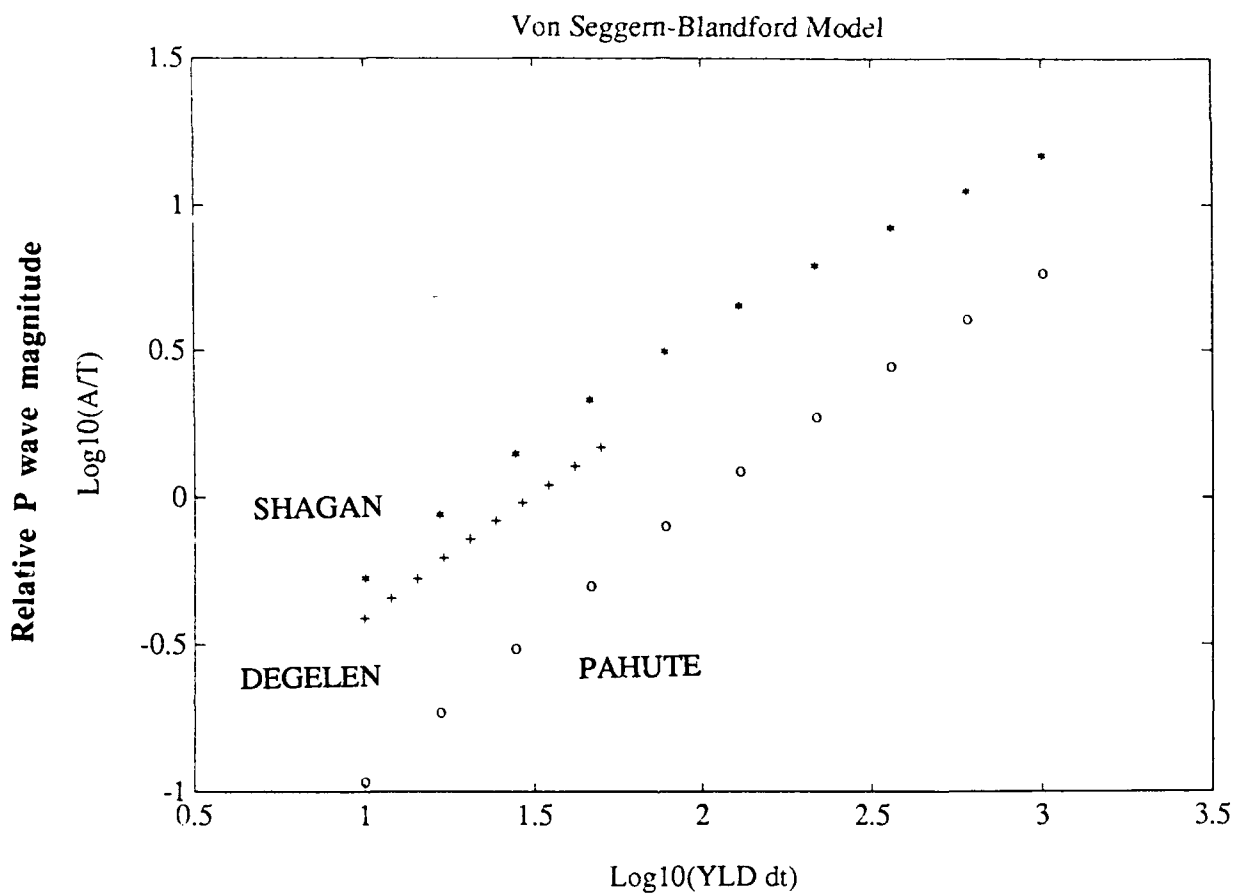


FIGURE 24: Simulated WWSSN mb for the three test sites obtained by using the source model of von Seggern and Blandford (1972), t^* derived from P spectra and pP parameters derived from deconvolution. Note the large NTS-Kazakh bias and the Degelen negative offset relative to Shagan. The Ms-mb lines have a pronounced curvature and the biases increase with decreasing yield. The two sets of curves are for stations located in shield and tectonic areas respectively. Identical source media were assumed for simplicity.

Recently, Jih (1990) analyzed a large magnitude data set for WWSSN stations and some other station recordings that were transformed to have the WWSSN response. He performed regressions on announced U.S. yields and the recently announced Soviet yields listed by Vergino (1989). In these regressions, the censoring effects on yields and the magnitudes were fully considered. The resulting magnitude-yield regression lines are shown in Figure 26. The similarities between this figure and Figures 24 and 25 can be noted. The NTS-Shagan bias is large, larger than one could explain with t^* differentials estimated from spectra (Der et al, 1985). It is also magnitude dependent and there is a Degelen-Shagan offset. These general features agree with the predictions in Figures 24 and 25. Before jumping to conclusions, we must add a note of caution. The slopes in Figures 24 and 25 are not the same as those obtained by Jih (1990) from the data, and although the offsets off the three curves are correct in sign, the differences are not the same. Some of these discrepancies may be appropriated to the fact that the assumptions and the source models were highly idealized in the simulations. For instance, actual deconvolutions of some Degelen and NTS explosions do show pP-like downswings and some Shagan explosions do not have pronounced "pP" arrivals. This could make the separation of these populations less pronounced. Besides, real data contains other arrivals as well.

Jih's results must also be further evaluated to reduce the possibility of *network bias* contamination of the conclusions. To do this, we must strive for a near-uniform distribution of stations on the focal sphere and the uniformity of the station responses. Jih used data from other systems as well and he transformed the traces to WWSSN short period instrument, prior to making readings for magnitude calculations. With these added data, Jih already obtained a fairly well-distributed network with a uniform instrument response.

We must be careful not to draw hasty conclusions from Jih's results and the similarities between our earlier simulation results and those of Jih (1990) do not necessarily prove that either of them are right, or that we fully understand the physical factors underlying magnitude-yield

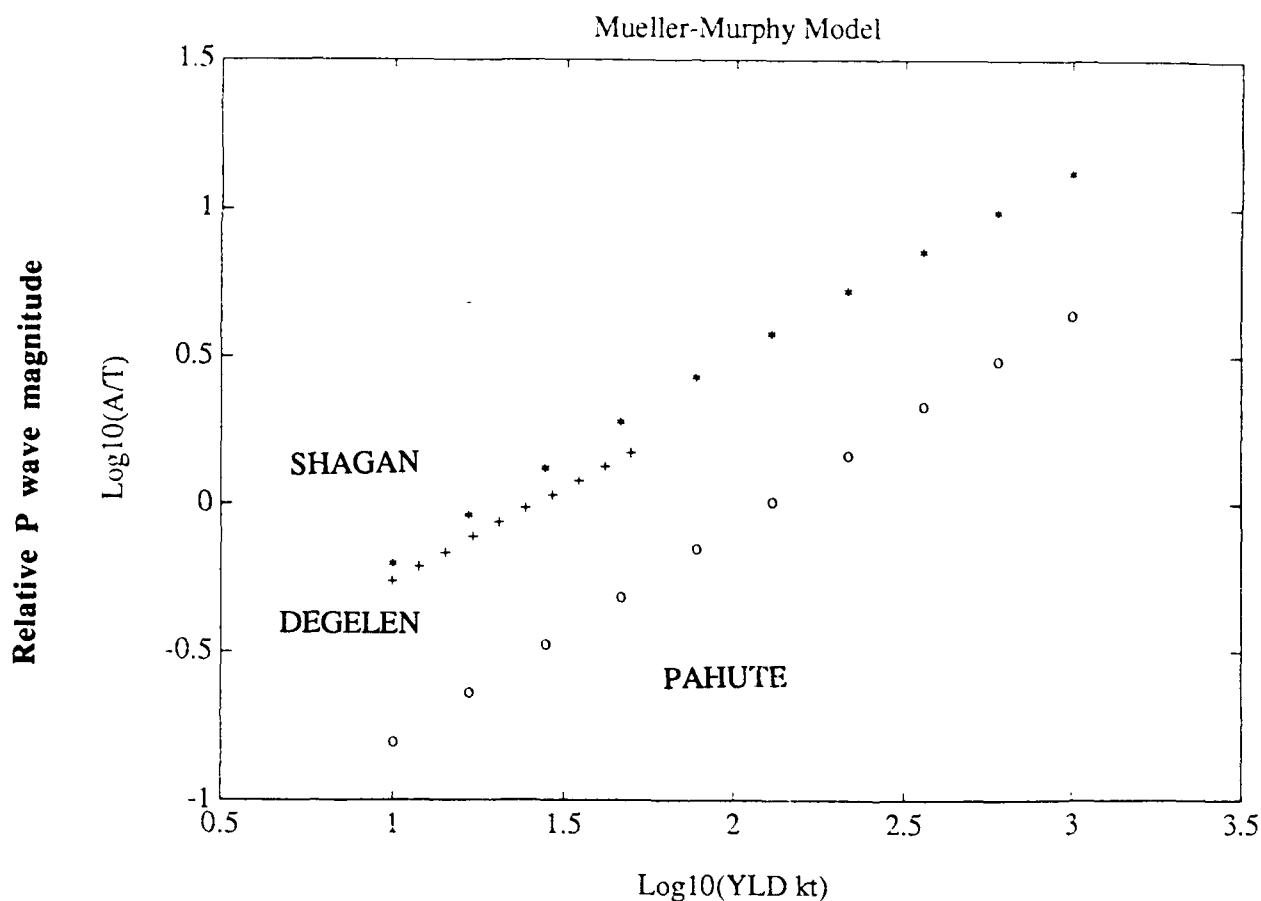


FIGURE 25: Simulated WWSSN m_b for the three test sites obtained by using the source model of Mueller and Murphy (1971), t^* derived from P spectra and pP parameters derived from deconvolution. Note the large NTS-Kazakh bias and the Degelen Negative offset relative to Shagan. The M_s - m_b lines have little curvature and the biases increase on'y slightly with decreasing yield. The latter features are more in agreement with the data. Identical source media were assumed for simplicity.

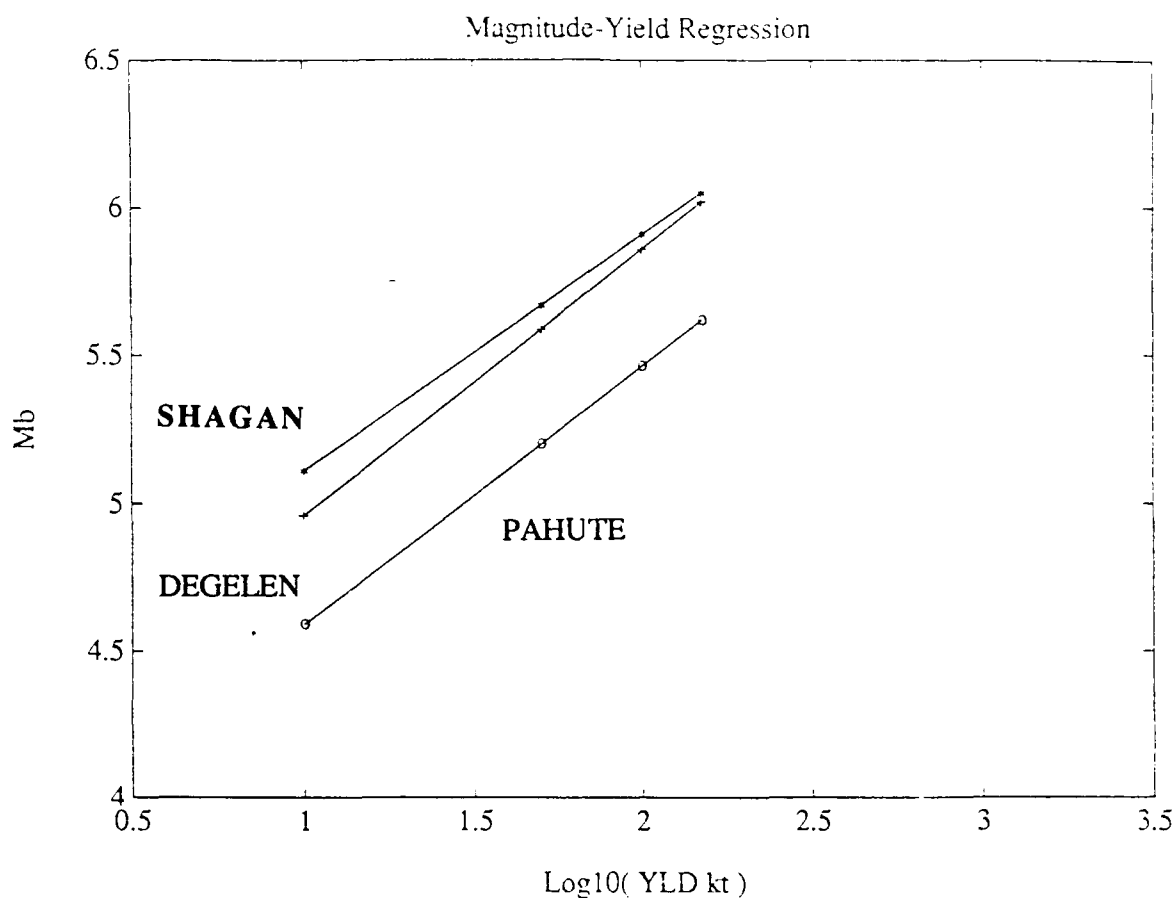


FIGURE 26: Jih's regression results for NTS and Kazakh (Degelen and Shagan) events using maximum likelihood analyses of actual and simulated P waves (recorded at other stations transformed to WWSSN response). Note the offset of Degelen relative to Shagan and the large NTS-Shagan difference that increase with decreasing m_b . Note the similarities of these lines to the general features in Figure B1 and especially to those in Figure 25.

relationships. Nevertheless, the simulation results point to the dangers of the narrow empiricism that characterized most of the studies of magnitude-yield relationships, and yield estimation procedures. Clearly, we cannot be confident of the validity of our yield estimation procedures until we close the gap between the simplistic linear magnitude-yield formulas differing only in their "intercepts" and the physical models that predict yield-dependent bias, effects of mantle Q under each station and a pP effect. *Both cannot be right* and have to be reconciled by modifying the physical models and by defining magnitude measures that depend on the physical factors in a more consistent, meaningful way. The standard body wave magnitude does not qualify (Der et al, 1981) since the interactions among wave "periods," the instrument response and divisions by period tend to obscure the physical processes, attenuation, source scaling and pP, in such a way that magnitudes will not depend on any of these factors in any clear, invertible fashion. For instance, it can be shown by simulations that in some situations strong attenuation of P phases may even *increase* the body wave magnitude (Der et al, 1981). Using other measures of body wave magnitudes such as true spectral m_b -s may be less affected by pP than implied above. On the other hand, band-pass filtered P wave maximum amplitudes used in computing the network-averaged magnitudes (Murphy, 1989) may still behave similarly to the conventional m_b , although some of the problems with period "correction" and division by the period are avoided, and thus, such measures are still vastly preferable, on physical grounds, to conventional m_b .

3.0 STUDIES OF SPATIO-TEMPORAL RESOLUTION OF SOURCE INVERSIONS

General Discussion

The time domain method for the derivation of source and path parameters from teleseismic recordings, direct modeling or least squares inversion of the observed seismic waveforms is popular and widely used. The seismological literature contains hundreds of papers of this kind. The objective of the method is to obtain optimum fits between the observed waveforms and the synthetic seismograms; the quality of fits is often judged by visual inspection or by optimizing some objective function, most commonly minimizing the RMS differences between the data and synthetic seismograms (Nabelek, 1984; Wallace et al, 1981). Some studies utilize elaborate least-squares inversion schemes with complex constraints for estimating the rupture history. Such methods (applied mostly to data sets that also include strong motion data), were described for example by Hartzell and Heaton (1983), Hartzell (1989), and Hartzell and Iida (1990). At the point of optimum time domain fit it is assumed that the parameters used in computing the synthetic seismograms are the best obtainable estimates for those of the source and path. The data utilized are diverse; they may include long period teleseismic waveforms, teleseismic short period waveforms and strong motion data. Although a narrative of the procedures leading to this best solution is commonly presented, this is usually not followed by assessments of the possible uncertainties and the limits of spatio-temporal resolution by taking into consideration the relative sizes of residual errors. The commonly missing resolution or error estimates should be part of any study. In this report, we shall discuss mostly the inversion of teleseismic long period body waveform data, but the general principles should apply to all inversion work.

Upon inspection of the results of most waveform inversion studies, it is obvious that the synthetic and real seismograms do not match perfectly and that the differences are mostly in the low amplitude, high-frequency details of the waveforms. The synthetic seismograms generally

also contain less high-frequency energy than the original data even if we allow for the presence of background noise. The inverted source time functions presented often contain details of a few seconds duration that depend, for their adequate characterization, on the same high-frequency signal components that were mismatched in the waveform inversion or modeling process. The time durations of the body waves observed at teleseismic stations often greatly exceed those claimed for the source, often there is a somewhat arbitrary cutoff in the length of time windows beyond which no attempt is being made to fit the synthetic seismograms to the data. The frequently stated justification for this is that the latter parts of the body waves are considered to be scattered waves with little relationship to the source processes. This explanation is quite plausible, but the length of such windows in practice is still determined quite arbitrarily. Some studies that use only about a dozen long period waveforms also claim to have determined source depth to an accuracy of a few kilometers and having seen indications of source finiteness. Since the wavelengths of the seismic waves at the frequencies where the waveforms seem to fit are much larger than the depth or the physical dimensions of the source and because the fits are not perfect at any frequency such claims seem to be poorly supported. Apparent internal contradictions and inconsistencies of this kind indicate a need for some quantitative justification of the results and the procedures.

Although many of the apparent problems associated with time domain waveform inversion techniques using only long period data may appear, at a first glance, to have little relevance to nuclear monitoring, the same kinds of problems need to be solved in nuclear seismology as well. The types of generic wavelength-resolution problems we shall discuss are prominent in resolving source mechanisms of compound events using surface waves and long period body waves, thus, affecting the yield estimation from M_s (Patton, 1988; Cohee and Lay, 1988). The techniques widely used for source inversion from short period data more relevant to nuclear monitoring are the same, only the frequency ranges are different. For instance, particulars of the sources such as pP, spall and strain release that could affect yield estimation could be derived better by appropriate

analyses of the spatio-temporal behavior of explosion and small earthquake sources. Admittedly, for such studies short period or broadband data will have to be emphasized more and the analysis of such data will be even more difficult because of the site effects. Our ultimate goal is to apply the methods we develop to explosions and small earthquakes on a large scale, but we need to analyze the less complex problem of inverting long period data first. Another motivation for this work is that while time domain modeling and waveform analysis as practiced today is a laborious, interactive and subjective trial-and-error process, our procedures can be automated relatively easily and may form parts of future systems for performing routine discrimination and yield estimation tasks.

It seems certain that the conclusions of many time-domain studies could stand up to rigorous analyses of errors and resolution. Nevertheless, many probably would not and the widespread use of such techniques makes it desirable to develop more quantitative procedures for assessing the reliability and stability of solutions. If the waveform fits are perfect (and the model to be fitted is known) it makes no difference whether the fitting is done in the frequency or time domain, but since it is not possible to fit any observed data perfectly, it matters how well the data matches the predictions from the models in either domain. This paper will address some aspects of this problem. Formulated in the frequency domain the inversion problem is completely frequency-separable and linear as seen by rewriting the well known equations from Aki and Richards (1980, p. 53)

$$u_n(\mathbf{x}, \omega) = M_{pq}(\omega) \cdot G_{np,q}(\omega) + N_n(\omega) \quad (12)$$

where u are displacements, M are components of moment tensors, G are derivatives of the Green's functions and N are noises. The problem in the frequency domain also becomes much simpler and less expensive to solve computationally (Olson and Anderson, 1988). In frequency domain inversion, instead of taking the time domain trace amplitudes as data we could fit the amplitudes

and phases of the various frequency components at the various recording stations. It is also much simpler to characterize site distortion, S/N ratios and attenuation in the frequency domain and optimize an inversion process accordingly. It also follows, by simply inspecting equation (12) that information on fine details found in the space-time structure of seismic sources cannot be recovered *from the data* unless the quality of the synthetic data fits is acceptable at frequencies which determine the essential features of the solution in time or spatial wavelength. Thus, fitting the data in some frequency range does not define the source spectrum at other frequencies although non-linear constraints often based on plausible assumptions or a priori knowledge about the source may influence the solution obtained at frequencies not fitted. Using the linear relationship in the equation above, it is clear that we can backpropagate, in the frequency domain, any fitting errors to assess the stability of a source inversion solution, regardless of how complex the original inversion process has been. Such backpropagation can provide the *a posteriori* error and resolution limits of the time domain source parameter estimation procedures.

With regards to the time domain inversion the following questions arise: Does the existence of "good" visual fits from time domain waveform analyses as presently practiced ensure the validity of deductions with respect to source depth, time functions and spatial details of sources as frequently presented? How well do we have to fit seismic waveforms?

In the following, we shall try to answer some questions of this kind by examining how well the waveform fitting is done in common practice as a function of frequency and introducing some statistical tests to test the stability of inversions and examine the spatial resolution. In this paper, we shall focus on the relatively simple problem of inverting the waveforms of long period body waves. The main reason for this is that array studies have shown that short period waveforms vary so much over short distances that fitting their waveforms in detail is hardly worthwhile unless we estimate waveform distortion due to near-receiver geology and make corrections for them. This is a complex procedure that may make use of signal frequency

components up to 4-5 Hz (Filson and Frasier, 1972; Der et al, 1987; Shumway and Der, 1985). Path and site related distortions of waveforms can place an upper frequency limit on the frequencies to be utilized directly, i.e., without site correction, in waveform inversion. This limit seems to be below 1 Hz, but probably it is not below 0.3 Hz, where the inter-sensor coherences seem to be high over large arrays such as NORSAR. At large arrays which were placed in tectonically stable areas (EKA, YKA) the waveform similarity is still excellent at 1 Hz. The statistical analysis of waveform variability is clearly beyond the scope of this paper and should be the subject of future research.

The prevalence of site distortion and near-source scattering is often given as the reason for de-emphasizing the high frequency parts of seismic signals, often above 0.15 Hz, in long period waveform inversion studies as we shall see below. Nevertheless, combinations of long and short period waveforms are often fitted in time domain studies. This is indicative of the fact that no general agreement exists as to the upper frequency limit above which the data cannot be used in source studies. Given the observations quoted above, this requires further justification based on the study of site-related waveform variability. The reasons for choosing a frequency range for data inversions do not affect our conclusions below; the consequences of such practices in decreasing the resolution of the source inversion results will be the same. The need for some quantification of the errors in such procedures has motivated some researchers to develop formal procedures for error estimation (Tichelaar and Ruff, 1989). These developments are important though they are still restricted to time domain inversion.

The purpose of this paper is not to present detailed criticisms of individual studies in the literature, but after describing some generic problems with the present approaches to the problem, to outline frequency domain procedures for estimating the spatial resolution of typical long period body wave inversions and show how to test the stability of solutions and estimate confidence limits for the estimates of parameters with a given quality of fit specified as a function of frequency.

TABLE V: Sources of Waveform Synthetic Pairs for Coherence Analyses

- 1) Goff, J.A., Bergman, E.A. and S.C. Solomon (1987). Earthquake source mechanisms and transform fault tectonics in the Gulf of California. *J. Geophys. Res.*, **92**, 10,485-10,510.
- 2) House, L.S. and K.H. Jacob (1983). Earthquakes, plate subduction, and stress reversals in the eastern Aleutian Arc. *J. Geophys. Res.*, **88**, 9347-9373.
- 3) Huang, P.Y., Solomon, S.C., Bergman, E.A. and J.L. Nabelek (1986). Focal depths of mid-Atlantic Ridge earthquakes from body waveform inversion. *J. Geophys. Res.*, **91**, 579-598.
- 4) Huang, P.Y. and S.C. Solomon (1987). Centroid depth and mechanism of mid-ocean ridge earthquakes in the Indian Ocean, Gulf of Aden, and Red Sea. *J. Geophys. Res.*, **92**, 1361-1382.
- 5) Molnar, P. and W-P. Chen (1983). Focal depths and fault plane solutions of earthquakes under the Tibetan Plateau. *J. Geophys. Res.*, **88**, 1180-1196.
- 6) Nabelek, J. (1985). Geometry and mechanism of the 1980 El Asnam, Algeria, earthquake from inversion of teleseismic body waves and comparison with field observations. *J. Geophys. Res.*, **90**, 12713-12728.
- 7) Pelayo, A.M. and D.A. Wiens (1989). Seismotectonics and relative plate motions in the Scotia Sea region. *J. Geophys. Res.*, **94**, 7293-7320.
- 8) Peppopane, S.K. and S.G. Wesnousky (1989). Large earthquakes and crustal deformation near Taiwan. *J. Geophys. Res.*, **94**, 7250-7264.

Disclaimer: Selection of these papers for assessing the average frequency characteristics of waveform fits does not necessarily imply criticism of the conclusions of these papers.

Quantification of Time Domain Waveform Fits

To judge the effectiveness of waveform fitting methods, we attempted to assess, in a quantitative way, the quality of waveform fits generally considered acceptable. In order to do this, we have taken 21 synthetic and data waveform pairs randomly selected from the literature (a list of these publications is given in Table V), enlarged and digitized them on a digitizing table. These samples were chosen to assess the average quality of time domain waveform fits in the literature, to be used as a point of reference. *We do not imply that any of the critical remarks above necessarily apply to the studies these waveforms were taken from.* The waveform pairs chosen are shown in

Figure 27. Above each pair the source of each waveform pair is identified by the reference number in Table V. The time domain correlation coefficient follows a slash after this identifying number. All the waveforms were rescaled to the same time scale and the positive maximum of the data waveform was normalized to unity, while the synthetic retained the same relative amplitude with respect to the data in each pair. The differences between the data and the synthetic traces are clearly visible in the original publications, and are not products of the digitizing, i.e., these differences are much larger than any plausible digitizing errors. Since all waveforms were plotted with an aspect ratio similar to the original papers, they should be easily recognizable on inspection. The reader can verify, by going back to the original studies, that we avoided the use of the worst waveform fits, and selected the better ones.

We computed the time domain correlation coefficients between data and synthetic waveforms in our sample

$$\rho = \frac{\int_0^T d(t) \cdot s(t) dt}{\sqrt{\int_0^T d^2(t) dt \int_0^T s^2(t) dt}} \quad (13)$$

This measure, compounded over all the waveforms, is also the most common choice for the judging the quality of fit in time domain waveform inversion studies if any quantitative measures of waveform similarity are applied at all (see for example Wallace et al, 1981). This parameter does not provide any information about how good the fits are between the data and the synthetic seismograms as functions of frequency; it merely provides a single number characterizing the overall RMS fit, and, therefore, is a poor measure for estimating spatial resolution. Generally, it weights the various frequency components proportionally to the cross-power spectra of the two traces, which is an accidental product of the instrument response, source spectrum and the Q

operator, but does not necessarily reflect the information content of the signals vs. frequency. Thus maximizing the time domain correlation coefficients will generally result in a suboptimum scheme for extracting information from the signals.

The time domain correlation coefficients for our data sample average near 0.9 for our selected sample; one sample is over 0.95, and only one is below 0.8. The visual similarity is also "good"; i.e., the chosen waveforms fit as well or better than the average data-synthetic pairs in the literature. The synthetic seismograms contain somewhat less high frequency energy than the data in accordance with visual observations. Moreover, the spectra are sharply peaked (Figure 28) giving the data a narrowband character.

Let us now evaluate the data vs. synthetic fits in the frequency domain utilizing an alternative similarity measure for the same data set. This measure is an ensemble-averaged coherence

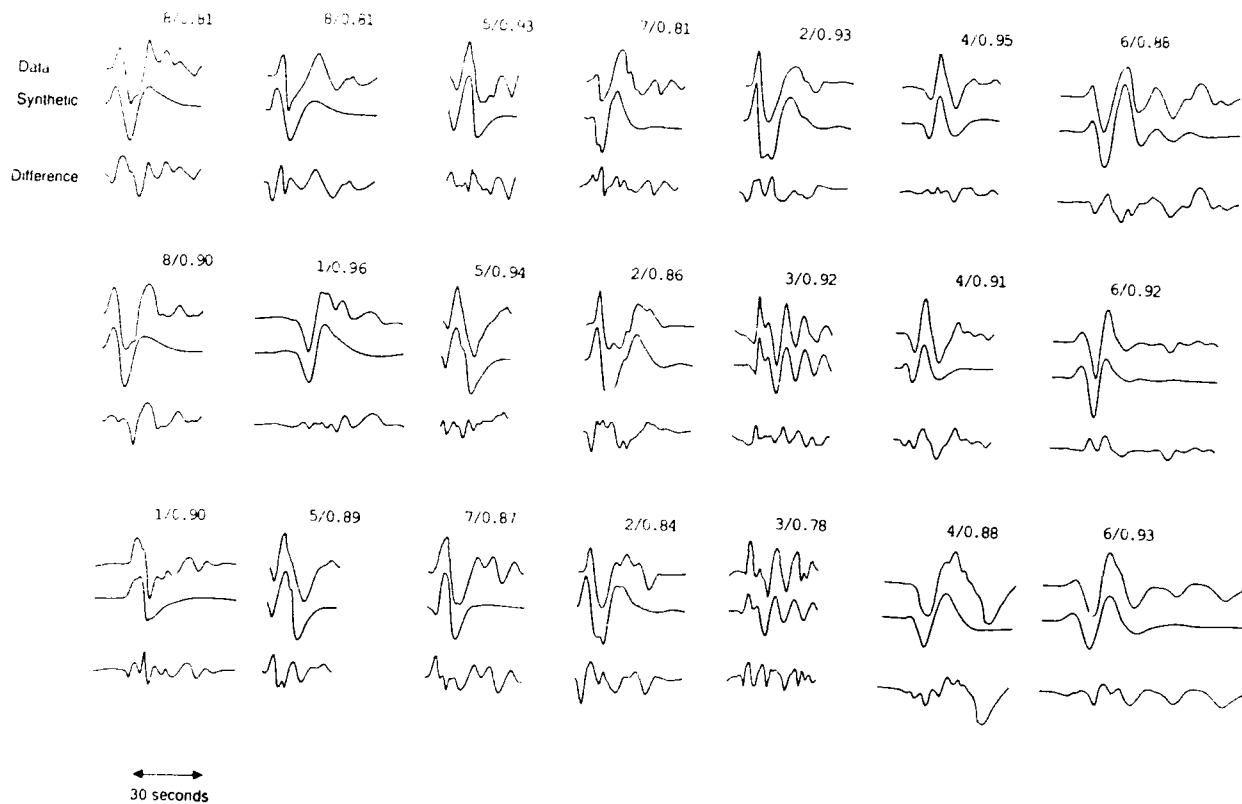


FIGURE 27: Waveforms used for computing the data-synthetic coherences in Figure 28. The different traces are shown below each pair. The two numbers next to each pair are the reference number in Table II and the time domain correlation coefficient.

$$C(\omega) = \frac{\left| \overline{\sum_i d_i(\omega) s_i^*(\omega)} \right|}{\sqrt{\sum_i \overline{d_i(\omega) d_i^*(\omega)} \sum_i \overline{s_i(\omega) s_i^*(\omega)}}} \quad (14)$$

that sums over waveform pairs i and applies spectral smoothing as denoted by the overbar. Plotting this as a function of frequency in Figure 29, it can be seen that while the fits near the peaks of the spectra are good (but by no means perfect) with a coherence a little over 0.9, this fit decreases in quality rapidly with increasing frequency. Wave components above five second periods are hardly fitted at all. For the coherence calculations the sample pairs were tapered at the trailing end by a cosine taper on the last 1/5 of the waveform, zero filled to the next common power of two in the number of samples prior to Fourier transformation. The tapering actually does increase the similarity of the waveforms and thus strengthens our conclusions below. Background noise levels were generally small compared to the amplitudes of the P waves digitized. By equalizing the amplitudes of the waveform pairs by the normalization described above, we ensured that all the sample pairs were considered roughly equally in the coherence analyses below. The approximate effective degrees of freedom for the coherence estimates shown were 50 after spectral smoothing.

Although we are confident that our digitization is good at least to 0.3 Hz, the coherence at this frequency and below it is essentially indistinguishable from zero for this data set. We shall designate this coherence plot as representing the quality of a "standard fit" in time domain modeling of long period data. Clearly, this standard will have a profound effect on the resolution of the time-space details of sources since the best fits are associated with frequencies below and near 0.1 Hz for which the apparent wavelengths are on the order of 60 km vertically and 150-250 km horizontally, much larger than the dimensions of the sources of mid-to-large earthquakes. By

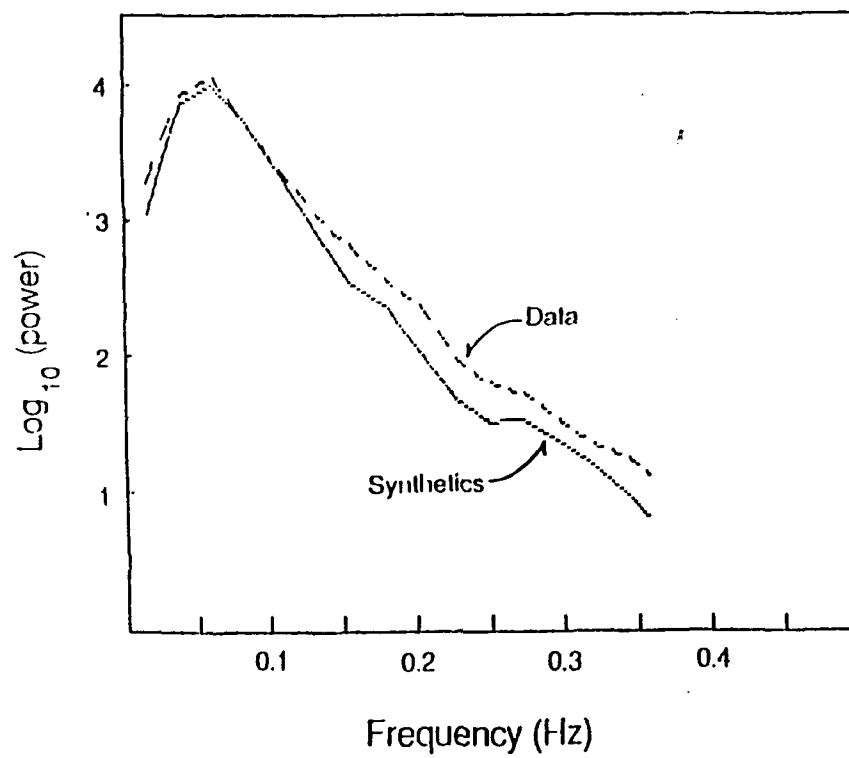


FIGURE 28: Averaged spectra of a sample of long period data and synthetic seismogram pairs randomly selected from the literature.

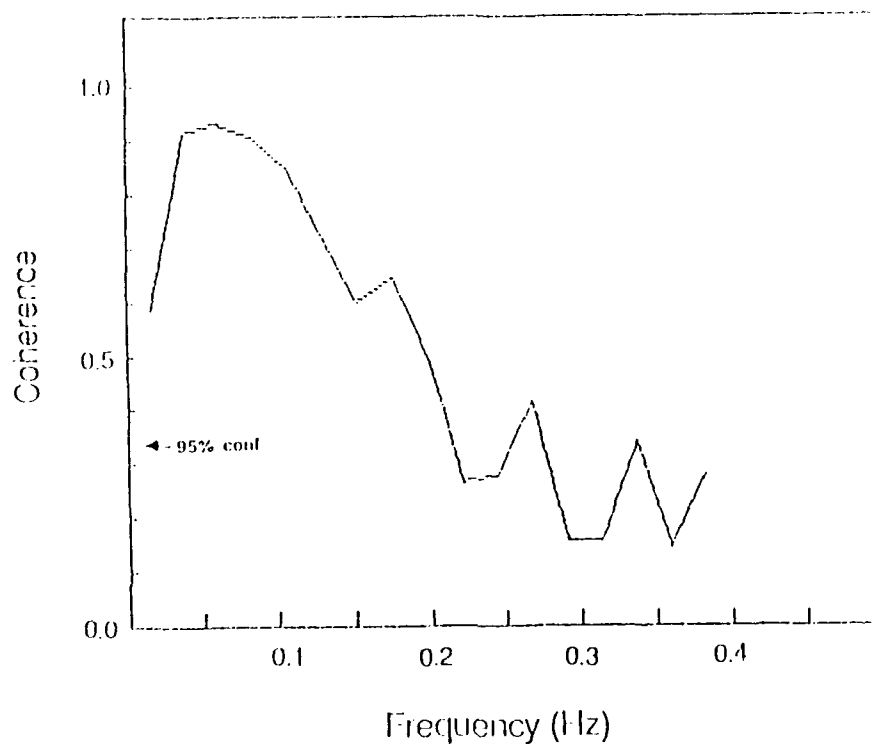


FIGURE 29: Ensemble-averaged coherences of our sample of data-synthetic pairs defining the “average fit”. The 95% limit shows the level below which the coherences are not significantly different from zero.

analyzing such waves, we are attempting to measure changes in source depths on the order of a few km and source finiteness on the order of a few tens of kilometers.

We have further verified our assessment of waveform fits by analyzing the differences of the data and synthetic traces. Plotting these, we found that the amplitudes of the difference traces suddenly increased at the arrival time of the signal and remained at the same level, about $1/3$ or $1/4$ the signal amplitude, throughout the waveform sample (Figure 1). Thus, the initial part of the waveform, contrary to a false impression that one might easily get from visual inspection of the waveform pairs, is not fitted any better than the later part. The increase in the amplitude of the difference traces at the arrival time of the signals shows that the misfit is not due to background noise. Moreover, when we compared the averaged spectra of the difference traces to those of the data and synthetic and data traces themselves the spectra of the difference traces were significantly below those of the latter two only in the .04-.14 Hz range. This confirms our assessment from coherence analyses that the average long period data body wave inversions in the literature generally fit only a small range of frequencies in a band not exceeding 0.1 Hz. Thus, the fact that the quality of the waveform fits vary strongly with frequency within the pass-band of the long period instrumentation, which is also quite evident from simple visual inspection, probably should not require further elaboration.

Statistical Analysis of the Source Inversion Problem

Let us look now at the space resolution obtainable from our typical long period waveform fit. First of all, we need some kind of statistical method to find the location of a point source with known mechanism in space (depth and location within a limited region). Usually, there exists some a priori knowledge of location and depth from short period data, the source mechanism may be known approximately from conventional analyses of first motions, but the exact depth and

details of source mechanism may be unknown. These could be determined by finding the maximum of the frequency domain statistic

$$F = (N - 1) \frac{\frac{f S f^*}{f f^*}}{\text{tr } S - \frac{f S f^*}{f f^*}} \quad (15)$$

which becomes a source "image" when mapped in space. In this formula, N is the number of sensors, S is the spectral matrix of the data, computed as d^*d , the outer product of the Fourier transforms of the data at various sensors, and f is the vector of Fourier components at the various sensors of the elementary source (synthetic seismograms) we try to map over space. Note that the customary smoothing in constructing the spectral matrix is not an essential part of this process and it can be, and will be, omitted in the examples that follow. Thus, the method can be applied to short transients, such as teleseismic body waves, just as well. The technique described above is essentially an adaptation of a high resolution F-K algorithm (Shumway, 1988) for finding the position of the elementary sources from waveforms associated with different slownesses, instead of the common application of finding the slowness vectors of signals associated with recordings at an array with known sensor coordinates. It can be shown easily that mathematically the two problems are the same, since the position and wavenumber vectors are interchangeable in the phasor factors $\exp(ikx)$. The additional complication caused by the fact that the amplitudes of the various frequency components are different is taken into account by normalizing the results of beaming by dividing with ff^* . Thus, the problem of finding the source position in a limited source region is analogous to finding the wavenumber vectors of noisy signals observed at an array of limited spatial extent. Since in our application the wavelengths of the signals are generally larger than the size of the source region and there is always some mismatch noise the problem is an extremely difficult one. Therefore, we must expect serious problems due to trade-offs, lack of

resolution and sidelobes in the process. These problems are present in the time domain approach to the problem as well, although this may not be obvious.

Similar ideas pertaining to finding the positions of signal sources in complex waveguides were advanced by Baggeroer et al (1988), Byrne et al (1990) and Steele and Byrne (1990), among many others, in underwater acoustics for locating submarines, and Goldstein and Archuleta (1987) in seismology using the Capon and MUSIC (Capon, 1969; Schmidt, 1981) algorithms respectively for studying seismic sources. The starting point for all the algorithms is the same, we have waveform data and some algorithms for computing Green's functions. The goal is to estimate the spatial distribution of sources and their time functions.

Our statistic is simply one of the many possible algorithms for examining the spatial resolution: we chose it because it is intuitively and computationally simple, does not require matrix inversion or eigenanalysis, and has a tractable probability distribution. The F statistic defined by equation (15) is essentially a ratio of the generalized beam power, the expression in the numerator, and the residual power or mismatch noise in the denominator (a S/N ratio, not to be confused with the conventional definition where the noise is commonly defined as ambient noise). This statistic for a single frequency has an approximate non-central F distribution at individual frequencies with 2 and $2(N-1)$ degrees of freedom for N input waveforms and the approximate associated non-centrality parameter is twice the estimated S/N power ratio i.e., $2F/(N-1)$ (Shumway, 1988; Hogg and Craig, 1978).

Particulars of this statistic, its relationship to Capon's (1969) estimator are given in Appendix A of this report. A simpler alternative algorithm based on a c^2 statistic, yet untested is described in Appendix B. If we stack the F statistics obtained at various frequencies over the source coordinates the probability density function of the result is approximately normal with mean Σm_i and variance with $\Sigma \sigma_i^2$ the sums are being over all the frequencies used, and m_i and σ_i are

the mean and the standard deviation estimates of the individual non-central F distributions for a single frequency. The degree of misfit will affect the mean and the standard deviation of the F statistic at each frequency, thus providing a way to obtain *a posteriori* error estimates automatically. The method above can also be considered a backpropagation algorithm in which the phase shifts due to propagation are compensated for and we are testing for the phase alignment of the various Fourier components at various source coordinates. Note that in the algorithm any common spectral factors, such as those associated with instrument responses and source spectra, divide out. Thus, it is well suited to avoid trade-offs between such factors and the source depth and location and to investigate the latter separately. The mathematical derivation for an alternative, yet untested algorithm based on central χ^2 statistic is given in Appendix B of this report.

For testing the method on a simple case, we shall assume the source crust to be a half-space so that the generalized beamsteer vector becomes

$$f_i(\omega) = \left\{ \sum_{j=1}^3 a_{ij}(\omega) \exp(-i\omega t_{ij}) \right\} \exp\left(-i\frac{\omega}{c_i} \hat{k}_i \cdot \mathbf{x}\right) \quad (16)$$

where the subscripts $j=1,2,3$ refer to the phases P , pP and sP respectively and \hat{k}_i is a unit vector appropriate to a station i , \mathbf{x} is a position vector in the source region, the c_i are phase velocities at a given station, and the t_{ij} are the travel times of the P , pP and sP phases. The source "image" is a mapping of F over the source region in depth and horizontal coordinates. Depth dependence enters into this formulation through the delay times of the depth phases and the exponential factors are determined by the horizontal coordinates of the source relative to some reference point and by the phase slownesses. We assume for the sake of convenience, that the Green's functions are perfectly known, which is generally not the case. The common problem of poorly defined Green's functions, which makes the inverse problem even less tractable, is not addressed in this paper.

Having specified a statistically tractable quantitative way to image a source, we applied this algorithm to a typical sample problem, that of decomposing a compound source with known mechanism using P wave data from 10 stations, azimuthally well distributed around this source with the source-to-station azimuths and slownesses listed in Table VI. The P waves contain only the P , pP and sP arrivals. Our compound source source in this test consisted of two double couples of equal power with identical mechanisms (strike= 245° , dip= 30° and rake = 120°) the first situated at a depth of 3 km near the center of the search grid, and the other displaced to the northeast by 28 km at the depth of 9 km in an elastic half-space with 6.5 km/sec compressional and 3.8 km/sec shear velocity. This is about the simplest compound source inversion problem there is, and it is representative of the scale of a medium-sized earthquake.

In Figure 30, we show *images* of this source (or in the parlance of underwater acoustics ambiguity surfaces), i.e., plots of F located within a coarse search grid with 5 km increments, at different depths. Normally, of course, one would not search an area of 250 X 250 km, such as the one shown, but would look for maxima of some statistic in a smaller source area or a fault plane. Nevertheless, presenting such images should give a good idea of the spatial resolution provided by the long period waves we utilize here. For the result shown in Figure 30, we have added gaussian-distributed random complex numbers to the original f vectors (for a source at 6 km depth) to correspond to a 0.9 coherence (correlation coefficient) value between the simulated "data" and the synthetics (the f 's) and used the frequencies between 0.02 and 0.15 Hz, stepped by 0.0125 Hz, with equal weight to define the frequency range utilized by the "average fit." The statistic gives a maximum that is located between the two sources and there is very little indication, if any, of the presence of two sources if we are satisfied with this quality of fit. With the low frequency end of the spectrum fitted preferentially, there is thus, a tendency for the image to merge the two sources together at the "centroid."

TABLE VI: Station Parameters for Numerical Simulations

<i>Station #</i>	<i>Azimuth /degrees</i>	<i>Slowness sec/km</i>
1	0.	0.08
2	0.	0.05
3	60.	0.06
4	120.	0.06
5	120.	0.05
6	180.	0.08
7	180.	0.05
8	240.	0.06
9	300.	0.05
10.	300.	0.08

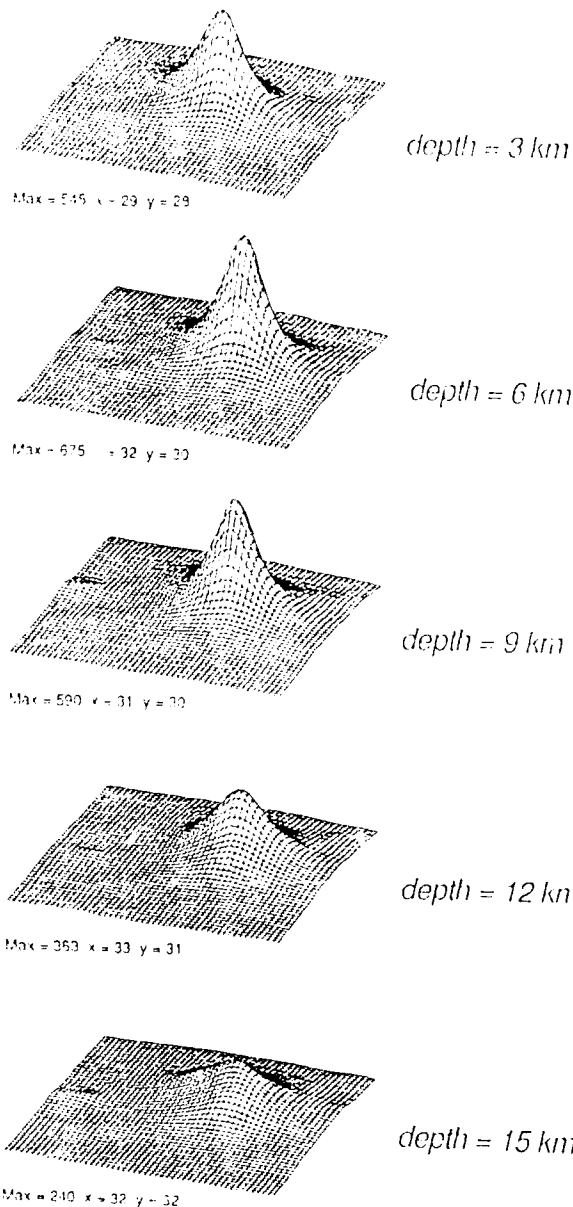


FIGURE 30: Perspective views of the variations of the frequency-compounded F statistics over the frequency range of 0.02-0.15 Hz for a pair of double-couple point sources with equal power. Uniform random noise was added to simulate a fit with an average correlation coefficient of 0.9. The peak value occurs between the two sources and the two sources were not resolved. The F statistics were computed for various assumed source depths and the sides of the source region views are 250 km long. The maximum value of the statistic and its location in gridpoint coordinates from the left lower corner (5 km spacing was used in both x and y) are given beside each view. The gridpoint x-y coordinates of the two synthetic sources were at 27, 27 and 31, 31 and the depths were at 3 and 9 km respectively.

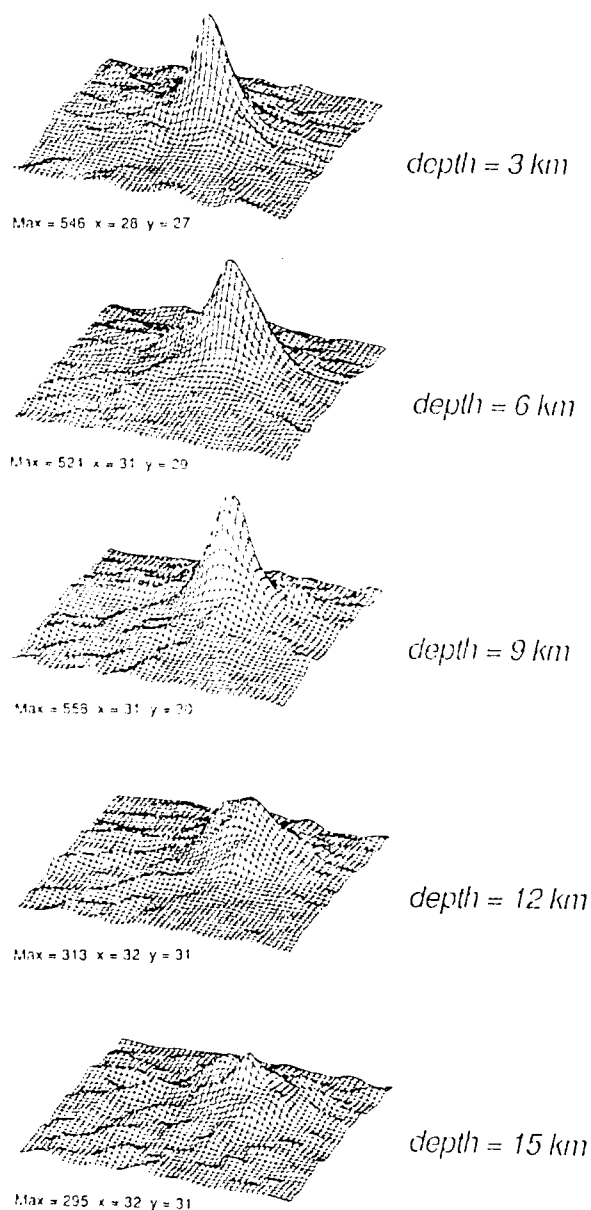


FIGURE 31: Perspective views of the variations of the frequency-compounded F statistics over the frequency range of 0.02-0.35 Hz for a pair of double-couple point sources the F values were computed for various assumed source depths. Random noise with 16% of the signal was added throughout the band. The peak values occur nearer to the two sources and the two sources were marginally resolved (for additional details of this display see the caption of Figure 4).

We next investigated how image could be improved if we extended the frequency range of fitting to 0.02-0.35 Hz. We added 16% noise throughout this band, thus doing away with the "standard fit" and attempting to fit the high frequencies as well as the low frequencies. As Figure 31 indicates, we now see two maxima at two different depths corresponding to the two sources. The locations are still closer to each other than the actual ones, and we still have a sizable peak between the two source locations at depth where we put no sources.

Finally, we decided to discard the lower range of frequencies altogether and did the fitting in the 0.15-0.35 Hz range with 16% noise added. We see in Figure 32 that the two sources well resolved with the values of the statistic between the two sources much diminished, but the tendency of the two sources to merge is still evident by the biases in the positions, the peaks being closer together than the originally specified source locations.

These results spell trouble for the studies of moderate-to-large earthquakes, based on long period data only, since it appears that fitting the data does not allow us to resolve details of fault motion. These results do not imply that one could not outline, with the prevalent quality of waveform fitting, the faulting history of larger events with source dimensions considerably larger than the location and depth uncertainties found in our simulations. Nevertheless, even in such cases not much detail in the faulting process could be derived from the data. The most that can be achieved using only the low frequency components of the data is some definition of a "centroid" location and an ill defined associated source function which may indicate by its long duration that the source had a significant spatial dimension.

One may ask whether our choice of the test statistic could be the cause of poor resolution and the application of the more conventional statistic, the time domain correlation coefficient could have yielded better resolution. In Figure 33, we show perspective plots of the expected correlation coefficient for various locations and at a few depths obtained by fitting a single double couple as a

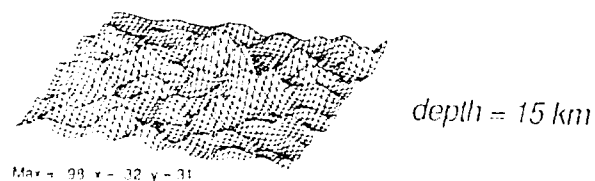
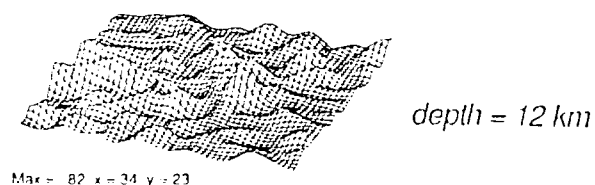
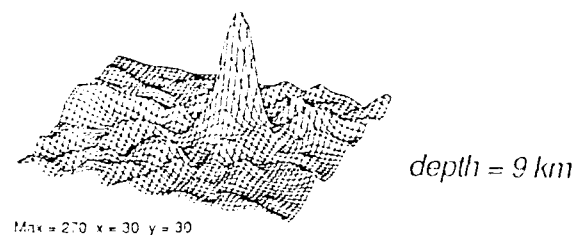
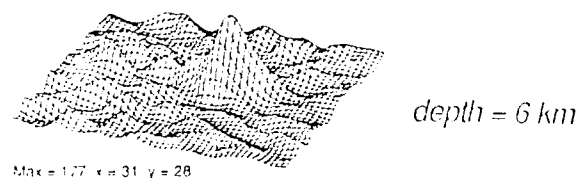
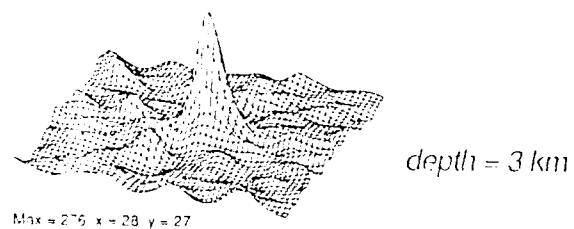


FIGURE 32: Perspective views of the variations of the frequency-compounded F statistics over the frequency range of 0.15-0.35 Hz, thus deleting the low frequencies, for a pair of double-couple point sources the F values were computed for various assumed source depths. Random noise with 16% of the signal was added throughout the band. The peak values occur near to the two sources and the two sources were well resolved (for additional details of this display see the caption of Figure 4).

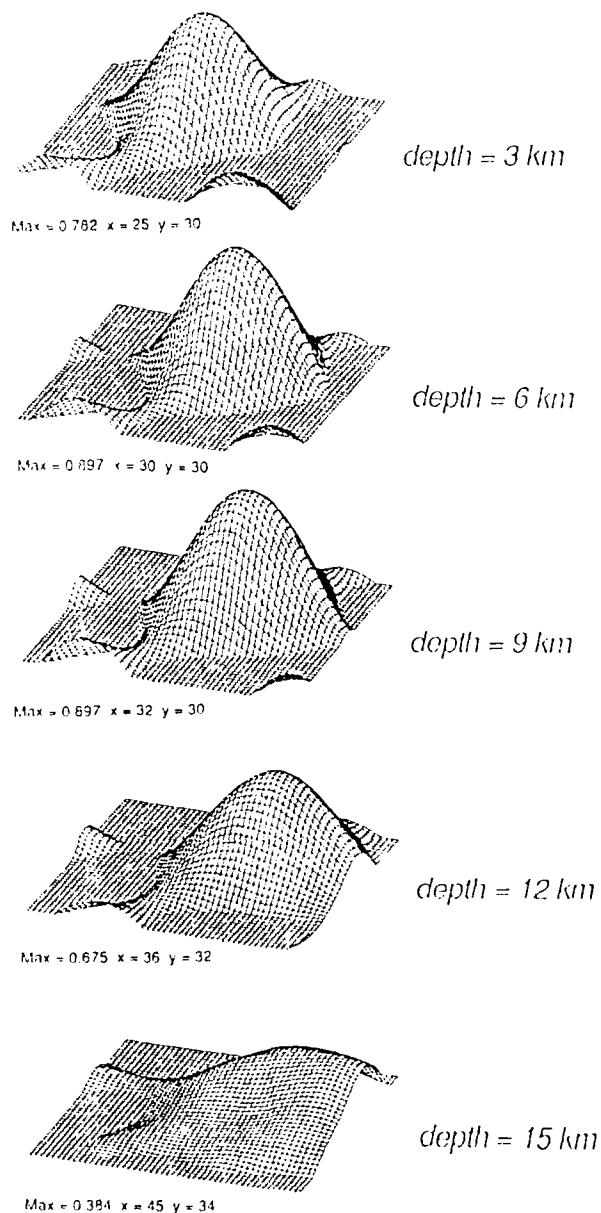


FIGURE 33: Perspective views of the variations of the positive parts of the simulated site-averaged time domain data vs. probe vector (data-synthetic) correlation coefficient over the frequency range of 0.02-0.15 Hz for a pair of double-couple point sources the F values were computed for various assumed source depths. The negative parts of the correlation coefficient were set to zero arbitrarily, since only peak positive values are of interest. Random noise was added throughout the band to give a peak value near 0.9. The two sources were not resolved (for additional details of this display see the caption of Figure 4).

source. The time domain correlation coefficient was approximated by the frequency domain equivalent formula (we have set up the whole simulation algorithm in the frequency domain) for zero lag

$$\rho = \frac{\sum_{\omega} P \operatorname{Re} (f d^*)}{\sqrt{\left(\sum_{\omega} P f f^* \right) \left(\sum_{\omega} P d d^* \right)}} \quad (17)$$

where $P(\omega)$ is the power spectrum of the data (those of the synthetics are very similar) shown in Figure 2, the sums are over frequency, the d are the Fourier transforms of the synthetic data vector (sums of direct P and surface reflections for all the sources), and the f are the probe vectors (in our case, the Fourier transforms of the expression in equation 5 for each sensor). In order to resolve the multiplicity of this source, one would expect that the correlation coefficient should be small enough to alert us that this is not a simple source, moreover, we would hope that the correlation coefficient would show two distinct peaks, each at the proper source position. None of these expectations are met, however. The maximum values of the correlation coefficient are closer to the deeper source, for this realization there are two identical maxima of 0.897 at 6 and 9 km depth and the value at 3 km depth is smaller, the locations do not correspond well to the actual positions of the sources. Accepting the standard of 0.9 correlation coefficient one would end the search and announce an acceptable fit for a simple double couple source at these depths and either of these locations. The correlation coefficient gives no clue about the presence of the shallower source, there is no double maximum. Note the large sidelobes of the correlation coefficient which are due to the limited range of frequencies applied and their long wavelengths. Incidentally, both the F statistic and the correlation coefficient are expected to behave similarly when the frequencies used are limited to a narrow range. The generalized beam on which the F statistic depends is maximized at the same spatial points where the correlation coefficient is maximized, and as we have shown

above none of them resolve the two sources from the information below 0.15 Hz. On the other hand, when the frequency range is wider the F statistic can keep track of the spatial resolution by estimating and compounding the same for all frequency components, while the correlation coefficient does not convey the same information since the same correlation coefficient can be obtained by mismatching different combinations of frequency components.

Our results for the simple problem of resolving two not very closely spaced sources of equal strength in a half-space imply that the prevalent fitting standards and frequency components utilized are just on the verge of indeterminacy for resolving spatial details of seismic sources of moderate-to-large events from typical long period body wave waveform inversions. The indeterminacy often manifests itself in the fact that in many studies, if the fits are deemed unsatisfactory, adding a few additional parameters or complications to the source model will generally produce good waveform fits. If such problems were overdetermined, i.e., there was enough redundancy in the data set, then it would be more difficult to find solutions and the inability to find a solution might sometimes point to the inadequacy of the models.

The preference for fitting the low frequency end of the spectrum is based on the perception that low frequency components of the signal appear to be more stable. One could argue, however, that since in studies of source spatial characteristics we essentially try to measure small time delays among subevents and various other arrivals (such as pP and sP) the phases of low frequency components (and the associated waveforms) will be less sensitive to variations in these times than high frequency components. Thus, at least some of this stability may be illusory.

Depth Estimation Error Limits for the El Golfo Earthquake

Our choice fell on this event since the El Golfo earthquake was reported to be a simple point source, a strike slip event found to be at 10 km depth by Ebel et al (1978) and thus, similar to

the synthetic case analyzed above. The source time function was estimated by Ebel et al, to be a simple triangle of 4 sec duration and the t^* along the paths to the receiving stations recording on WWSSN 15-100 LP instruments was assumed to be 1.3 sec. We adopted these parameters as well as the fault orientation and the crustal model given in the same paper and used formula (4) in an attempt to verify the depth estimate from the P wave data by our imaging method.

The Green's functions (f vectors) were calculated by using an adaptation of the formulation of body wave radiation from a point source given by Douglas et al (1971) generalized to a flat-layered source crust model. The synthetic seismograms generated are very close to the ones given in the paper by Ebel et al (1978). We attribute some small, occasional differences to the fact that while our program, based on propagator matrices, automatically includes all rays in the source crust, the program used by Ebel et al needs the specification of all rays desired (Langston, 1976). Thus, some less important rays may have been omitted in the calculations of Ebel et al. In any case, the synthetic waveforms we have generated are matching the data just as well as those of Ebel et al (1978) and are very similar to those used in that study.

The long period P waveforms to be processed were obtained by digitizing the enlarged seismograms from the paper on a high resolution digitizing tablet. We have matched a 37 sec long segment of the waveforms, similar to the original study of Ebel et al (1978), and tapered the trailing edge with a smooth cosine taper. This essentially utilized the first 1-1/2 cycle of the signals, similar to the range of the visual fitting in the original paper. Compared to the sizes of the mismatches between synthetic and data the digitizing errors and any trace distortions are very small and should not affect the our conclusions. In order to eliminate the absolute times as a factor in the matching procedure (had we known the absolute times, properly corrected for mantle heterogeneity, we could have obtained the depth from those alone), we lined up both the time domain representations of the f 's and the data on the first P arrival.

We have made two test runs while varying the source depth and fitting the spectral structures in the .02 to .15 Hz band using all frequencies with equal weight. In the first test, we matched the synthetic seismograms for 10 km depth with source crustal responses appropriate to all depths and added 5% random white noise (to avoid a singularity at 10 km depth) and in the second we matched the data with the source crustal responses appropriate for different source depths; for the results of the latter we also computed our admittedly crude error bounds analytically, and assumed that the compound F statistics have an approximate normal distribution. The means and variances of this normal distribution were computed by summing for all the various frequency components the means and variances of the individual non-central F distributions, appropriate to the quality of fit (S/N ratios) implied by the estimated values of F statistics (Hogg and Craig 1978, p. 288). The means and variances of these individual non-central F distributions were computed by utilizing the approximate formulas given by Mudholkar, Chaubey and Lin (1976). Thus, for estimating the error bounds the quality of fit is automatically taken into account by our algorithm.

As one would expect, the computation on the synthetic seismogram for 10 km depth resulted in an unambiguous maximum of the statistic at 10 km depth with narrow 95% error bounds relative to the F value at the peak (Figure 34a). The data, on the other hand, when subjected to the same analysis procedure could be reconciled with practically any depth shallower than 16 km (Figure 34b) and had much smaller F values. There are two peaks at 5 and 14 km depth, but they are not very significant. Some of the depths in the acceptable range are considerably outside of the 2 km accuracy limits claimed by Ebel et al (1978) for their solution which, at 10 km, is not inconsistent with our depth limits. Theoretically, if the synthetic seismograms and the data are similar enough they should give the same solution. It is shown above that the data and the synthetic seismograms for the same event, although their waveforms are similar, give *substantially different* conclusions with regards to source depth which could have caused problems if we had tried to analyze the fault motion in any detail on the fault plane. We have essentially shown in Figure 34a that for a similar problem the method should have given the

same answer had the waveforms been more similar. Despite the fact that the original El Golfo earthquake study also utilized some additional data, a limited amount of SH and surface waves, we do not believe that the inclusion of these would have changed our results or conclusions. We agree with Ebel et al (1978) that the best visual fits for P waves appear to be near 10 km in source depth. We have found, however, that this may be deceptive. In Figure 35, we show the data waveforms and synthetic seismograms appropriate to various source depths for the stations CAR, WES, TRN, UME and COL. It seems that the best waveform fit does not occur at the same depth for the various stations. While the best fit for CAR is at 10 km, WES and TRN can be reconciled with a greater depth almost as well, while UME and COL seem to fit the 4 km synthetic much better than than the three-peaked broad waveforms for 10 km depth. The net result of such waveform fit trade-offs among stations gives an intuitive explanation to our results in Figure 34. Although we feel that time domain waveform comparisons are not the best means inversion results should be judged by, we present these waveforms for the benefit of those who like to think in the time domain.

We used this event to illustrate how confidence limits on source parameters, in our case the source depth, can be computed for actual data. We were not interested in the actual mechanism and parameterization of this particular event which may be refined by further study that we are not planning to undertake. Our main point in analyzing this event was also to show that synthetic and data waveforms can give different results even if the waveforms are similar. Based on Monte-Carlo simulations described above, depth estimation with an accuracy of practical utility for events of this size and using the frequency ranges involved in time domain studies of long period body waves would require a fitting at least at the .96 coherence (or correlation coefficient) level. At this level of fitting accuracy we probably could not ignore the receiver crustal transfer functions (as it is done presently in all source inversion studies). Thus, it appears that much more work is needed for producing accurate inversions than that contained in most studies.

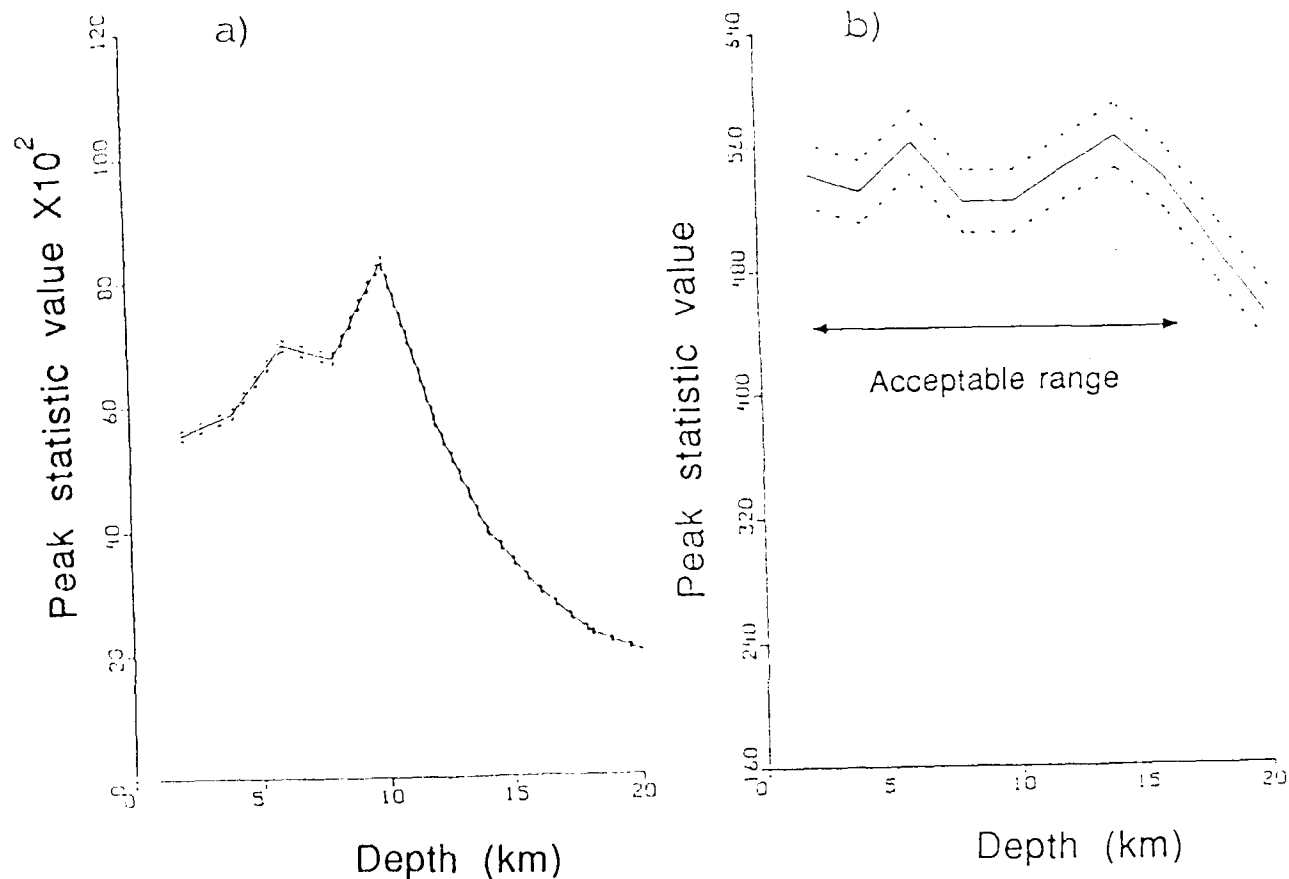


FIGURE 34: a) F statistics computed for the set of synthetic seismograms appropriate to the El Golfo crustal and point source model at 10 km depth as fitted to a wide range of depths. Five percent random white noise was added to avoid singularity in the solution. The dashed lines are approximate 95% confidence limits to the F values. The maximum unambiguously defines a depth of 10 km. b) F statistics computed using the actual P waves from the El Golfo earthquake and fitted to a wide range of depths. The dashed lines are approximate 95% confidence limits. The arrows indicate the large acceptable depth range which is consistent with the F values.

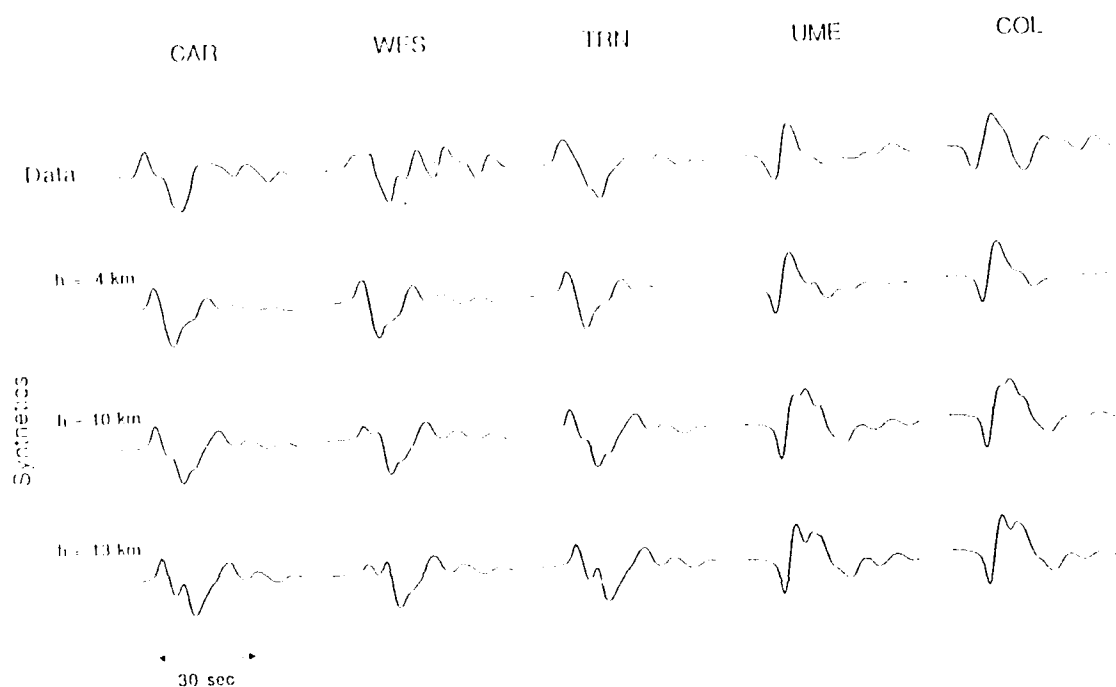


FIGURE 35: Selected data and synthetic seismograms appropriate to various source depths for the El Golfo earthquake. The “best” time domain waveform fits occur at different depths at the various stations.

Imaging of the 1988 Armenian Earthquake

This event was described by Pacheco et al (1989) and was found to be a superposition of three subevents with different source mechanisms (Table 2 in the paper by Pacheco et al 1989). The first of the three subevents occurred near the center of the causative fault break, it was followed by the second subevent located ESE from the first. The third subevent occurred farther west from the first one. In this report, we did not plan to redo all the detailed analyses by Pacheco et al (1989), instead we only attempted to find corroborating evidence for their solution based on our methodology. In order to do that, we have adopted the source mechanisms and depths for their three subevents and tried to verify the triple events by matching each to the P wave data for the eight broadband stations TOL, COL, HIA, BJI, WMQ, LZH, KMI and GAR using equation (15). The data were obtained on a standard distribution tape for this event from IRIS together with the specification for all the instrument responses. Although the three solutions are distinct, they do not appear entirely dissimilar at our eight stations.

Before applying our matching procedures we have, therefore, done some experiments on the synthetic sources we generated. Our synthetics were computed with the source crust model of Pacheco et al (1989), a t^* of 0.7 sec that also used by them, but did not use the trapezoidal source time functions applied in that paper (Pacheco personal communication) since the source time function cancels in the matching process. First of all, we have matched each source model to the space-shifted versions of themselves. This resulted, of course, in peaks placed at the appropriate locations (Figures 36a-c). Besides the peaks there are ridges running SW-NE in these images, these artifacts that are related to the fact that all of our stations are in the NW-SE quadrants and thus, we have poor control over the inferred source locations in the SW-NE direction. Matching the three sources against each other (Figures 37a-c) resulted in cross-matched peaks appropriately

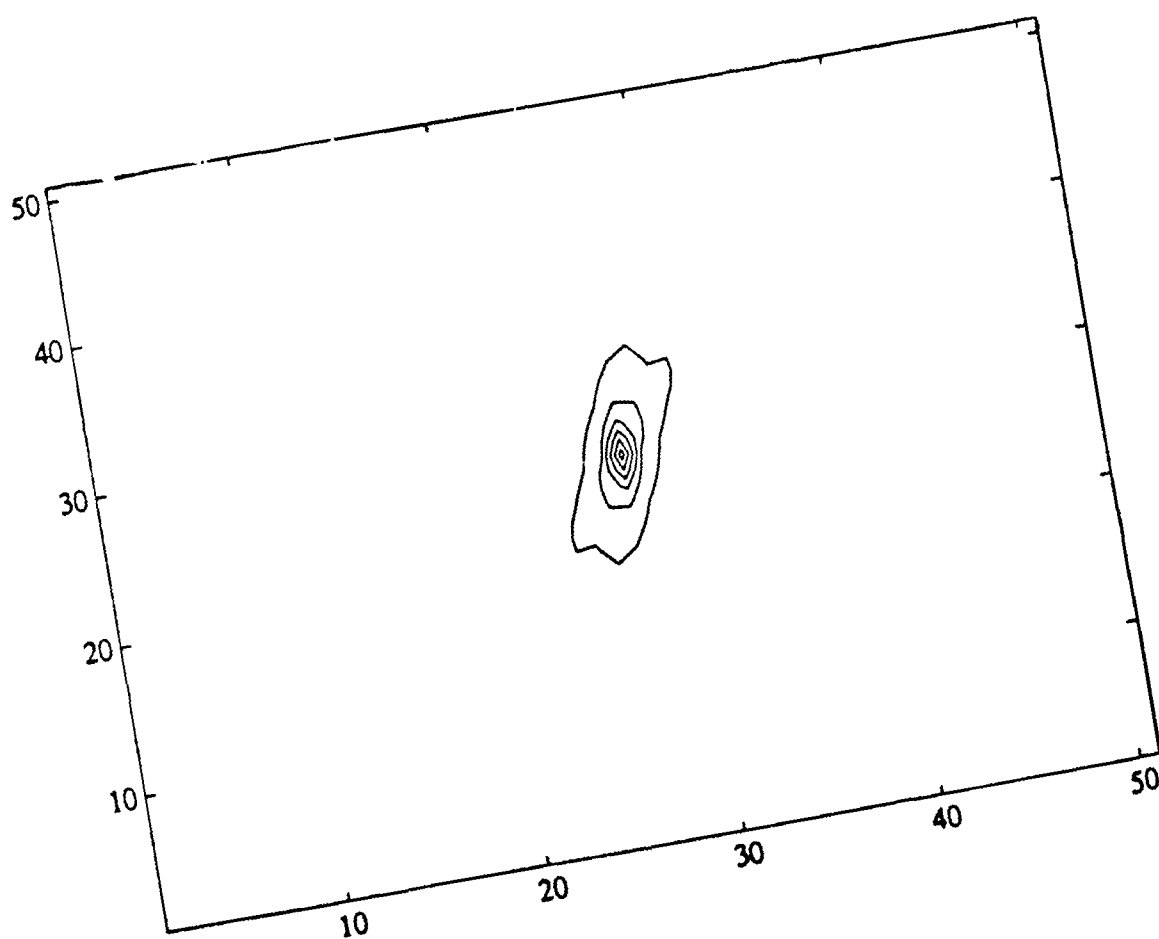
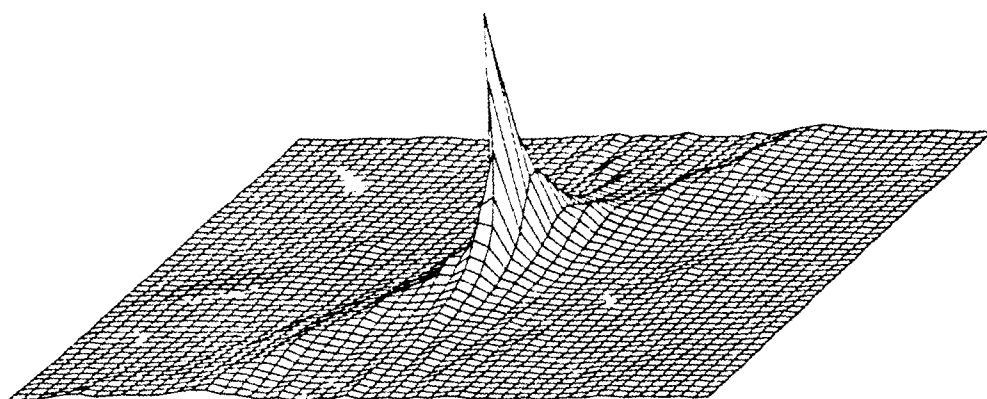


FIGURE 36a: Matching the three subevent source models for the Armenian earthquake against themselves in the 0.1-1.0 Hz range using both perspective views and contour plots. Note that the distance scales are different on the horizontal (EW) and the vertical (NS) axis. a) Subevent 1.

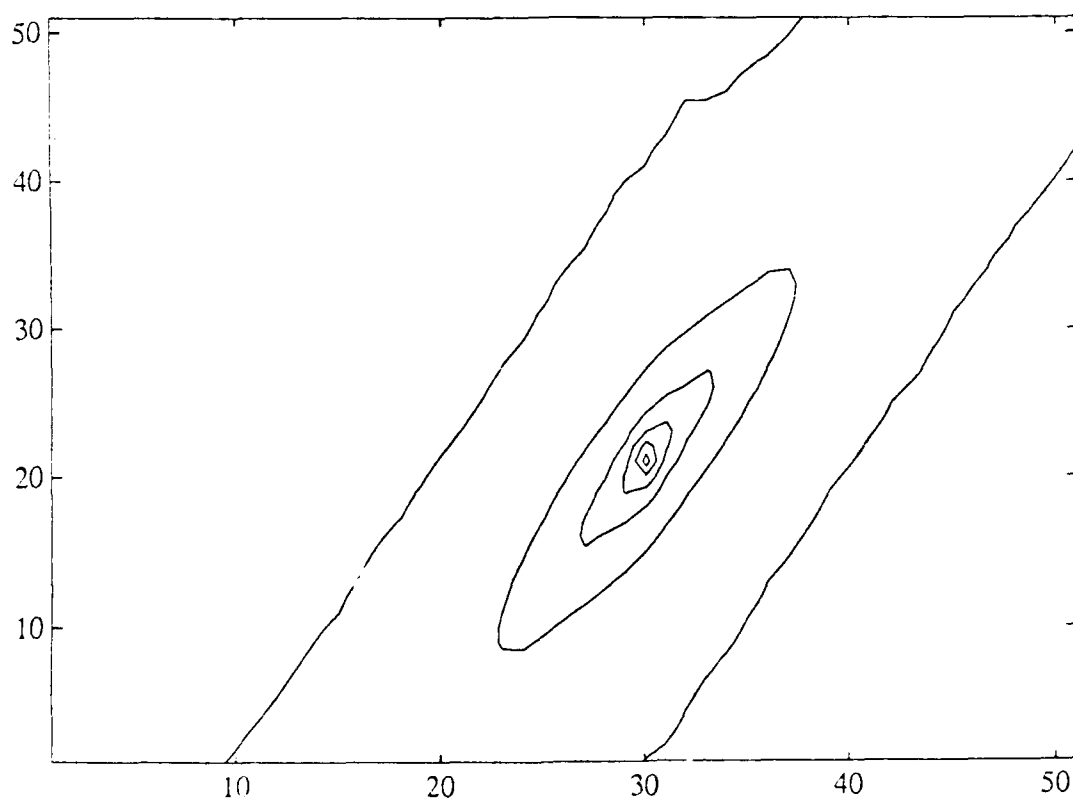
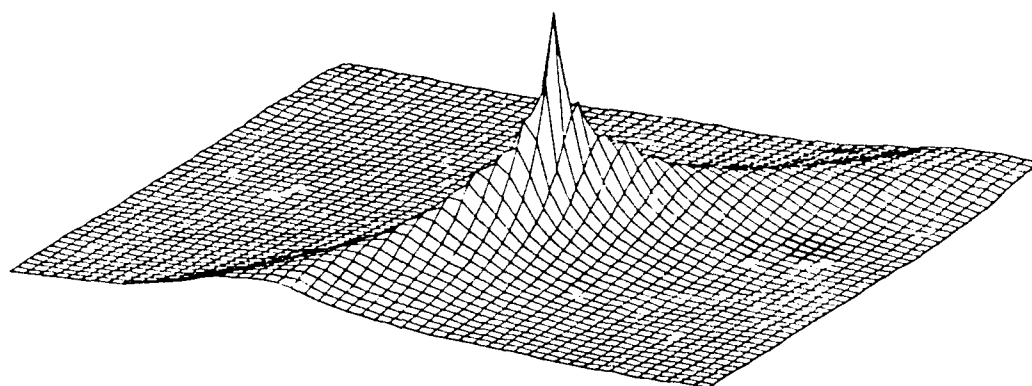


FIGURE 36b: Subevent 2.

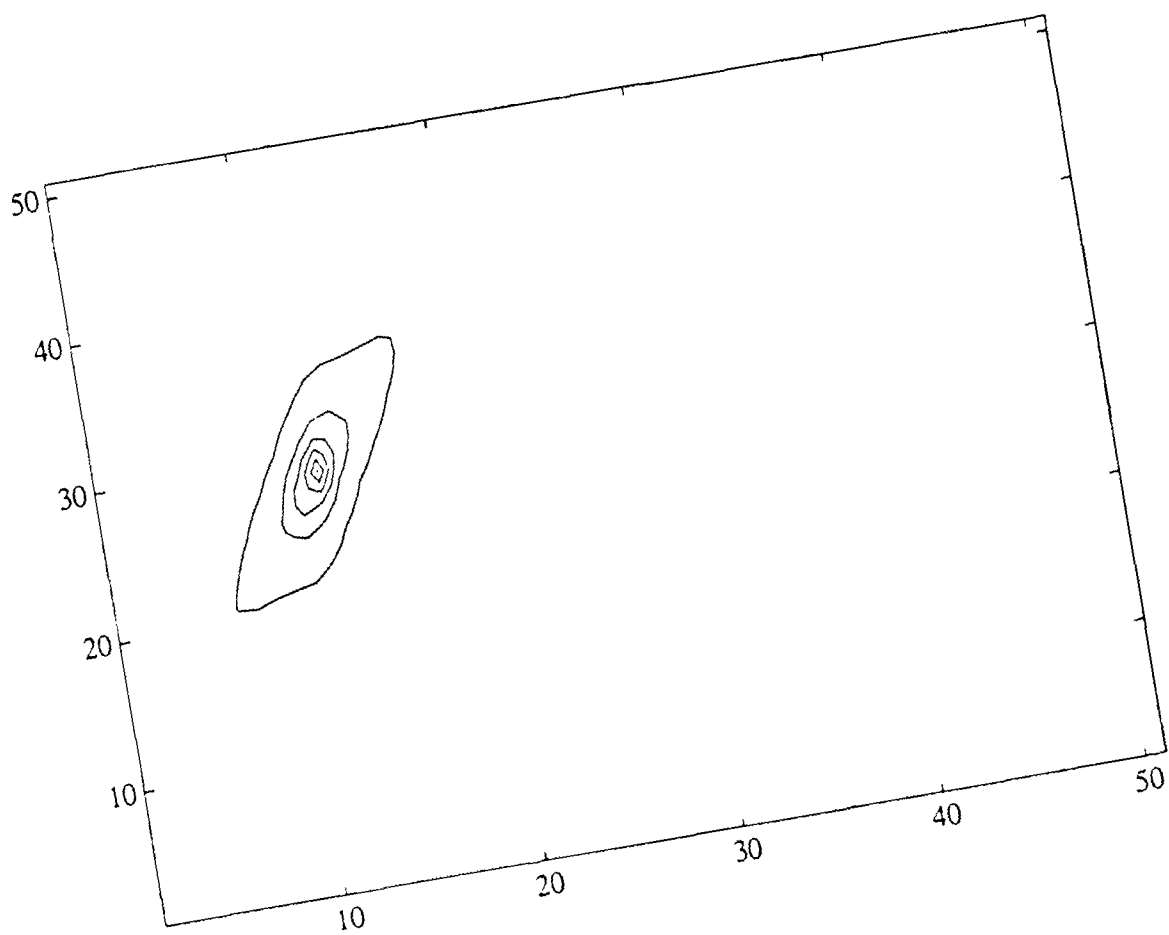
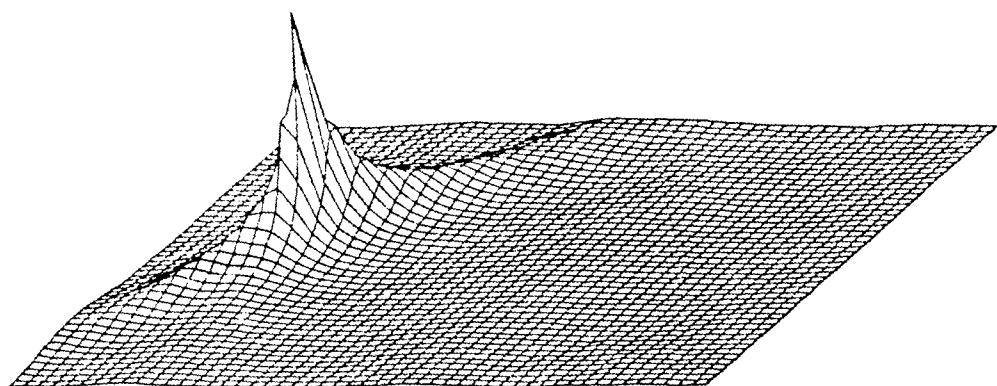


FIGURE 36c: Subevent 3. Perspective views are on top and contour plots of the same surface are below. The sizes of grids are 127.5 km x 127.5 km with 51 subdivisions in each direction.

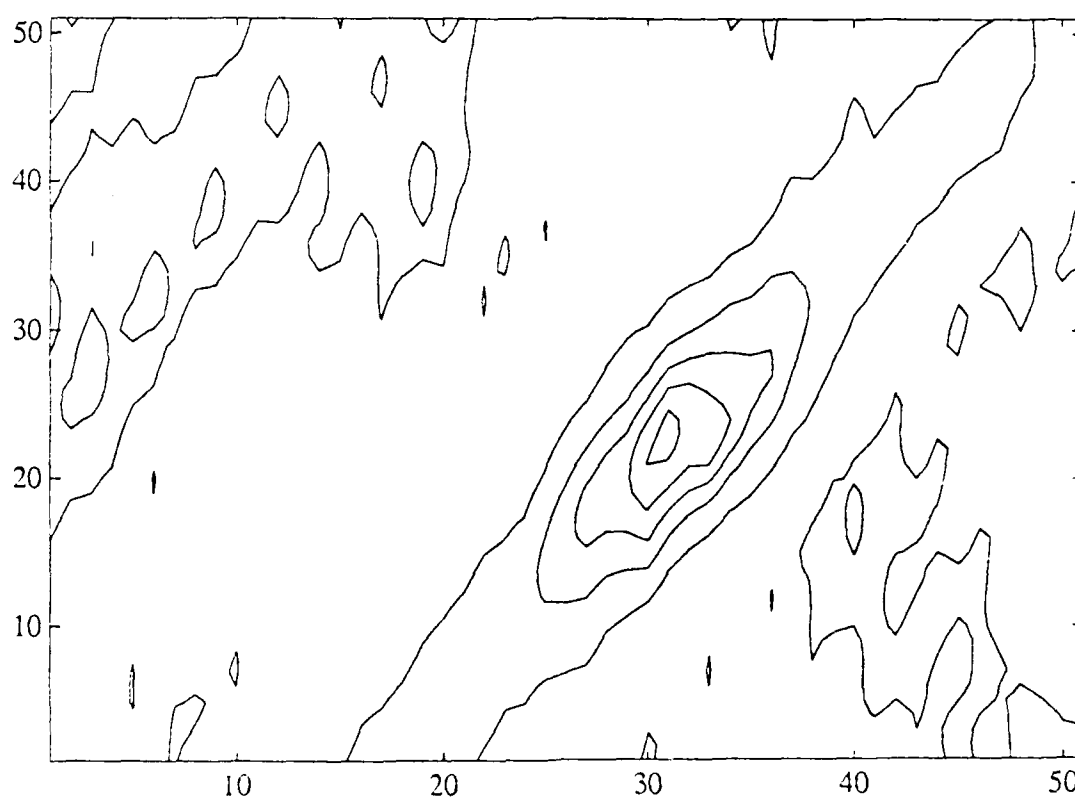
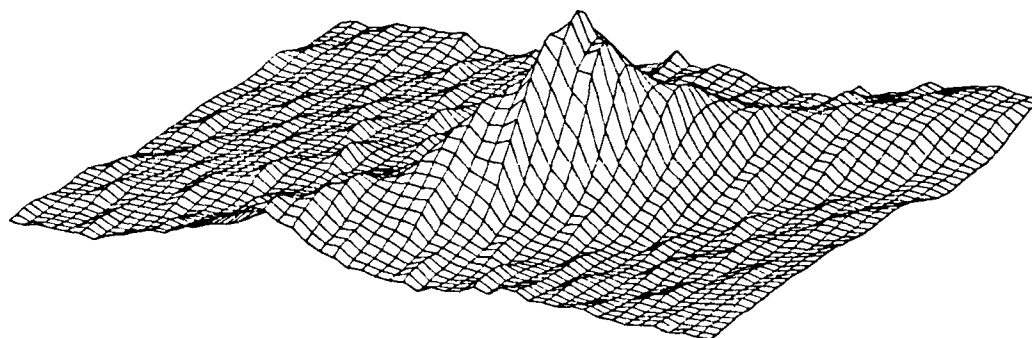


FIGURE 37a: Matching the three subevent source models for the Armenian earthquake against each other in the 0.1-1.0 Hz range. a) Model 2 against Model 1.

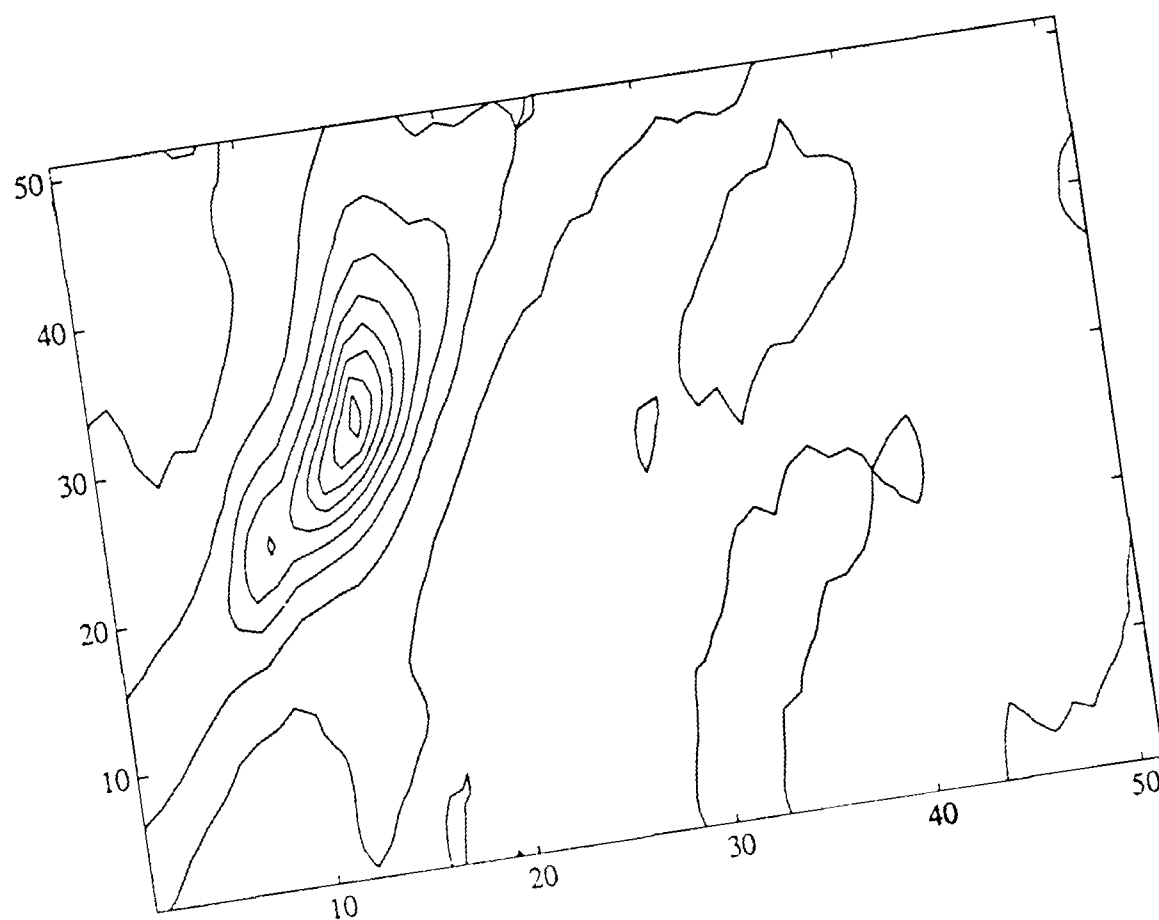
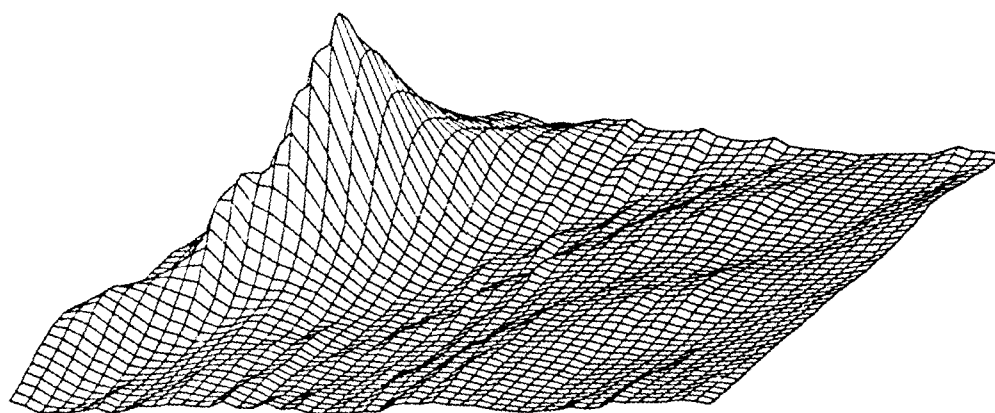


FIGURE 37b: Model 3 against Model 1.

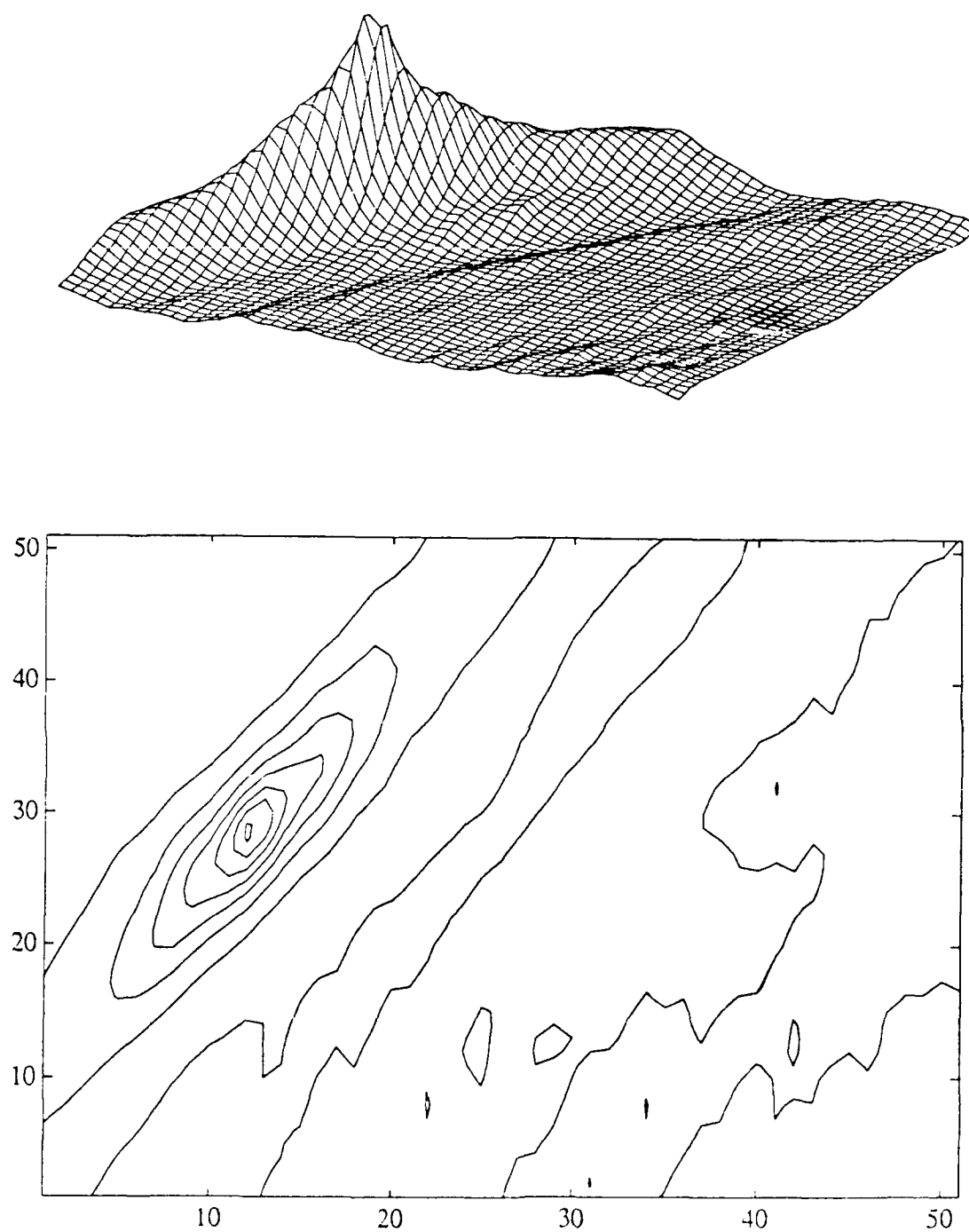


FIGURE 37c: Model 3 against Model 2. Note that the distance scales are different on the horizontal (EW) and the vertical (NS) axis. Perspective views are on top and contour plots of the same surface are below. The sizes of grids are 127.5 km x 127.5 km with 51 subdivisions in each direction.

placed on the positions given by Pacheco et al (1989). It appears that sources 1 and 3 match each other better than source 2 against the other two given this static distribution.

In the next step, we have superposed the three synthetic sources and matched each source against this sum. We succeeded to recover the approximate locations of the individual sources, although the cross-correlation peaks also came into play.

Finally we used the f for each of the individual source type in the matching process on the original data. Instead of deconvolving instrument responses from each seismic trace of the data or constructing broadband traces from several instruments the components of f vectors in equation (15) were made to include the appropriate instrument responses. This approach should have no effect on the results with regards to the spatial structure of the sources, but has the advantage that the effective instruments on the various kinds of seismic recordings do not have to be equalized. Matching the data against the three kinds of point sources (Figures 38 a-c) results in an *EW running ridge* that faintly suggests the trend of the fault thought to be responsible for the Armenian earthquake (Pacheco et al 1989). The peaks matched with subevents 1 and 3 are located at the center and the west end of the fault, respectively, as determined by Pacheco et al (1989). There is no clear indication of subevent 2. Since we have used P waves solely from only eight stations the spatial resolution is poor. We plan to redo this analysis using a much larger data set approximating the scope of the total P and S wave data used by Pacheco et al (1989).

A complete inversion of all the available data from this earthquake is beyond the scope of the work on this project. Since this is a compound source a complete analysis would involve the stripping out of individual sources and test the residual waveforms for the presence of other sources taking into consideration of the reduced degrees of freedom. Moreover, by estimating the time functions of the seismic radiation from various parts of the fault more details about the fault motion could be revealed.

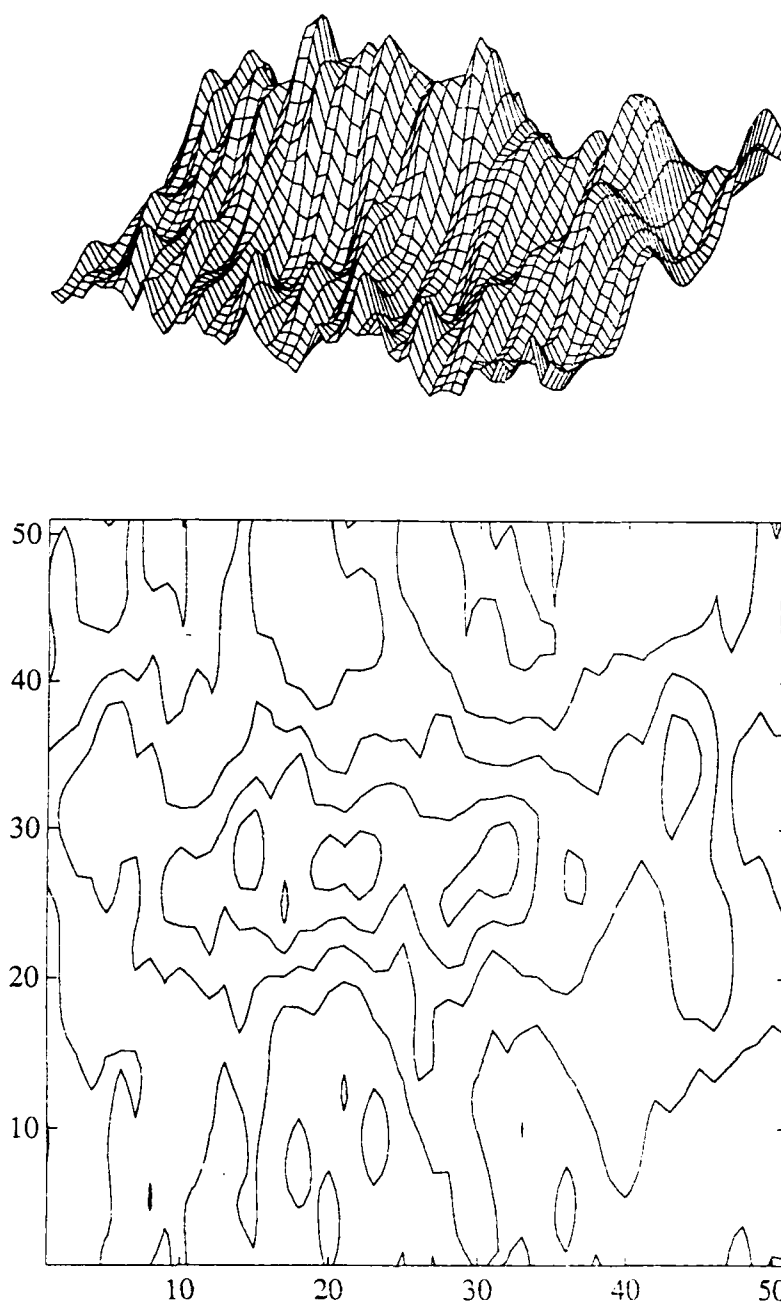


FIGURE 38a: Matching the three subevent source models for the Armenian earthquake against P wave data from eight teleseismic stations in the 0.1-1.0 Hz range. Matching with a) Subevent 1.

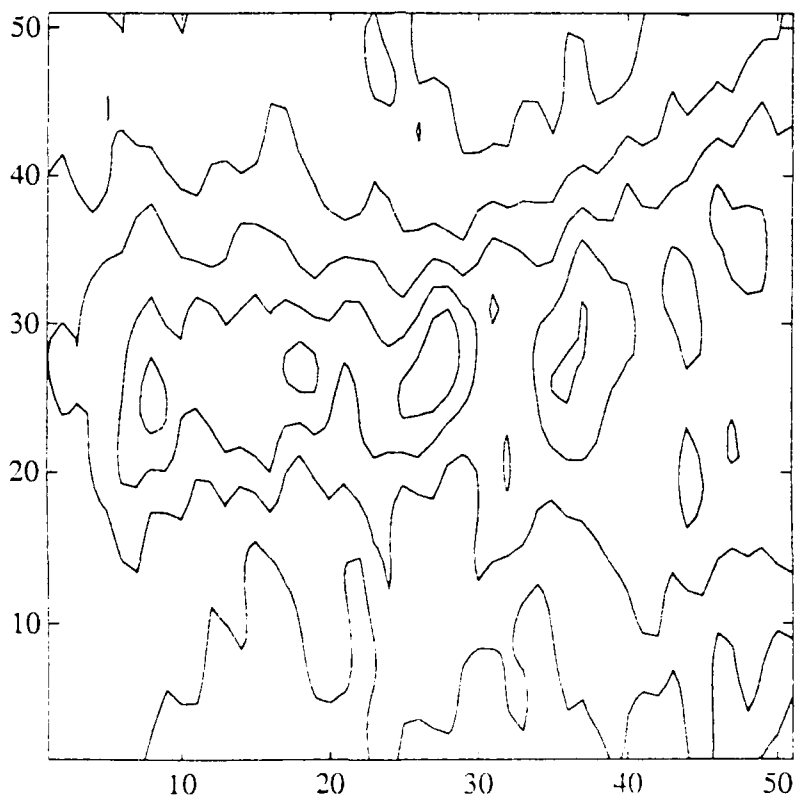
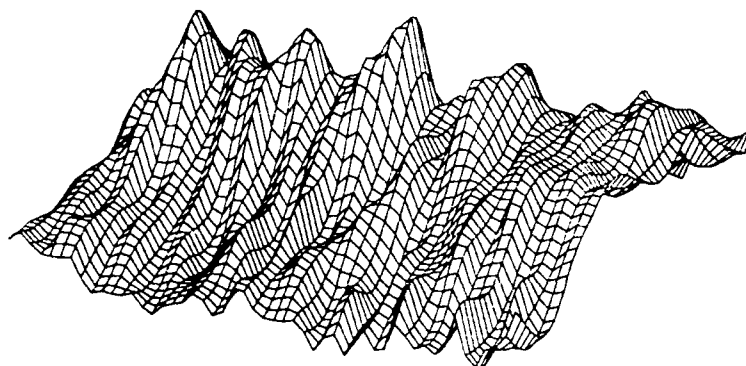


FIGURE 38b: Subevent 2.

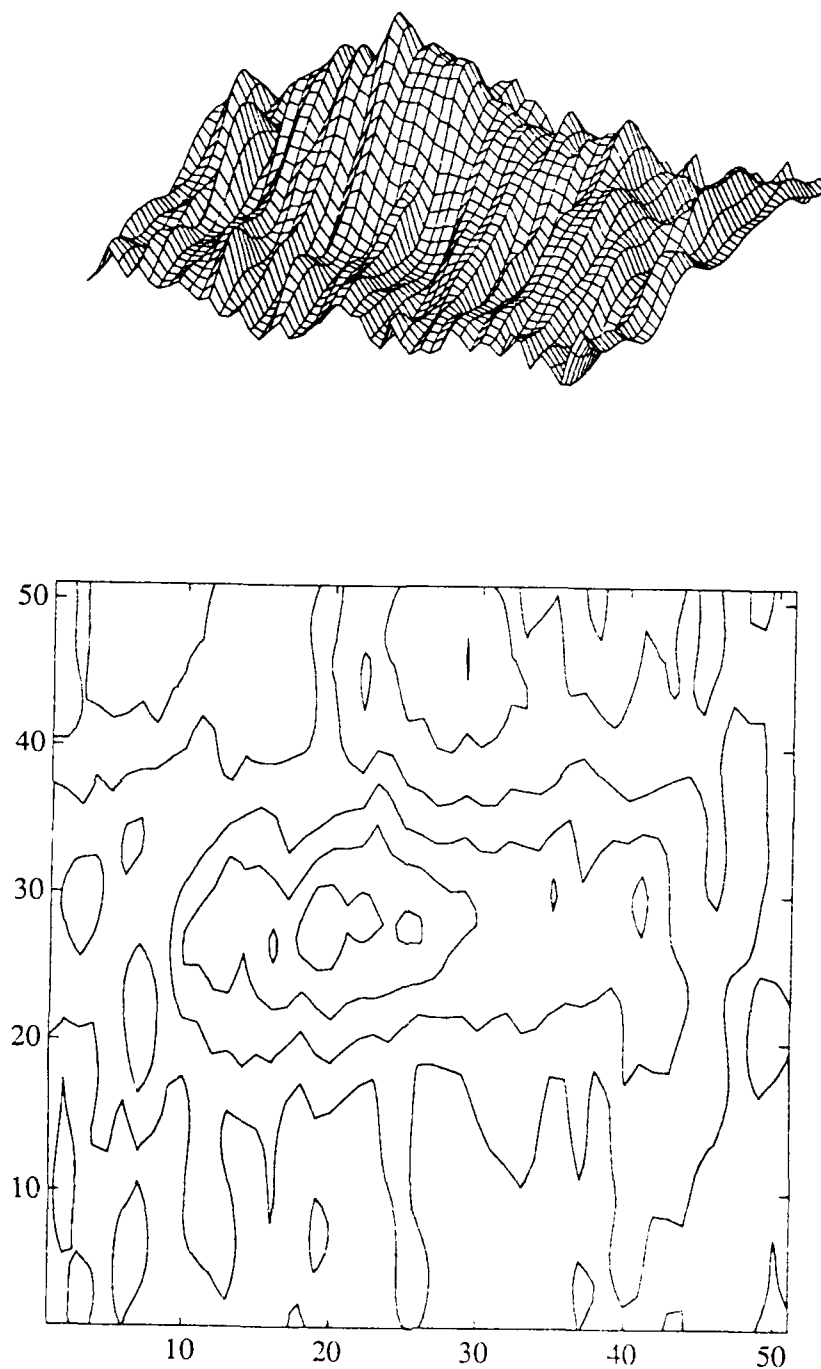
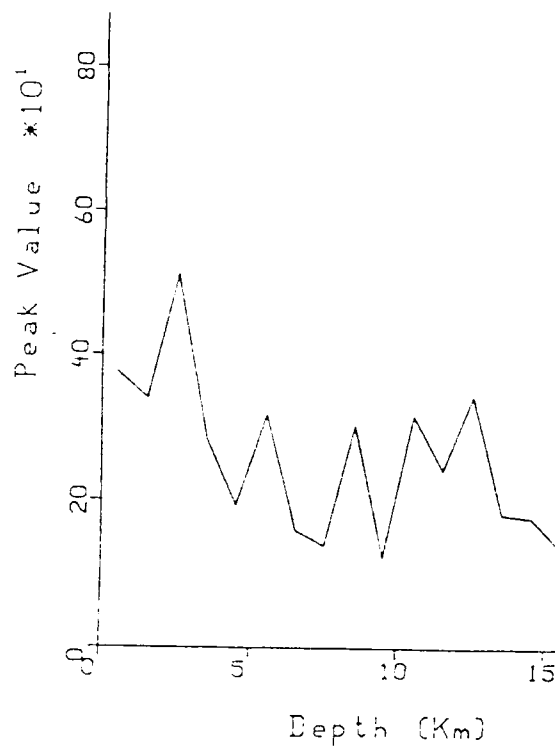


FIGURE 38c: Subevent 3. Note that the dominant feature is a EW trending ridge. Perspective views are on top and contour plots of the same surface are below. The size of grids are 127.5 km x 127.5 km with 51 subdivisions in each direction.

Imaging of selected nuclear explosions at Kazakh

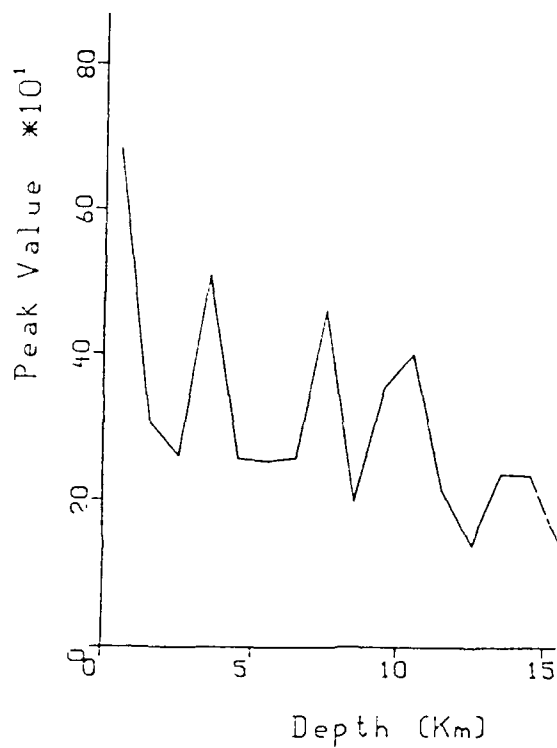
In order to test our scheme of source imaging, we have selected two Kazakh events for which we had deconvolutions at three UK arrays (Der et al, 1987). Taking the deconvolved traces at these three arrays, we have used the model of an explosion source in a half-space to design the f vectors in the procedure. Since we have only three waveforms, complete imaging in the horizontal plane was not practical since it is not possible to make a good image with only three azimuths. Therefore, we have tried to match the depth only. We must point out that while we are trying to match an ideal model the actual deconvolutions may not contain a true pP in the sense of an elastic model. Moreover, even if the simple elastic model were applicable, the bandwidth limitations of the data may not allow us to resolve the true depth. These caveats notwithstanding, if we plot Shumway's statistics as functions of source depth they indicate shallow source depths (Figures 39 and 40). Thus, the deconvolved seismograms best resemble an elastic compressional source at shallow depths; this is more than we can deduce from location calculations at teleseismic distances.

It appears that our imaging procedure may be a good alternative for the discrimination and depth estimation schemes devised by Pearce (1980, 1977) Pearce and Stewart 1989 who also tried to match the various depth phases with amplitude limits obtained from measurements made on seismic records. Our approach differs from his in that we can use the whole seismograms automatically without manual measurements, we also utilize the polarities of phases, but without trying to determine them subjectively, and that we can, in addition, incorporate any available knowledge of crustal structures, no matter how complex, into the scheme by using them to compute the f vectors. The matching procedure will work in spite any complexities in waveforms caused by non-impulsive source time functions. Thus, our new standard method of discrimination will require that we line up the P waves on the first onset (the only manual step), invoke the best crustal response of the source region and match these against sets of f 's computed for explosion



12/25/75

FIGURE 39: Shumway's statistic as a function of depth computed from deconvolved P wave seismograms of the December 25, 1975 Kazakh nuclear explosion.



6/29/77

FIGURE 40: Shumway's statistic as a function of depth computed from deconvolved P wave seismograms of the June 29, 1977 Kazakh nuclear explosion.

sources at various depths in that structure. In more general crustal structures, complexities not explainable to simple depth phases will also be present, and these can also be matched. Good matches (high F values) will designate explosions, poor matches-various crustal earthquakes (because the mismatches in the amplitudes and polarities of the various arrivals, mostly of the depth phases). Deconvolution is not needed for the success of the scheme, because common frequency factors cancel in the process; on the other hand, corrections for unequal path attenuation or instrument responses will be required. Reduction of site effects by array averaging is desirable prior to this process, but does not seem to be absolutely necessary if many stations are being used. Crustal structures have been the subject of studies over many decades and have been mapped all over the world. A database of such structures could be a good accessory to intelligent monitoring systems.

Analyses of surface waves from Kazakh nuclear explosions

We wish to analyze surface waves observed at a set of stations in a similar way, then the components of the f vector become

$$f_i(\omega) = P_i(\omega) \exp [j \omega \hat{k}_i x / c_i(\omega)]$$

In this case the waves are dispersive and the phase velocity depends on frequency, and $P_i(\omega)$ is the source radiation pattern in the direction of the station i . The exponential again describes horizontal source translation in laterally homogeneous models.

The key problem in nuclear monitoring is the separation of isotropic (explosion) and deviatoric (double couple, strain release or block motion) contributions in a set of seismic surface waves. An obvious application is yield estimation from surface waves when tectonic strain release is present. We want to reduce the effects of the double-couple component and estimate the energy

in the compressional source contribution. For this application the Capon's algorithm seems to be the most suitable, since it is essentially a formulation for the energy in an output of a constrained optimum filter designed to reduce the noise (double couple component) and pass the signal (compressional component) undistorted. The original formulation of Capon's F-K algorithm has the inverse noise spectral matrix N instead of that of data S . In most imaging applications (Baggeroer et al, 1988) of the total data spectral matrix containing contributions from both the desired signal and the undesirable noise (strain release in our case) is substituted. This may have serious consequences, however, in the case of mismatch (Cox, 1973). In our simulations of extracting the compressional contribution we shall use the original formulation of Capon (1969) and will use the spectral matrix constructed only from *a priori* estimates of the average strain release sources summed over a range of mechanisms ($\sum d_i^* d_i$) for thrust events of the type typical for Kazakh. According to the literature of Capon's estimator (Cox, 1973) the resulting algorithm that uses a "noise" spectral matrix and does not include the desired compressional source will be more stable and much less sensitive to mismatch. It will be generally possible to obtain some estimate of the average strain release spectral matrix for a test site, although this estimate need not be very accurate. Using this in conjunction with an imperfectly known compressional component, we still should be able to reduce the contribution from the deviatoric component whatever its cause is.

Table VII shows the results of such a simulation where a constant compressional source superposed on variable levels of a strain release source (thrust fault) was processed by Capon's algorithm. The "noise" spectral matrix was constructed of a superposition of thrust fault contributions (that also included the simulated fault used in the input) the fault orientations of which were varied over a range of five degrees to account for the uncertainties and variations in the strain release components. The table shows that the power in the output (signal estimate) did not vary much, although the ratio of the compressional and "strain release" components did. Only at extremely large ratios can we see a breakdown of the process. This indicates that such a processor

could work, despite the uncertainties and variations in the strain release components as long as we have an idea what we need to eliminate. The other major issue, that of the limited ability to distinguish various types of shallow deviatoric sources (Patton, 1988) may also be attacked by similar signal processing methods. In the future, we plan to investigate the associated resolution problem perhaps including long period body waves as well (Cohee and Lay, 1988). In contrast to the presently used painstaking procedures of fitting radiation patterns to the data, estimating and subtracting the strain release components, this procedure can be automated and performed instantaneously after receiving the surface waves from an event.

TABLE VII: Separation of Compressional and Deviatoric Sources with Capon's Algorithm.

Relative deviatoric component	Output amplitude
0.	1.0
0.17	1.0
0.333	0.99
0.5	0.99
1.0	1.1
10.	1.4

The only problem that needs to be solved is to obtain in practice good prior estimates of the compressional and strain release spectral matrices. These can be obtained empirically, either by finding events with low strain release (small Love waves) or manipulating several events with similar strain release mechanisms, but different degrees of strain release. Such procedure involves translating the two events to the same location by phase shifting and differencing their spectra to obtain estimates of a pure compressional source. Such a process would totally eliminate the need

for complex "path corrections." It is possible, however, that the method may not work over larger areas (exceeding 70 km in diameter) due to waveform distortions caused scattering of Rayleigh waves (Rivers and von Seggern 1979). This would not detract from the usefulness of such an approach, since other methods such as that of Stevens (1986) would be also affected by the same problem.

In view of some data problems discovered and described below, in this report we set a less ambitious goal, that of locating three events relative to each other. We assume that the strain release component is negligible. During this phase of the work, we have collected surface wave recordings of Kazakh nuclear explosions at common stations using the databases at the Center for Seismic Studies. We have collected surface wave data for nine Kazakh explosions which were recorded at five common stations ANTO, GRFO, MAT, TATO and KONO. The dispersive phase shifts were estimated from the fundamental Rayleigh wave dispersion curves computed for the Kazakh crustal model given by Stevens (1986). The first test was to verify that the events gave maxima near to their actual locations. This was found to be the case for several of them. In Figure 41 we show the maps of Capon's statistics obtained by using the event with the smallest tectonic release, lowest Love wave energy, as a master event defining the f vector. This seems to confirm the findings of von Seggern (1972) who was able to locate events relative to each other with surface waves with about a 10 km accuracy. However, some other events did not locate well at all. Upon examining the data, we have found that the absolute times given in the database were grossly in error for at least two of the traces. Further inquiries made revealed that people who had used the data before (Richard Baumstark for instance) also experienced problems with the absolute times in some of the CSS databases. While gross errors are easy to notice, smaller errors may go unnoticed and can make any results questionable. Therefore, we decided that we need to verify absolute times for all records we shall use in the future before we attempt anything like the separate estimation of compressional and deviatoric source energy.

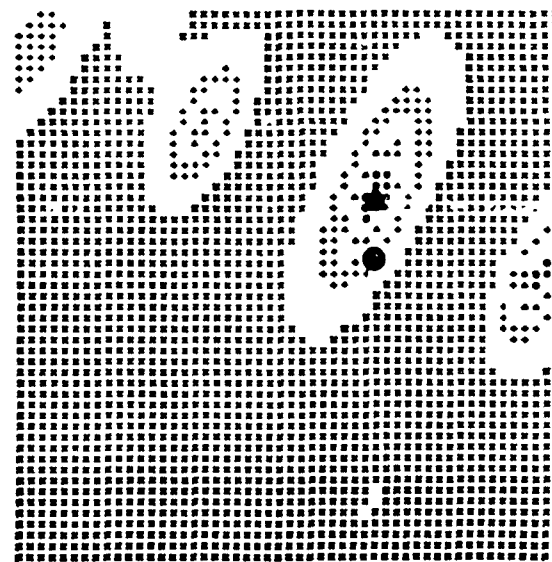
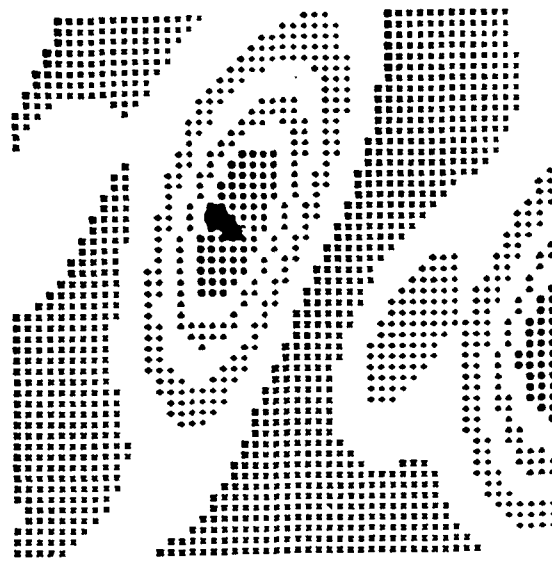


FIGURE 41: Surface wave imaging of two nuclear explosions at the Kazakh test site (October 12, 1980 on top and September 14, 1980 on the bottom) by the Capon algorithm. The geographical coordinates of the centers of the print plot grids are 50N-79E and the events are plotted relative to that. Filled circles denote the locations, obtained from body waves, as listed by unclassified files at the Center for Seismic Studies, triangles show the maxima of the Capon's statistics. The grids are 50 km on each side, and the tops are facing North.

Depth imaging of the 1976 Kazakh earthquake

This March 20, 1976 event was analyzed in some detail by Pooley et al (1983) and was identified as an earthquake. The deconvolutions at three UK arrays resulted in the waveforms shown in Figure 42. The prominent arrivals include P, pP, sP and an early arriving Moho conversion of the S wave. The crustal model used by Pooley et al (1983) consisted of a single layer underlain by mantle. Adapting this model the changes in the depth will only result in time shifts of the three idealized impulsive arrivals. Using the Fourier transforms of the sequence of these four impulses spaced appropriately to the various depths as f and those of the three data traces for d , shown in Figure 43, in the imaging formula we can see how the frequency-compounded F statistic between 0.5-4 Hz changes as a function of depth (Figure 44). We naturally get a prominent peak at the expected result of 20.5 km, having assumed the same structure and phase interpretation as Pooley et al (1983). This is an obvious example with clear depth phases that could be interpreted manually as well and it merely serves as an illustration how such method works. We do not claim that this approach would work so neatly all the time for more complicated events with directionality (Douglas et al, 1990). We must point out, however, that without the deconvolution (or equivalently, beamed phaseless seismograms) the timings and the polarities of the various phases would be much less obvious, and the deconvolution did much to clean up the seismograms. This can be seen in an earlier report of ours where we presented samples of the original seismograms for this event (Der et al, 1987a).

Summary of Section III

It can be shown that time domain studies of long period body waves preferentially fit the low frequency components of signals with adverse effect on the resolution of the spatial characteristics of the seismic sources because of the long wavelengths and limited resolution obtainable from long period signal components. Inversions of long period waveform data for

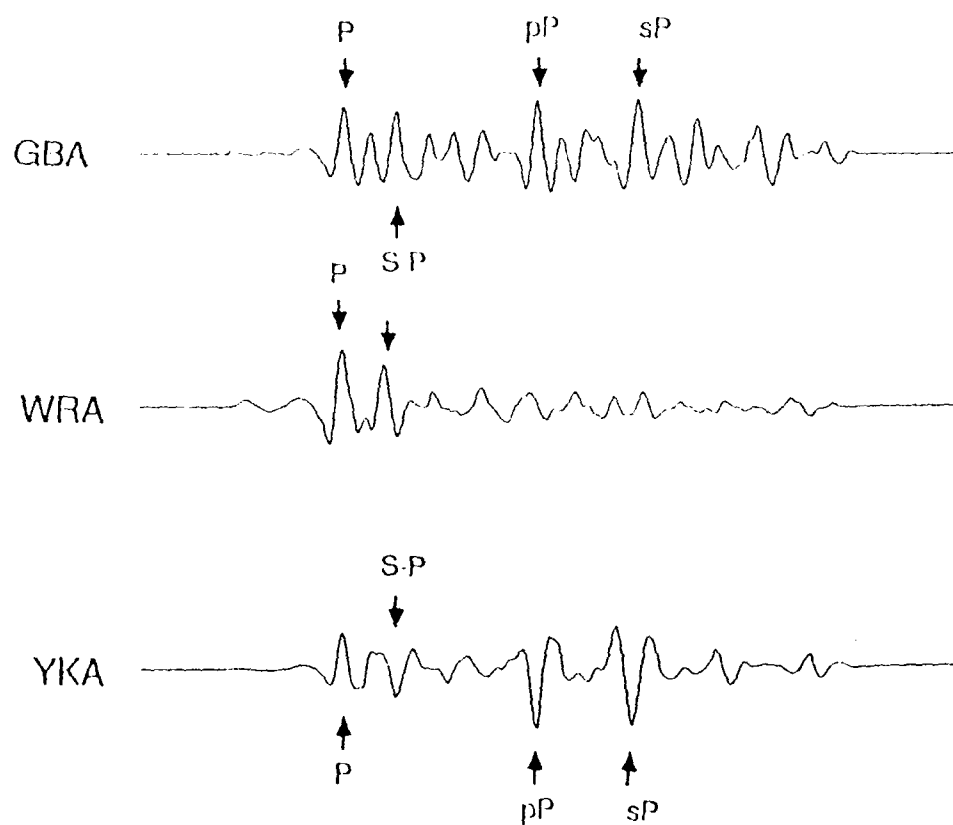


FIGURE 42: Deconvolved waveforms of the Kazakh earthquake at three UK arrays. Besides the surface reflections pP and sP there is an early phase which is probably a Moho-converted phase (Pooley et al 1983).

Depth estimated for a single layer
over halfspace model

$H = 20.5 \text{ km}$

Frequency band 0.5-4.0 Hz

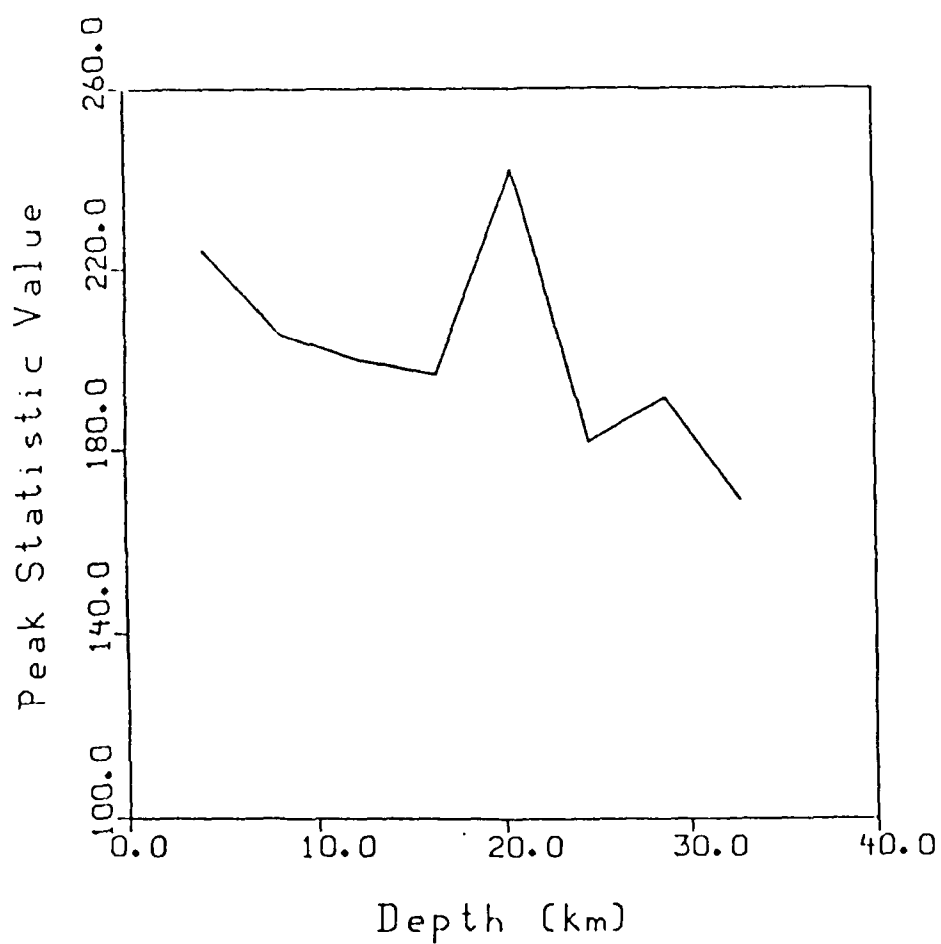


FIGURE 43: Depth imaging of the 3/20/1076 Kazakh earthquake.

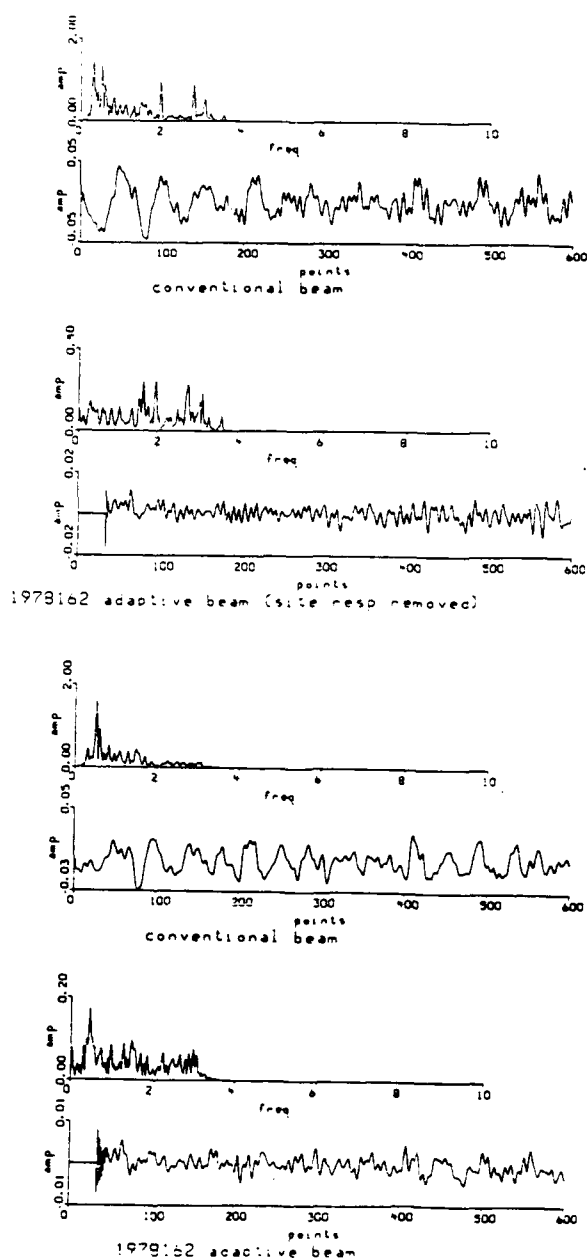


FIGURE 44: Comparisons of noise adaptation without (bottom) and with (top) the site response removed. Comparing the shapes and levels of spectra it can be seen that the overall noise is significantly reduced by the adaptive beaming method relative to the beams, especially below 2 Hz. The adaptive beams quickly adapt to the noise, and after a few oscillations the overall noise levels are much reduced relative to the beam outputs. EKA data was processed.

moderately large events can give only a "centroid" solution without any reliable details in the fault motion. Side-by-side time domain comparisons of data and synthetic seismograms are useful aids for verifying the results, but do not constitute sufficient proof for the validity of the source parameters derived by such comparisons only.

In this report, we present alternative general ways for inverting waveform data. The methods are a general class of pattern matching related in mathematical form to F-K analysis. The methodology has the advantage that, unlike qualitative comparison of data and synthetic waveforms, it provides means for the estimation of error limits and spatial resolution. It also appears potentially quite suitable for automatization of the waveform inversion process. Preliminary applications of the methodology to various types of seismic data, long period and short period body waves and long period surface waves, gave interesting and promising results. A potential application for such algorithms would be the optimum estimation of seismic strain release component in M_S . Nevertheless, much needs to be done to further develop and refine such techniques, especially for compound sources.

4.0 TESTS OF VARIOUS S/N OPTIMIZATION ALGORITHMS

General Remarks

In applying discrimination and yield estimation procedures to measurements made on various teleseismic and regional wave arrivals emitted by the sources, it is important to extend the ranges of detectability and measurability. Commonly, large events will excite body waves, Lg , and long period surface waves that can be seen teleseismically. Smaller events will not have long period surface waves that can be seen above the noise at teleseismic distances, but will still have detectable P waves. Events that are even smaller can be detected only by regional stations and arrays. With decreasing magnitude, the quantity and quality of measurements used as discriminants, diagnostics and yield estimators will also decrease. Therefore, we need techniques that extend the ranges of detectability of various weak arrivals and that enable us to extract broadband information from the data. A family of such techniques includes the various optimum filtering methods. A common trait of many of these is that they were designed to minimize stationary noise while passing ideal, perfectly identical signal waveforms across arrays without distortion (Capon, 1969; Booker and Ong, 1971; Shen, 1979; Kedrov and Ovchinnikov, 1990).

Past attempts of optimum filtering were characterized by performance which was far below that predicted from idealized theoretical signal and noise models (Capon, 1969; Booker and Ong, 1971). There were basically two reasons for this. The first one was that signal waveforms are not exactly identical across arrays, this led to degradation (beam loss) in the performance of optimum filters (Cox, 1973). The result was that beam loss often cancelled the gains in reducing the noise level resulting in no or negligible net S/N gain. The second was that the background noise is generally not stationary and the noise models derived from large data blocks were not realistic. Recognizing the nature of the second factor several workers have started to apply adaptive filtering methods with relatively fast adaptation rate.

Applying such techniques to small arrays where the signal waveform variability was not a major problem significant S/N gains were indeed achieved (Widrow, 1966; Shen, 1979). He found that the noise reduction exceeded that of the conventional beamforming. The filters were designed on the basis of perfect similarity of seismic signals. This assumption is not correct for most arrays, as we have pointed out above.

In this report we are investigating the effect of increasing the signal similarity by factoring out the site responses prior to applying the technique of adaptive filtering. The factoring out of site

responses will, of course, change the noise coherence structure also, and we rely on the adaptation of the filter to adjust to this changed structure. After removing the site responses, we can assume with more justification that the signals are perfectly coherent. This will reduce the "beamloss" (Cox, 1973) to much lower levels.

The last issue is that of the computational costs associated with the introduction of any such relatively elaborate schemes. In the past, such considerations were very important because computers were expensive and slow and the available memory or disk space limited. This was a major reason, besides the problems discussed above, why optimum filtering methods fell out of favor during the early seventies. With the advent of cheap and fast computers even moderate S/N gains seem to be worthwhile, even if part of the time no net S/N gains result relative to simpler processors. It can be shown that we would never do worse than a simple beam processor since optimum processors degrade into simple beams when the noise is uncorrelated. Based on some limited randomly chosen actual signal and noise situations we have found, however that net S/N gains (over simple beaming) of 4-6 dB are quite common. Such improvements in the output S/N seem to be worthwhile.

Processing of Teleseismic P Waves Recorded at Large Seismic Arrays

For testing our approach, we have used recordings of a set of Kazakh (Shagan River) P waves recorded at EKA and estimated the site effects by applying our deconvolution procedure to the seismograms listed in Table VIII. Subsequently, we factored out the site effects and applied Shen's algorithm to the result. In order to test the effect of the algorithm on the noise alone, we have applied the noise-adaptive filter to the noise preceding the signals.

**TABLE VIII: List of Kazakh Events
Recorded at AWRE EKA Array**

Event	Origin Time	Lat (N)	Lon (E)
1978241	04:26:75.9	49.82	78.14
1978162	02:56:57.6	49.90	78.80
1977334	04:06:57.4	49.96	78.89
1976342	04:56:57.4	49.96	78.85

We performed this test on noise samples with and without the site effect correction. Figures 45 to 47 show that noise adaptation reduces the noise amplitudes relative to the conventional beam throughout the frequency range of 0-4 Hz, but the noise reduction is most effective below 1 Hz. The removal of site effects did not impair the effectiveness of noise-adaptation. The filter adapts quickly (as evidenced by a few large oscillations in the output after the noise amplitude falls off).

Applying the process to windows containing signals shows that the noise was reduced to a level below visibility in this high S/N sample by the adaptive process, while the noise is clearly visible on the beams (top traces in Figure 46). Obviously, this example has no practical use, since the signal is much larger than the noise in the case shown. It must be pointed out, however, that the relative noise reduction is the same regardless of the relative signal size (the site-equalized process will be unaffected by the presence of large coherent signals). Thus, a weaker signal would have stood out much better on the trace processed by the same procedure than on the beam and the result would be much better suited for any further analyses of the signal.

It is also interesting to look at these noise reduction results in the frequency domain. In Figure 46 we show the differences in the output on signal windows when the adaptive beam algorithm is applied with and without site effect correction. The figure shows that without the site effect correction the signal output is considerably less with adaptive beaming than with conventional beaming (a). This is not surprising, since the adaptive beam process will reduce the signal output if the signals are not matched. After site-equalization is performed, this signal loss is much less severe (b). Since the noise reduction of adaptive beaming remains more effective, even after applying site-equalization, than the conventional beam, the resulting overall S/N ratio improvement will be better for the adaptive beam combined with site-equalization (Figure 47). Thus, this combined process appears to be superior to the conventional beaming process. The gain is achieved at a considerable expense in processing complexity, but it may be justified in special cases when we want to learn more about smaller events at teleseismic distances. Such procedures may be part of a toolbox for more detailed investigations.

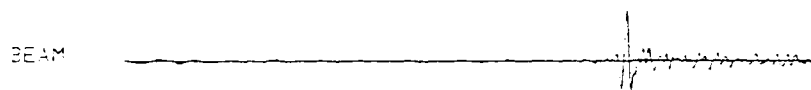


7.1 SEC 0.96 CTS C-P

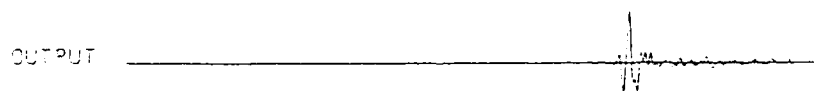


7.1 SEC 0.97 CTS C-P

EKA-KAZAKH (79152) Filtered .4-3.0 Hz



7.1 SEC 0.98 CTS C-P



7.1 SEC 0.75 CTS C-P

EKA-KAZAKH (79152) site response removed. Filtered .4-3.0 Hz

FIGURE 45: Teleseismic P waves recorded at EKA processed by beaming and adaptive filtering with and without removal of site frequency responses.

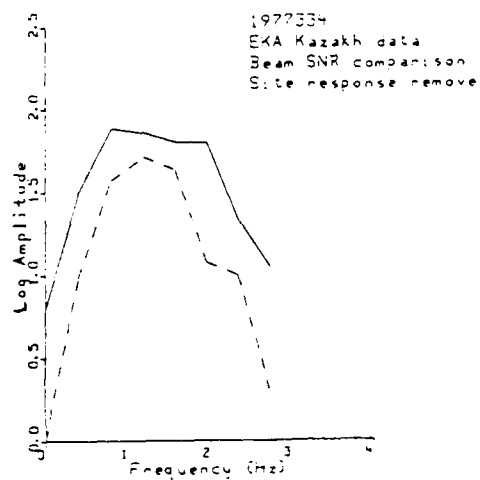
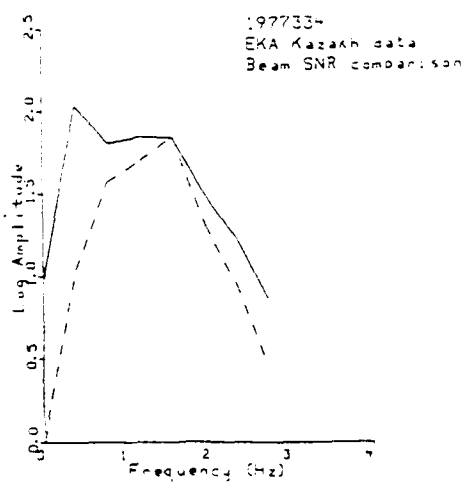
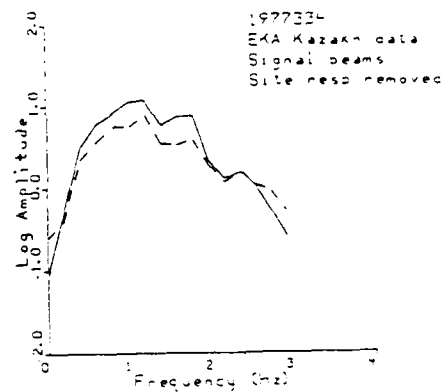
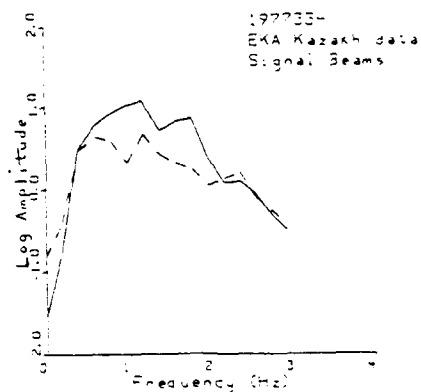


FIGURE 46: Spectra representative to the signal beam loss (top) and the S/N gain obtained for two events by using the four modes of processing described in the text.

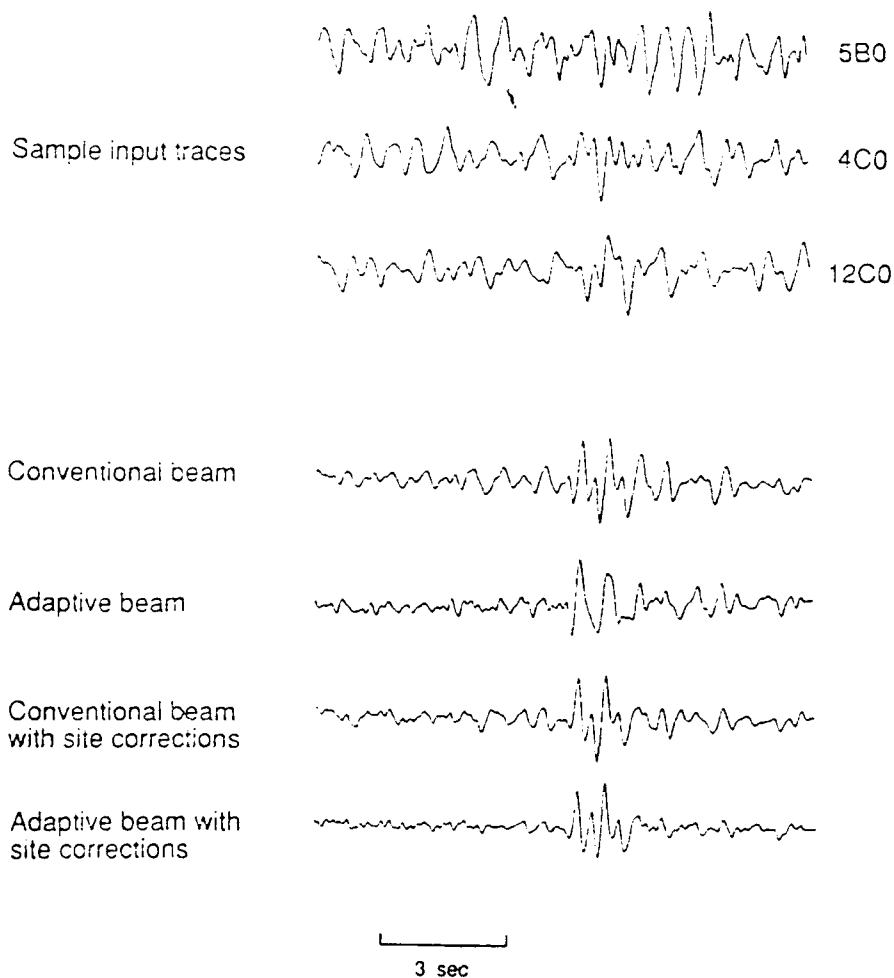


FIGURE 47: Optimum processing of the nuclear explosion Mast, overlain by added amplified actual background noise, at NOR SAR. The best performance, about a 2:1 S/N gain, is associated with site equalization followed by adaptive beaming (bottom trace). It must be pointed out, that contrary to any superficial appearances, this is not equivalent to frequency filtering since this process works by spatial filtering only and does not change the spectrum or waveforms of any signals.

Another example of this kind of signal processing is that of the P waves from the NTS nuclear explosion Mast recorded at NORSAR. To simulate noisy conditions, we have amplified background noise preceding the event and added it to the respective traces of the array recording. The site response functions were obtained by factoring a suite of original, high S/N recordings of NTS nuclear explosions at NORSAR. Thus, we are simulating the case of enhancing a weak event by utilizing pre-stored high-quality site response functions in conjunction with adaptive filtering. In this simulation, we have utilized 12 sensors of NORSAR spread out across the reduced array. Figure 48 shows some of the original, unprocessed traces on the top and the results of four kinds of processing. It is clear that the combination of the site-equalization and the adaptive noise filtering gave the best result.

Processing of Western Norway Earthquakes Recorded at NORESS

Similarly to teleseismic signals, we have done a limited amount of work testing the suitability of adaptive beaming and site-equalization methods for enhancing regional Pn arrivals. Pn arrivals are generally emergent at regional distances and are much smaller in amplitude than Lg or Sn . Enhancing Pn arrivals may be quite useful in discrimination studies. The methodology followed is identical to that described for teleseismic P elsewhere in this report. The method was tested using a set of Pn arrivals from western Norway earthquakes. A list of these events is given in Table IX. The site effects were estimated from applying the factorization procedure using the multi-channel deconvolution program (Der et al, 1987). Applying the adaptive beaming program to the noise alone (Figure 48) shows that the site response removal somewhat degrades the relative performance improvement due to the adaptive beaming process. On the other hand, the decrease in signal loss through the process appears to compensate approximately for this loss. The net result is that the best strategy seems to be to apply adaptive (not conventional) beaming either with or without site corrections. We must add that this test was done before we realized the extreme sensitivity of site factors to azimuth, and the western Norway earthquakes may be too scattered in azimuth to get stable and effective site correction factors. In any case, the adaptive beaming process appears to be better than conventional beaming for regional signals.

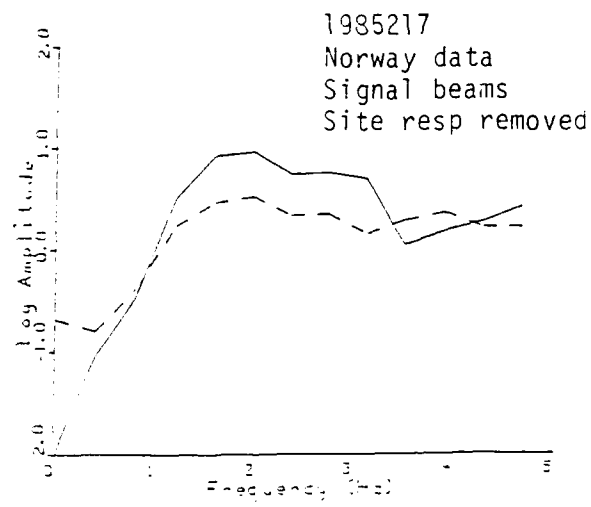
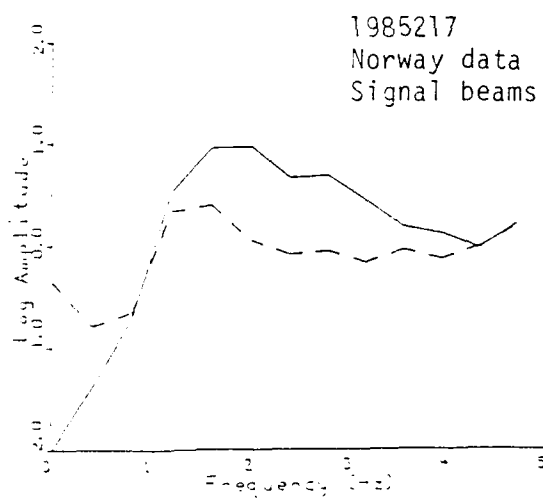
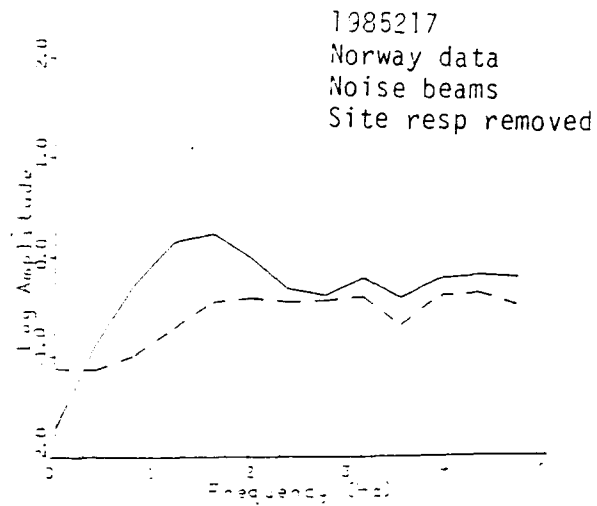
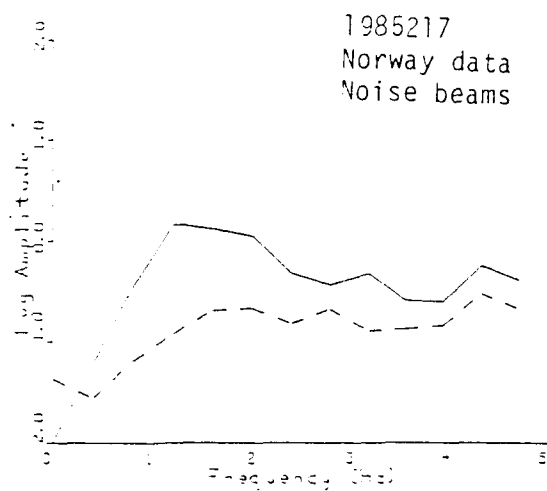


FIGURE 48: Noise reduction gain and beam loss for western Norway earthquakes as processed by beaming and adaptive filtering with or without removing the site transfer functions.

TABLE IX: List of Western Norway Events Recorded at NORESS

Event	Origin Time	Lat (N)	Lon (E)
1985217	17:42:58.7	59.3	6.59
1985218	17:50:07.9	59.3	6.95
1985290	10:00:00.4	59.3	6.95

CONCLUSIONS

Work during this contract revealed the great potential in the applications of various statistical time-series analysis methods for solving seismological problems relevant to nuclear monitoring. In our study of the coherence structure regional seismic waveforms, extending the concept of spectral factorability of teleseismic body wave data (Filson and Frasier, 1972), we have demonstrated that spectra of regional phases can also be decomposed into source and recording site factors provided that the signals originated from a limited source region. Groups of events located close to each other can be identified by the fact that their waveforms can be reconstructed from their spectral source and site factors.

In addition, it was also found that events within such factorable groups could be further subdivided according to relative inter-event coherences between them. The events which show high inter-event coherence are probably both close to each other and have very similar source mechanisms, albeit different source time functions. The opposite must be true for events that do not show high coherence. Cross-event equalization filtering between coherent events using short time domain filters resulted in increases in waveform similarity, and no such increase seemed possible between events pairs with low inter-event coherence.

Site transfer functions between sensors located at the extreme ends of NORESS appear to be complex, describable only with transfer functions with impulse responses longer than a second. Assuming the same degree of crustal heterogeneity for a source region this may imply changes in waveforms similar in nature over small displacements of source location.

Analyses of the coherence properties of suites of regional waveforms for Pn and Lg can be used for:

- a) Identifying very closely spaced events with similar source mechanisms.
- b) Identifying closely spaced events with different source mechanisms (possibly attempts of evasion).
- c) Identifying larger spatial separations in events, not detectable by standard location methods.

In the second part of this report, we re-examined some aspects of estimating secondary arrivals (pP, spall, etc.) in teleseismic P waves. A popular model (P+pP model) often used for interpreting P waves from nuclear explosions and deriving pP parameters consist of a site function convolved with a P and pP pulse sequence and some explosion source pulse (Lay, 1985; Murphy, 1989). Frequency domain analyses of data variance show that this model cannot explain a significant portion of the energy (30-40%) in the P waves from Pahute Mesa events for which such analysis methods were previously applied. Spectral factorization, which does not assume the P+pP model, on the other hand, accounts for 90-95% of the energy in both Pahute Mesa and Kazakh events. Therefore, the complex source waveforms often seen in multi-channel deconvolved P waves from nuclear explosions at both Pahute Mesa and the Kazakh test sites *are required for explaining the data* and reflect the actual complexity of P waves radiated from nuclear explosions. It is shown that magnitude-yield relationships appropriate to the generic pP characteristics derived from multi-channel deconvolutions of nuclear explosions (and appropriate t^*) are similar to those directly derived by regression analyses of m_b data and published yields of nuclear explosions for Pahute and Kazakh test sites by Jih (1990).

In the third section of this report, we have derived some new approaches for imaging seismic sources and seismic source inversion. The methods are based finding the maxima of statistics that are closely related to those used in F-K analyses as functions of source parameters. The method is quite general, it uses Green's functions in conjunction with waveforms of various types of arrivals. Such can be used for inverting both body and surface waves for source parameters in a semi-automatic fashion without subjective visual or RMS comparisons of synthetic and data waveforms. These algorithms also provide a means for evaluation of the performance of time domain direct modelling and source inversion methods as currently practiced. Our analyses indicated that the time domain fits using long period data are generally not precise enough to

resolve the source depth to a few km and other spatial details with the accuracies often claimed, but can only give "centroid" solutions. Other simulations indicated that the same approaches can create reasonably resolved images of faults and can be used for the separate estimation of compressional and strain release components of energies from explosions.

Our source imaging-inversion methodology was applied to two deconvolved Kazakh nuclear explosions and the 1966 El Golfo, the 1988 Armenian and 1976 Kazakh earthquakes. The method identified both explosions as shallow, with depths below 5 km, and the depth estimate for the El Golfo and Kazakh earthquakes event turned out to be 14 km and 20.5 km. These are reasonable results indicating that such methods could be applied for seismic discrimination. Imaging the Armenian earthquake gave a linear feature close in orientation to the actual fault inferred as the source of this event. Imaging Kazakh explosion sources using surface waves was hampered by demonstrably erroneous absolute timing information in the CSS data we retrieved.

In the last section of this report, we explored applications of combined adaptive filtering and site-effect compensation processing schemes to teleseismic (UK array) and regional (NORESS) data indicated that such methods can significantly enhance the signal-to-noise ratios (by 4-6 dB) for P (Pn) arrivals should such computer-intensive analyses prove to be desirable for an event.

5.0 REFERENCES

- Aki, K. and P.G. Richards (1980). *Quantitative Seismology*. W.H. Freeman & Co., San Francisco.
- Anderson, D.A. and B.W. Stump (1989). Seismic wave generation by quarry blasts. In "Quantification of explosion source characteristics from near source, regional and teleseismic distances", Southern Methodist University, GL-TR-89-0194. ADA216218
- Baggeroer, A.B., Kuperman, W.A. and H. Schmidt (1988). Matched-field processing: Source localization in correlated noise as an optimum parameter estimation problem. *J. Acoust. Soc. Am.*, **83**, 571-587.
- Bakun, W.H. and L.R. Johnson (1973). The deconvolution of teleseismic P waves from explosions Milrow and Cannikin. *Geophys. J. R. Astr. Soc.*, **34**, 321-342.
- Baumgardt, D.R. and K.A. Ziegler (1988). Spectral evidence for source multiplicity in explosions, application to regional discrimination of earthquakes and explosions. *Bull. Seism. Soc. Am.*, **78**, 1773-1795.
- Barker, T.G., Day, S.M., McLaughlin, K.L., Shkoller, B. and J.L. Stevens (1990). An analysis of the effects of spall on regional and teleseismic waveforms using two-dimensional numerical modeling of underground explosions. GL-TR-90-0126, S-Cubed, La Jolla, CA, SSS-TR-90-11536. ADA226921
- Bendat, J.S. and A.G. Piersol (1966). *Measurement and Analysis of Random Data*. John Wiley & Sons.
- Booker, A. and C-Y. Ong (1971). Multiple constraint adaptive filtering. *Geophysics*, **36**, 498-509.
- Box, G.E.P. and G.M. Jenkins (1978). *Time Series Analysis: Forecasting and Control*. Holden Day.
- Byrne, C.L., Brent, R.T., Feuillade, C. and D.R. DelBalzo (1990). A stable data-adaptive method for matched-field array processing in acoustic waveguides. *J. Acoust. Soc. Am.*, **87**, 2493-2502.
- Capon, J. (1969). High resolution frequency-wavenumber analysis. *Proc IEEE*, **57**, 1408-1412.
- Cohee, B.P. and T. Lay (1988). Modeling teleseismic SV waves from underground explosions with tectonic release: Results for southern Novaya Zemlya. *Bull. Seism. Soc. Am.*, **78**, 1158-1178.
- Cox, H. (1973). Resolving power and sensitivity to mismatch of optimum array processors. *J. Acoust. Soc. Am.*, **54**, 771-785.
- Der, Z.A., McElfresh, T.W. and A. O'Donnell (1981). Results of the SDCS (Special Data Collection System) attenuation experiment. VSC-TR-81-14, Teledyne-Geotech, Alexandria, VA.
- Der, Z.A., Shumway, R.H., Anderson, L.M., McElfresh, T.W. and J.A. Burnett (1983). Analysis of estimators for pP times and amplitudes. VSC-TR-83-17, Teledyne Geotech, Alexandria, VA.

Der, Z.A., McElfresh, T.W., Wagner, R. and J. Burnetti (1985). Spectral characteristics of P waves from nuclear explosions and yield estimation. *Bull. Seism. Soc. Am.*, **75**, 379-390. Also Errata. *Bull. Seism. Soc. Am.*, **75**, 1222.

Der, Z.A., Lees, A.C., Chan, W.W., Shumway, R.H., McLaughlin, K.L., Smart, E., McElfresh, T.W. and M.E. Marshall (1987a). Maximum-likelihood multi-channel deconvolution of P waves at seismic arrays. *TGAL-87-3*, Teledyne-Geotech Alexandria Laboratories, Alexandria, VA.

Der, Z.A., Shumway, R.H. and A.C. Lees (1987b). Multi-channel deconvolution of P waves at seismic arrays. *Bull. Seism. Soc. Am.* **77**, 195-211.

Der, Z.A., Shumway, R.H. and A.C. Lees (1988). Frequency domain coherent processing of regional seismic signals at small arrays. *Bull. Seism. Soc. Am.* **78**, 326-338.

Der, Z.A., Hirano, M.R. and R.H. Shumway (1990). Coherent processing of regional signals at small seismic arrays. *Bull. Seism. Soc. Am.*, **80B**, 2161-2176.

Douglas, A., Hudson, J.A. and V.K. Kembavi (1971). The relative excitation of seismic surface and body waves by point sources. *Geophys. J. R. Astr. Soc.*, **23**, 451-460.

Douglas, A. (1981). Seismic source identification: A review of past and present research efforts. In *"Identification of Seismic Sources- Earthquake or Underground Explosion"*. E.S. Husebye and S. Mykkeltveit Editors. Reidel Publishing Company.

Douglas, A., Marshall, P.D. and J.B. Young (1987). The P waves from Amchitka Island explosions. *Geophys. J. R. Astr. Soc.*, **90**, 101-118.

Douglas, A. and J.A. Hudson (1990). The effect on teleseismic P of the zone of damage created by an explosion. *Geophys. J. Int.*, **103**, 111-133.

Douglas, A., Richardson, L. and M. Hutchins (1990). Surface reflections and S-P conversions on P seismograms. *Geophys. J. Int.*, **100**, 303-314.

Ebel, J.E., Burdick, L.J. and G.S. Stewart (1978). The source mechanism of the August 7, 1966 El Golfo earthquake. *Bull. Seism. Soc. Am.*, **68**, 1281-1292.

Filson, J. and C.W. Frasier (1972). Multisite estimation of explosive source parameters. *J. Geophys. Res.* **77**, 2045-2061.

Goldstein, P. and R.J. Archuleta (1987). Array analysis of seismic sources using Green's functions (Abstract). *EOS*, **68**, 1348.

Gupta, I.N., Lynnes, C.S. and R.A. Wagner (1990). Broadband F-K analysis of array data to identify sources of local scattering. *Geophys. Res. Letters*, **17**, 183-186.

Harris, D.B. (1989). Characterizing source regions with signal subspace methods: Theory and computational methods (draft). Lawrence Livermore Laboratory, Livermore, CA.

Harris, D.B. (1990). Comparison of direction finding performance of high frequency seismic arrays and three-component stations. *Bull. Seism. Soc. Am.*, **80B**, 1951-1968.

Hartzell, S. (1989). Comparison of seismic waveform inversion results for the rupture history of a finite fault: Application to the 1986 North Palm Springs, California, earthquake. *J. Geophys. Res.*, **94**, 7515-7534.

Hartzell, S.H. and T.H. Heaton (1983). Inversion of strong ground motion and teleseismic waveform data for the fault rupture history of the 1979 Imperial Valley, California, earthquake. *Bull. Seism. Soc. Am.*, **73**, 1553-1583.

Hartzell, S. and M. Iida (1990). Source complexity of the 1987 Whittier Narrows, California, earthquake from inversion of strong motion records. *J. Geophys. Res.*, **95**, 12475-12485.

Hartzell, S.H., Burdick, L.J. and T. Lay (1983). Effective source functions for Pahute Mesa nuclear tests. Final Technical Report, *WWCP-R-83-3*, Woodward Clyde Consultants, Pasadena, CA.

Hogg, R.V. and A.T. Craig (1978). *Introduction to Mathematical Statistics*. MacMillan Publishing Company.

Ingate, S.F., Husebye, E.S. and A. Christofferson (1985). Regional arrays and optimum data processing schemes. *Bull. Seism. Soc. Am.* **75**, 1155-1177.

Israelson, H. (1990). Correlation of waveforms from closely spaced regional events. *Bull. Seism. Soc. Am.*, **80B**, 2177-2193.

Jih, R-S., Shumway, R.H. and D.W. Rivers (1990). Maximum-likelihood magnitude-yield regression with censored information. (Submitted to the *Bull. Seism. Soc. Am.*).

Kanasewitch, E.R. (1981). *Time Sequence Analysis in Geophysics*. The University of Alberta Press.

Kedrov, O.K. and V.M. Ovtchinnikov (1990). An on-line analysis system for three-component seismic data: Method and preliminary results. *Bull. Seism. Soc. Am.*, **80B**, 2053-2071.

Kwaerna, R. and S. Mykkeltveit (1986). Optimum beam deployment for NORESS P-wave detection. In *NORSAR Semiannual Technical Summary*, L.B. Loughran Editor, 1 April-30 September 1985, No. I-86/87, 61-76.

Langston, C.A. (1976). Body wave synthesis for shallow earthquake source: Inversion for source and earth structure parameters. *Ph. D. Thesis. California Institute of Technology*.

Lay, Thorne. (1985). Estimating explosion yield by analytical waveform comparison. *Geophys. J.*, **83**, 1-30.

Marple, S.L. (1987). *Digital Spectral Analysis and Applications*. Prentice Hall Series on Digital Signal Processing.

McLaughlin, K.L., A.C. Lees, Z.A. Der and M.E. Marshall (1988). Teleseismic spectral and temporal M_0 and Ψ_∞ estimates for four French explosions in the southern Sahara. *Bull. Seism. Soc. Am.*, **78**, 1580-1596.

McLaughlin, K.L., Barker, T.G., Day, S.M., Shkoller, B. and J.L. Stevens (1988). Effects of depth of burial and tectonic strain release on regional and teleseismic P waveforms. AFGL-TR-88-0314, S-Cubed, La Jolla, CA, SSS-R-88-9844. ADA207541

- Mellman, G.R. and S.K. Kaufman (1981). Relative waveform inversion. *SGI-R-81-048*. Sierra Geophysics, Redmond, WA.
- Mendiguren, J.A. (1977). Inversion of surface wave data in source mechanism studies. *J Geophys. Res.*, **82**, 889-894.
- Mendoza, C. and S.H. Hartzell (1988). Inversion for slip distribution using teleseismic P waveforms, North Palm Springs, Borah Peak and Michoacan earthquakes. *Bull. Seism. Soc. Am.*, **78**, 1092-1111.
- Mueller, R.A. and J.R. Murphy (1971). Seismic characteristics of underground nuclear detonations. *Bull. Seism. Soc. Am.*, **61**, 1975.
- Murphy, J.R. (1977). Seismic source functions and magnitude determinations for underground nuclear detonations. *Bull. Seism. Soc. Am.*, **67**, 135-158.
- Murphy, J.R. Barker, B.W. and A. O'Donnell (1989). Network averaged teleseismic P-wave spectra for underground explosions. Part I. Definitions and examples. *Bull. Seism. Soc. Am.*, **79**, 141-155.
- Murphy, J.R. (1989). Network averaged teleseismic P-wave spectra for underground explosions: Part II. Source characteristics of Pahute Mesa explosions. *Bull. Seism. Soc. Am.*, **79**, 156-171.
- Mykkeltveit, S., Astebol, K., Doornbos, D.J. and E.S. Husebye (1983). Seismic array configuration optimization. *Bull. Seism. Soc. Am.* **73**, 173-186.
- Mudholkar, G.S. , Y.P. Chaubey and N. Lin (1976). Approximations for the noncentral-F distribution. *Commun. Statis. Theor. Meth.*, *A(5)1*, 49-63.
- Nabelek, J.L. (1984). Determination of earthquake source parameters from inversion of body waves. *Ph. D. Dissertation, Massachusetts Institute of Technology*.
- Olson, A.H. and J.G. Anderson (1988). Implications of frequency-domain inversion of earthquake ground motions for resolving the space-time dependence of slip on an extended fault. *Geophysical Journal*, **94**, 443-455.
- Owens, T.J., Taylor, S.R. and Zandt, G. (1987). Crustal structures at regional seismic test network stations determined from inversion of broadband teleseismic P-waveforms. *Bull. Seism. Soc. Am.*, **77**, 631-662.
- Pacheco, J.F., Estabrook, C.H., Simpson, D.W. and J.L. Nabelek (1989). Teleseismic body wave analysis of the 1988 Armenian earthquake. *Geophys. Res. Letters*, **16**, 1425-1428.
- Patton, H.J. (1988). Source models of the Harzer explosion from regional observations of fundamental and higher mode surface waves. *Bull. Seism. Soc. Am.*, **78**, 1133-1157.
- Pearce, R.G. (1977). Fault plane solutions using relative amplitudes of pP and P. *Geophys. J.R. Astr. Soc.*, **50**, 381-394.
- Pearce, R.G. (1980). Fault plane solutions using the relative amplitudes of P and surface reflections: further studies. *Geophys. J. R. Astr. Soc.*, **60**, 459-487.

- Pearce, R.G. and R.C. Stewart (1989). Interpretation of seismic pulse duration in terms of a propagating rupture: a method and case histories. *Tectonophysics*, **166**, 115-132.
- Pooley, C.I., Douglas, A. and R.G. Pierce (1983). The seismic disturbance of 1976 March 20 east Kazakhstan: earthquake or explosion? *Geophys. J.R. Astr. Soc.*, **74**, 621-631.
- Rivers, D.W. and D.H. vonSeggern (1979). Random scattering effects on Rayleigh wave amplitudes and phases. *SDAC-TR-78-3*, Teledyne-Geotech, Alexandria, VA.
- Robinson, E.A. (1967). *Multi-channel Time Series Analysis with Digital Computer Programs*. Holden Day.
- Schmidt, R.O. (1981). A signal subspace approach to multiple emitter location and spectral estimation. *Ph. D. Dissertation, Stanford University, Stanford, CA*.
- Shen, W.W. (1979). A constrained minimum power adaptive beamformer with time varying adaptation rate. *Geophysics*, **44**, 1088-1096.
- Shumway, R.H. (1988). *Applied Statistical Time Series Analysis*. Prentice Hall.
- Shumway, R.H. and Z.A. Der (1985). Deconvolution of multiple time series. *Technometrics*, **27**, 385-393.
- Steele, A.K. and C.L. Byrne (1990). High-resolution array processing using implicit eigenvector weighting techniques. *IEEE J.Ocean. Eng.*, **15**, 8-13.
- Stevens, J.L. (1986). Estimation of scalar moments from explosion-generated surface waves. *Bull. Seism. Soc. Am.*, **76**, 123-151.
- Stewart, R.C. and A. Douglas (1983). Seismograms from phaseless seismographs. *Geophys. J.R. Astr. Soc.*, **72**, 517-521.
- Tichelaar, B.W. and L.J. Ruff (1989). How good are our best models? Jackknifing, bootstrapping and earthquake depth. *EOS (Trans. AGU)*, **70**, May 16, 1989.
- von Seggern, D.H. (1972). Relative location of seismic events using surface waves. *Geophys. J. Astr. Soc.*, **26**, 499-513.
- von Seggern D.H. and R.R. Blandford (1972). Source time functions and spectra for underground explosions. *Geophys. J. R. Astr. Soc.*, **31**, 83-87.
- Vergino, E.S. (1989). Soviet test yields. *EOS, (Trans. Am. Geophys. Union)*, November 28.
- Wallace, T.C., Helmberger, D.V. and G.R. Mellman (1981). A technique for the inversion of regional data in source parameter studies. *J. Geophys. Res.*, **86**, 1679-1685.
- Widrow, B. (1966). Adaptive filters I: Fundamentals. Stanford Center for Systems Research. Systems Theory Laboratory, Stanford, CA.
- Willis, D.E. (1963). A note on the effect of ripple firing on the spectra of quarry shots. *Bull. Seism. Soc. Am.* **53**, 79-85.

APPENDIX A

Source imaging: A statistical theory

As we stated in the introduction of this report, one of the main goals of analysis of seismic data is to derive some properties of the source. In nuclear monitoring we desire to discriminate between events of various types, such as earthquakes and explosions either through the direct discrimination of source mechanisms or indirectly through determination of the source depth. It would be desirable to do this by some visual identification of sources after some preprocessing. In conventional processing of P wave data such identification can be performed through lining up the short period P waves and observing the pP "moveout", i.e., the changes in pP time with the values of slowness. Alternatively, one may apply some criteria using amplitude measurements in some time windows covering possible times of depth phases to ascertain that an event belong to either the earthquake or explosion category (Pearce 1980). Although such methods are clearly useful, they are somewhat tedious, and some future automation of such approaches is clearly desirable. In a broader sense going beyond the concept of point sources, detailed mapping of the sources of seismic radiation is also very important in studies of the mechanisms of earthquakes. In order to understand the faulting processes we need to know how the fault dislocation developed in time and space.

The discussion below establishes a proposed definition of the "source image", i.e., the estimated power of seismic sources as functions of space coordinates in the source region and derives confidence intervals for this image. We consider, as usual, the observed time vector $y(t)$ observed over N array elements or stations. The discrete Fourier transform of this can be written as

$$y = f s + n \quad (1)$$

where $s = s(x, \nu)$ is the Fourier transform of the theoretical signal at frequency ν and at source position vector x , usually specified as a combination of location and depth. The vector $f = f(x, \nu)$ is the transform of the function that combines with s to produce the data y . We can think of f as some combination of Green's functions. The vector f is assumed to be known whereas the signal s is deterministic and unknown. The noise vector n is assumed to be spatially white (uncorrelated among stations) with power spectral matrix

$$E(n n^*) = P_n(\nu) I \quad (2)$$

at frequency ν , where $P_n(\nu)$ is the noise power spectrum of each channel and I is the identity matrix.

Information carried by the observed vector y . One can simply plot the power in the generalized transform $f^* y$ as the beampower

$$B(x, \nu) = \frac{|f^* y|^2}{|f|^2} \quad (3)$$

An alternative measure with higher resolution is Capon's C , defined as

$$C(x, \nu) = \left[f^* (y y^* + c^2 I)^{-1} f \right]^{-1} \quad (4)$$

which can also be written in the form

$$C(x, v) = \frac{c^4}{|f|^2} \left(1 + \frac{B(x, v)}{(c^2 + |y|^2 - B(x, v))} \right) \quad (5)$$

which shows its relation to the generalized beam. It is convenient to define the residual power as

$$R(x, v) = |y|^2 - B(x, v) \quad (6)$$

so that

$$C(x, v) = \frac{c^4}{|f|^2} \left(1 + \frac{B(x, v)}{(c^2 + R(x, v))} \right) \quad (7)$$

the constant c is an arbitrary number chosen to make the matrix $(y y^* + c^2 I)$ non-singular.

A second alternative estimator is Shumway's F , defined as the likelihood ratio test statistic resulting from testing the model (1). This leads to

$$F(x, v) = (N - 1) \frac{B(x, v)}{R(x, v)} \quad (8)$$

which is closely related to the other two.

Capon's C and Shumway's F have similar resolving capabilities since they are both functions of B and R . They are both better than the generalized beampower from this point of view since equation (3) does not incorporate the residual noise power R . We shall show below that the F is superior statistically to the other two, both for detecting the predefined signal and for providing an estimator for the signal image.

If the noise is Gaussian, it is easy to show that

$$\frac{2 B(x, v)}{P_n(v)} \sim \chi^2_2(\delta^2) \quad (9)$$

where χ^2_2 denotes the chi-squared distribution with noncentrality parameter

$$\delta^2 = \frac{2 |S(x, v)|^2}{P_n(v)} \quad (10)$$

and \sim is a notation for "approximately distributed as". Note that δ^2 is twice the "signal-to-noise" ratio

$$\xi^2(x, v) = \frac{|S(x, v)|^2}{P_n(v)} \quad (11)$$

It is this signal-to-noise ratio that we propose to define as the image. It is also easy to show that

$$\frac{2 R(x, v)}{P_n(v)} \sim \chi^2_{2N-2}(0) \quad (12)$$

and is independent of $B(x, v)$. It follows that

$$F_{2, 2N-2}(\delta^2) = \frac{\chi^2_2(\delta^2) / 2}{\chi^2_{2N-2} / (2N-2)} \quad (13)$$

so that

$$F(x, v) = (N-1) \frac{B(x, v)}{R(x, v)} \quad (14)$$

has the non-central F distribution with the non-centrality parameter δ^2 given by equation (11). Hence the distribution of F depends only on the signal-to-noise ratio $\xi^2(x, v)$ for a given number of sensors N .

We may examine this further by noting that for an F with n_1 and n_2 degrees of freedom

$$E(F_{n_1, n_2}(\delta^2)) = \frac{n_1}{n_2} \cdot \frac{1}{n_2 - 2} \cdot (n_1 + \delta^2) \quad (15)$$

so that

$$E(F(x, v)) = \frac{(N - 1)}{(N - 2)} (1 + \xi^2(x, v)) \quad (16)$$

and the mean value is essentially the signal-to-noise ratio.

$$E(F_{n_1, n_2}^2(\delta^2)) = \frac{n_2}{n_1} \frac{1}{(n_2 - 2)(n_2 - 4)} [2n_1 + 4\delta^2 + (n_1 + \delta^2)^2] \quad (17)$$

can be used to compute the variance with

$$\text{var}(F) = E(F^2) - E^2(F) \quad (18)$$

and $n_1 = 2$, $n_2 = 2N - 2$. The variance depends on the signal-to-noise ratio that we are trying to estimate in a rather complicated way and the normal approximation will not be very good for obtaining an approximate confidence interval.

For any x and v , however, we can obtain an exact confidence interval for $E(F(x,v))$, δ^2 or ξ^2 in the following way. We know from (16) that

$$\hat{\xi}^2(x,v) = \frac{(N-2)}{(N-1)} F(x,v) - 1 \quad (19)$$

is an unbiased estimator of the signal to noise ratio (11) which we are defining as the image. Let $F(x,v)$ be some observed sample value of equation (14). Let δ^2_1 and δ^2_2 be two values of δ^2 such that

$$Pr \{ F_{2, 2N-2}(\delta_1^2) \leq F(x,v) \} = \alpha/2 \quad (20)$$

and

$$Pr \{ F_{2, 2N-2}(\delta_2^2) \leq F(x,v) \} = \alpha/2 \quad (21)$$

The resulting $1-\alpha$ confidence interval for δ^2 will be (δ^2_1, δ^2_2) . The interval for this signal-to-noise ratio is $(1/2 \delta^2_1, 1/2 \delta^2_2)$. This interval can also be connected into a $(1-\alpha)$ confidence interval for $E(F(x,v))$ using equation (16).

The above procedure can be used to get a $(1-\alpha)$ percent confidence interval for each x and v . Since the intervals are dependent, for n of them one can only assign an overall confidence of $1-n\alpha$. Therefore, in order to assign small confidence to the upper and lower surfaces of, say .90, with 100 points on the surface, each separate point should have $\alpha=.001$ or 99.9% confidence.

One may also investigate various pooling procedures if the model is repeated at M points, say

$$y_m = f_m s_m + n_m \quad (22)$$

for $m=1,2,M$, where $f_m = f(x, v_m)$, $s_m = s(x, v_m)$ and the spectrum of the noise is

$$E[n_m, n_m^*] = P_n(v) \quad (22)$$

so that it is relatively constant over the frequencies. Then, for

$$B(x, v_m) = \frac{|f_m^* y_m|^2}{|f_m|^2}, \quad (24)$$

$$\frac{2 B(x, v_m)}{P_n(v)} \sim \chi_2^2(\delta_m^2) \quad (25)$$

where

$$\delta_m^2 = \frac{2 |S(x, v_m)|^2}{P_n(v)} \quad (26)$$

It follows that the pooled value

$$\frac{2 \sum_{m=1}^M B(x, v_m)}{P_n(v)} \sim \chi_{2M}^2\left(\sum_{m=1}^M \delta_m^2\right) \quad (27)$$

Also, for the residual power

$$R(x, v_m) = |y_m|^2 - B(x, v_m), \quad (28)$$

it follows that

$$\frac{2 \sum_{m=1}^M R(x, v_m)}{P_n(v)} \sim \chi_{2M(N-1)}^2(0) \quad (29)$$

Hence, we have the result that

$$F(x, v_m) = (N-1) \frac{\bar{B}(x, v_m)}{\bar{R}(x, v_m)} \quad (30)$$

is distributed as a non-central F with $2M$ and $2M(N-1)$ degrees of freedom (Hogg and Craig 1978) and non-centrality parameter

$$\delta^2 = \frac{2 \sum_{m=1}^M |S(x, v_m)|^2}{P_n(v)} \quad (31)$$

One might also consider pooling the separate F values

$$F(x, v_m) = (N-1) \frac{B(x, v_m)}{R(x, v_m)} \quad (32)$$

leading to

$$F_2(x, v_m) = \frac{1}{M} \sum_{m=1}^M F(x, v_m) \quad (33)$$

An approximate interval might be based on normality and homogeneity (not likely to be true because of (17)) of the means and variances over v_m . Then a very rough and ready approximation would be

$$F_2(x, v_m) \pm z_{\alpha/2} \frac{s}{\sqrt{M}} \quad (34)$$

where

$$s^2 = \frac{1}{M-1} \sum_{m=1}^M (F(x, v_m) - F_2(x, v_m))^2 \quad (35)$$

and $z_{\alpha/2}$ is the upper $\alpha/2$ point on the normal distribution.

APPENDIX B

An alternative method for imaging

Although the estimation of source spatio-temporal configurations can be done effectively using the adaptation of Shumway's F-K method computing of confidence limits becomes somewhat crude if we assume normality and if we have only a few frequencies that contribute to the image. A normal distribution in this case is a very poor approximation to the superposition of noncentral F distributions. To derive an alternative approach we again start out with the model in the frequency domain, assuming that all quantities are complex and functions of frequency

$$y = f s + n \quad (1)$$

where the $n \times 1$ probe (Green's function) vector f relates the scalar signal s to the $n \times 1$ data vector with an additive vector of noises n assumed to be complex Gaussian with zero mean and a complex covariance matrix

$$E (n n^*) = P_n I \quad (2)$$

where I is the $n \times n$ identity matrix. We assume that the scalar signal s is univariate complex Gaussian with power density

$$E (s^* s) = P_s \quad (3)$$

which we are trying to estimate as a function of f 's to form an image. Assuming that it is stochastic rather than fixed makes the derivation of statistics easier, we need to work with only

central chi-squared variables. The following arguments are essentially adaptations of those in chapter 4.4.5 of Shumway (1988).

The key is to organize the test statistics that we have looked at before as a spectral analysis of variance problem. Denote the numerator B of our F statistics in the previous section as

$$B = \frac{f S f^*}{f f^*} \quad (4)$$

and interpret it as the power due to the signal since it is essentially the extra power (over $\text{tr}(S)$ where S is the spectral matrix of the data) accounted for in fitting the signal model. Denote the denominator by

$$R = \text{tr}(S) - B \quad (5)$$

which is the noise or residual error power.

This can be arranged in an *analysis of power table* as follows

Source	Power	Degrees of freedom	E(power)
-----	-----	-----	-----
Signal	$\frac{f S f^*}{f f^*}$	2	$f f^* P_s + P_n$
Noise	$\text{tr}(S) - \frac{f S f^*}{f f^*}$	$2(N - 1)$	$(N - 1) P_n$

Total

$tr(S)$

$2N$

Where N is the number of stations applied. We verify the expectation by noting that the beam power B is approximately distributed as

$$(ff^* P_s + P_n) \frac{\chi^2(2)}{2}$$

Then, since

$$E[\chi^2(m)] = m \quad (6)$$

we get the result. Note also that

$$var[\chi^2(m)] = 2m \quad (7)$$

so that

$$var(B) = (ff^* P_s + P_n)^2 \quad (8)$$

R is approximately distributed as

$$\frac{P_n \chi^2(2N-2)}{2}$$

so that $E(R) = P_n$ and

$$var(R) = (N-1) P_n^2$$

Now consider an unbiased estimator for the image P_s , defined as

$$\hat{P}_s = \frac{B - \frac{R}{(N-1)}}{f f^*} \quad (9)$$

It is clear that $E(\hat{P}_s) = P_s$ and that

$$\text{var}(\hat{P}_s) = \frac{\left[(f f^* P_s + P_n)^2 + \frac{P_n^2}{(N-1)} \right]}{(f f^*)^2} \quad (10)$$

It is clear that both the estimator and the estimator for its variance can be computed for the analysis of power table but we need to define the confidence intervals.

To obtain the confidence interval we use an old stratagem due originally to Satterthwaite (Ref?) and also used by Tukey (Ref?) to approximate the distribution of smoother spectral estimates with windows. We assume that the quantity \hat{P}_s , which is the weighted difference of chi-square variable can also be approximated with a chi-squared variable. We shall need the degrees of freedom for this chi-squared distribution. This can be estimated by taking the ratio of twice the expectation to the variance.

$$m = \frac{2 \left(E[\chi^2(m)] \right)^2}{\text{var}[\chi^2(m)]} \quad (11)$$

In our case this becomes

$$m = \frac{2 P_s^2}{\text{var}(\hat{P}_s)} \quad (12)$$

where $\text{var}(\hat{P}_s)$ has been computed earlier. The confidence interval can be computed using the fact that

$$m \frac{\hat{P}_s}{P_s}$$

has a $\chi^2(m)$ distribution.

Naturally, it is necessary to replace all quantities that are unknown in these expressions with their estimators from the analysis of power table above.

To derive confidence intervals for signal power estimated from pooling L independent values for various frequencies, the degrees of freedom m' for the pooled statistics, also assumed to be distributed as chi-squared, we get the degrees of freedom from the expression.

$$m' = \frac{2 L P_s^2}{\sum_{i=1}^L \text{var}(\hat{P}_{s,i})} \quad (13)$$

APPENDIX C

Implementation of multi-channel deconvolution in the X windows environment

In order to facilitate the use and the testing of the multi-channel deconvolution method we have written a version that makes use of the X-window environment. The program is menu driven with the following options for viewing in the Multi-channel Deconvolution Display (MDD):

- 1) Source estimate waveforms and resolution kernels.
- 2) Site transfer function (time domain) displays.
- 3) Source spectral estimates.
- 4) Site response spectra.
- 5) Original vs. reconstructed waveforms with associated correlation coefficients.

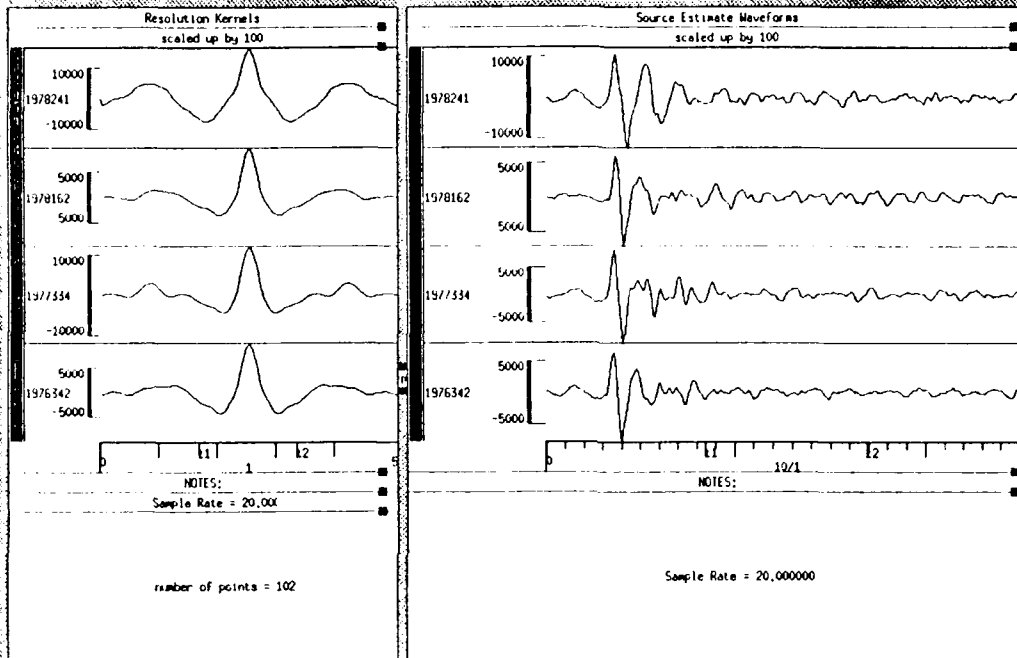
Examples of these various kinds of displays are shown in figures C1 to C4. For further explanations, we refer to the figure captions. When MDD is activated it creates a window and waits for user input. All input is entered by using a mouse. The right mouse button produces a menu of the options. The option is chosen by moving the mouse so that the desired option is highlighted and the left mouse button is pressed.

Once the option is chosen a window displaying the desired data appears. If all the data will not fit the window the first few waveforms will be displayed and the rest can be viewed by scrolling. A scrollbar appears at the left edge of each window. It can be used to scroll the data within that window by standard X11 scrollbar manipulations. Each new window will be created

on top of those currently displayed. All windows can be resized, moved and overlayed using standard X facilities.

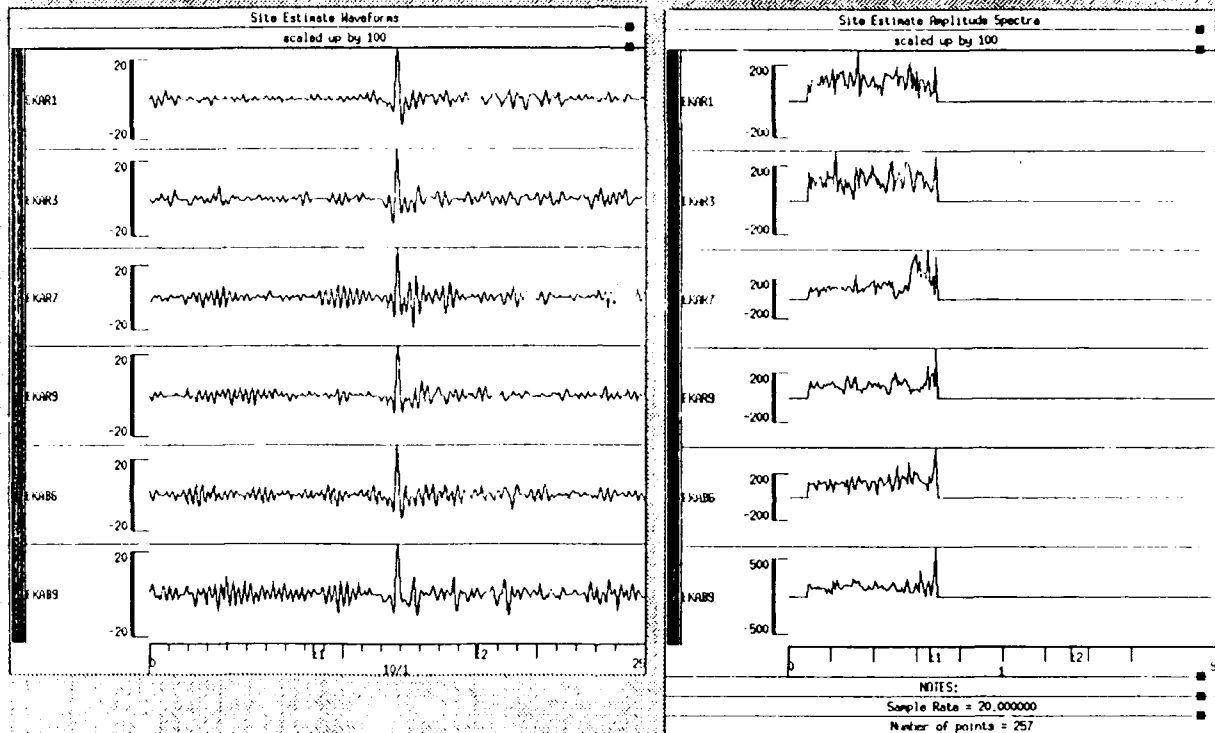
Multichannel Deconvolution Display

press F10 for menu



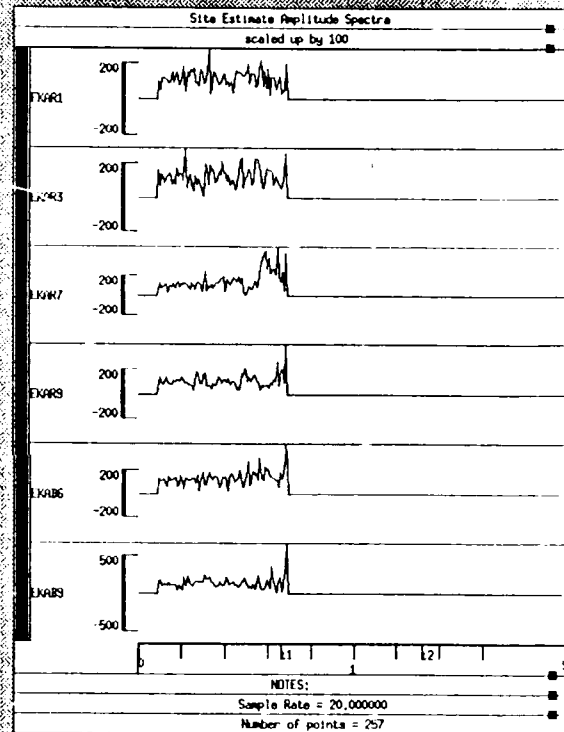
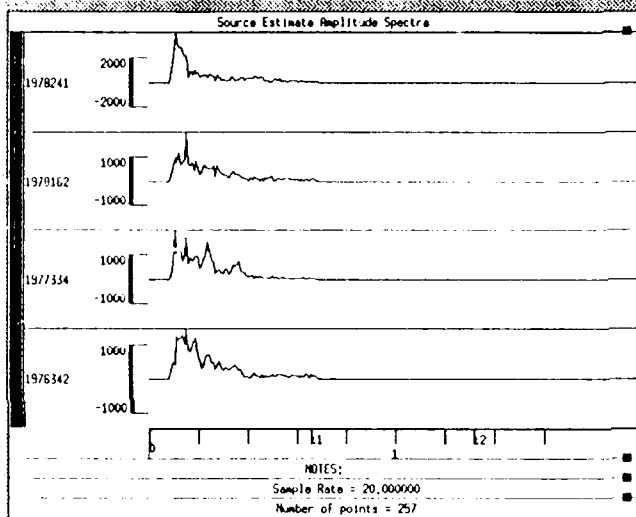
Multichannel Deconvolution Display

press right button for menu



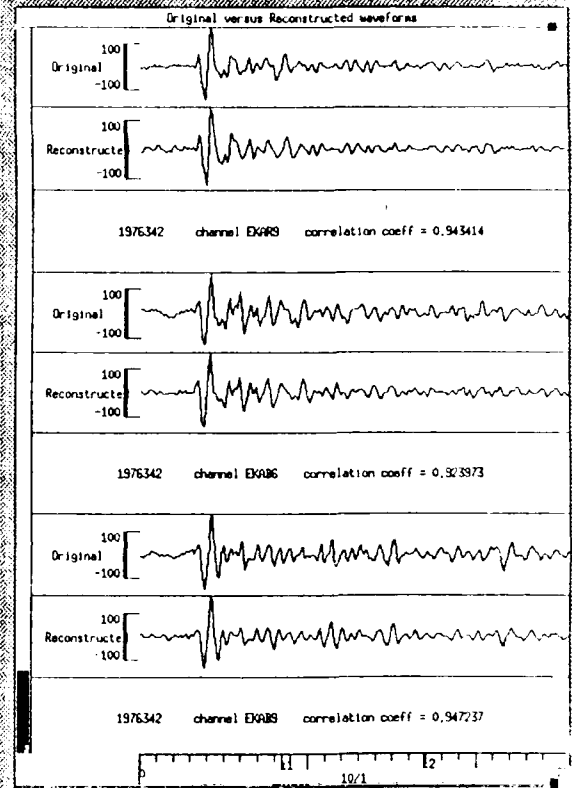
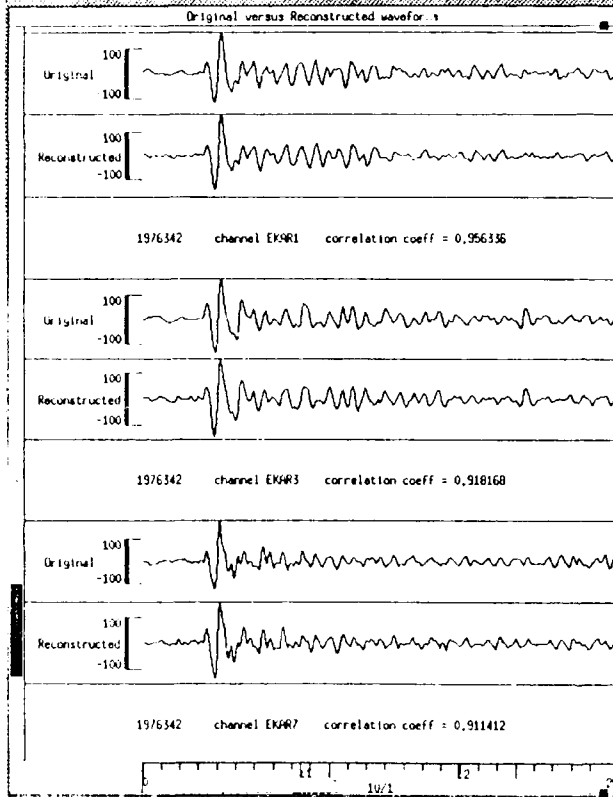
Multichannel Deconvolution Display

press right button for menu



Multichannel Deconvolution Display

press right button for menu



Prof. Thomas Ahrens
Seismological Lab, 252-21
Division of Geological & Planetary Sciences
California Institute of Technology
Pasadena, CA 91125

Prof. Charles B. Archambeau
CIRES
University of Colorado
Boulder, CO 80309

Dr. Thomas C. Bache, Jr.
Science Applications Int'l Corp.
10260 Campus Point Drive
San Diego, CA 92121 (2 copies)

Prof. Muawia Barazangi
Institute for the Study of the Continent
Cornell University
Ithaca, NY 14853

Dr. Jeff Barker
Department of Geological Sciences
State University of New York
at Binghamton
Vestal, NY 13901

Dr. Douglas R. Baumgardt
ENSCO, Inc
5400 Port Royal Road
Springfield, VA 22151-2388

Prof. Jonathan Berger
IGPP, A-625
Scripps Institution of Oceanography
University of California, San Diego
La Jolla, CA 92093

Dr. Gilbert A. Bollinger
Department of Geological Sciences
Virginia Polytechnical Institute
21044 Derring Hall
Blacksburg, VA 24061

Dr. Lawrence J. Burdick
Woodward-Clyde Consultants
566 El Dorado Street
Pasadena, CA 91109-3245

Dr. Jerry Carter
Center for Seismic Studies
1300 North 17th St., Suite 1450
Arlington, VA 22209-2308

Prof. Vernon F. Cormier
Department of Geology & Geophysics
U-45, Room 207
The University of Connecticut
Storrs, CT 06268

Professor Anton W. Dainty
Earth Resources Laboratory
Massachusetts Institute of Technology
42 Carleton Street
Cambridge, MA 02142

Prof. Steven Day
Department of Geological Sciences
San Diego State University
San Diego, CA 92182

Dr. Zoltan A. Der
ENSCO, Inc.
5400 Port Royal Road
Springfield, VA 22151-2388

Prof. Lewis M. Duncan
Dept. of Physics & Astronautics
Clemson University
Clemson, SC 29634-1901

Prof. John Ferguson
Center for Lithospheric Studies
The University of Texas at Dallas
P.O. Box 830688
Richardson, TX 75083-0688

Dr. Mark D. Fisk
Mission Research Corporation
735 State Street
P. O. Drawer 719
Santa Barbara, CA 93102

Prof. Stanley Flatte
Applied Sciences Building
University of California
Santa Cruz, CA 95064

Dr. Alexander Florence
SRI International
333 Ravenswood Avenue
Menlo Park, CA 94025-3493

Dr. Clifford Frohlich
Institute of Geophysics
8701 North Mopac
Austin, TX 78759

Dr. Holy K. Given
IGPP, A-025
Scripps Institute of Oceanography
University of California, San Diego
La Jolla, CA 92093

Prof. Henry L. Gray
Vice Provost and Dean
Department of Statistical Sciences
Southern Methodist University
Dallas, TX 75275

Dr. Indra Gupta
Teledyne Geotech
314 Montgomery Street
Alexandria, VA 22314

Prof. David G. Harkrider
Seismological Laboratory
Division of Geological & Planetary Sciences
California Institute of Technology
Pasadena, CA 91125

Prof. Danny Harvey
CIRES
University of Colorado
Boulder, CO 80309

Prof. Donald V. Helmberger
Seismological Laboratory
Division of Geological & Planetary Sciences
California Institute of Technology
Pasadena, CA 91125

Prof. Eugene Herrin
Institute for the Study of Earth and Man
Geophysical Laboratory
Southern Methodist University
Dallas, TX 75275

Prof. Bryan Isacks
Cornell University
Department of Geological Sciences
SNEE Hall
Ithaca, NY 14850

Dr. Rong-Song Jih
Teledyne Geotech
314 Montgomery Street
Alexandria, VA 22314

Prof. Lane R. Johnson
Seismographic Station
University of California
Berkeley, CA 94720

Dr. Richard LaCoss
MIT Lincoln Laboratory
M-200B
P. O. Box 73
Lexington, MA 02173-0073 (3 copies)

Prof. Fred K. Lamb
University of Illinois at Urbana-Champaign
Department of Physics
1110 West Green Street
Urbana, IL 61801

Prof. Charles A. Langston
Geosciences Department
403 Deike Building
The Pennsylvania State University
University Park, PA 16802

Prof. Thorne Lay
Institute of Tectonics
Earth Science Board
University of California, Santa Cruz
Santa Cruz, CA 95064

Prof. Arthur Lerner-Lam
Lamont-Doherty Geological Observatory
of Columbia University
Palisades, NY 10964

Dr. Christopher Lynnes
Teledyne Geotech
314 Montgomery Street
Alexandria, VA 22314

Prof. Peter Malin
Department of Geology
Old Chemistry Bldg.
Duke University
Durham, NC 27706

Dr. Randolph Martin, III
New England Research, Inc.
76 Olcott Drive
White River Junction, VT 05001

Prof. Thomas V. McEvilly
Seismographic Station
University of California
Berkeley, CA 94720

Dr. Keith L. McLaughlin
S-CUBED
A Division of Maxwell Laboratory
P.O. Box 1620
La Jolla, CA 92038-1620

Prof. William Menke
Lamont-Doherty Geological Observatory
of Columbia University
Palisades, NY 10964

Stephen Miller
SRI International
333 Ravenswood Avenue
Box AF 116
Menlo Park, CA 94025-3493

Prof. Bernard Minster
IGPP, A-025
Scripps Institute of Oceanography
University of California, San Diego
La Jolla, CA 92093

Prof. Brian J. Mitchell
Department of Earth & Atmospheric Sciences
St. Louis University
St. Louis, MO 63156

Mr. Jack Murphy
S-CUBED, A Division of Maxwell Laboratory
11800 Sunrise Valley Drive
Suite 1212
Reston, VA 22091 (2 copies)

Prof. John A. Orcutt
IGPP, A-025
Scripps Institute of Oceanography
University of California, San Diego
La Jolla, CA 92093

Prof. Keith Priestley
University of Cambridge
Bullard Labs, Dept. of Earth Sciences
Madingley Rise, Madingley Rd.
Cambridge CB3 0EZ, ENGLAND

Dr. Jay J. Pulli
Radix Systems, Inc.
2 Taft Court, Suite 203
Rockville, MD 20850

Prof. Paul G. Richards
Lamont Doherty Geological Observatory
of Columbia University
Palisades, NY 10964

Dr. Wilmer Rivers
Teledyne Geotech
314 Montgomery Street
Alexandria, VA 22314

Prof. Charles G. Sammis
Center for Earth Sciences
University of Southern California
University Park
Los Angeles, CA 90089-0741

Prof. Christopher H. Scholz
Lamont-Doherty Geological Observatory
of Columbia University
Palisades, NY 10964

Thomas J. Sereno, Jr.
Science Application Int'l Corp.
10260 Campus Point Drive
San Diego, CA 92121

Prof. David G. Simpson
Lamont-Doherty Geological Observatory
of Columbia University
Palisades, NY 10964

Dr. Jeffrey Stevens
S-CUBED
A Division of Maxwell Laboratory
P.O. Box 1620
La Jolla, CA 92038-1620

Prof. Brian Stump
Institute for the Study of Earth & Man
Geophysical Laboratory
Southern Methodist University
Dallas, TX 75275

Prof. Jeremiah Sullivan
University of Illinois at Urbana-Champaign
Department of Physics
1110 West Green Street
Urbana, IL 61801

Prof. Clifford Thurber
University of Wisconsin-Madison
Department of Geology & Geophysics
1215 West Dayton Street
Madison, WI 53706

Prof. M. Nafi Toksoz
Earth Resources Lab
Massachusetts Institute of Technology
42 Carleton Street
Cambridge, MA 02142

Prof. John E. Vidale
University of California at Santa Cruz
Seismological Laboratory
Santa Cruz, CA 95064

Prof. Terry C. Wallace
Department of Geosciences
Building #77
University of Arizona
Tucson, AZ 85721

Dr. William Wortman
Mission Research Corporation
8560 Cinderbed Rd.
Suite # 700
Newington, VA 22122

Prof. Francis T. Wu
Department of Geological Sciences
State University of New York
at Binghamton
Vestal, NY 13901

UNITED STATES (Others)

Dr. Monem Abdel-Gawad
Rockwell International Science Center
1049 Camino Dos Rios
Thousand Oaks, CA 91360

Michael Browne
Teledyne Geotech
3401 Shiloh Road
Garland, TX 75041

Prof. Keiiti Aki
Center for Earth Sciences
University of Southern California
University Park
Los Angeles, CA 90089-0741

Mr. Roy Burger
1221 Serry Road
Schenectady, NY 12309

Prof. Shelton S. Alexander
Geosciences Department
403 Deike Building
The Pennsylvania State University
University Park, PA 16802

Dr. Robert Burrige
Schlumberger-Doll Research Center
Old Quarry Road
Ridgefield, CT 06877

Dr. Kenneth Anderson
BBNSTC
Mail Stop 14/1B
Cambridge, MA 02238

Dr. W. Winston Chan
Teledyne Geotech
314 Montgomery Street
Alexandria, VA 22314-1581

Dr. Ralph Archuleta
Department of Geological Sciences
University of California at Santa Barbara
Santa Barbara, CA 93102

Dr. Theodore Cherry
Science Horizons, Inc.
710 Encinitas Blvd., Suite 200
Encinitas, CA 92024 (2 copies)

Dr. Susan Beck
Department of Geosciences
Bldg. # 77
University of Arizona
Tucson, AZ 85721

Prof. Jon F. Claerbout
Department of Geophysics
Stanford University
Stanford, CA 94305

Dr. T.J. Bennett
S-CUBED
A Division of Maxwell Laboratory
11800 Sunrise Valley Drive, Suite 1212
Reston, VA 22091

Prof. Robert W. Clayton
Seismological Laboratory
Division of Geological & Planetary Sciences
California Institute of Technology
Pasadena, CA 91125

Mr. William J. Best
907 Westwood Drive
Vienna, VA 22180

Prof. F. A. Dahlen
Geological and Geophysical Sciences
Princeton University
Princeton, NJ 08544-0636

Dr. N. Biswas
Geophysical Institute
University of Alaska
Fairbanks, AK 99701

Mr. Charles Doll
Earth Resources Laboratory
Massachusetts Institute of Technology
42 Carleton St.
Cambridge, MA 02142

Dr. Stephen Bratt
Center for Seismic Studies
1300 North 17th Street
Suite 1450
Arlington, VA 22209

Prof. Adam Dziewonski
Hoffman Laboratory, Harvard Univ.
Dept. of Earth Atmos. & Planetary Sciences
20 Oxford St
Cambridge, MA 02138

Prof. John Ebel
Department of Geology & Geophysics
Boston College
Chestnut Hill, MA 02167

Eric Fielding
SNEE Hall
INSTOC
Cornell University
Ithaca, NY 14853

Dr. John Foley
Phillips Laboratory/LWH
Hanscom AFB, MA 01731-5000

Prof. Donald Forsyth
Department of Geological Sciences
Brown University
Providence, RI 02912

Dr. Anthony Gangi
Texas A&M University
Department of Geophysics
College Station, TX 77843

Dr. Freeman Gilbert
IGPP, A-025
Scripps Institute of Oceanography
University of California
La Jolla, CA 92093

Mr. Edward Giller
Pacific Sierra Research Corp.
1401 Wilson Boulevard
Arlington, VA 22209

Dr. Jeffrey W. Given
SAIC
10260 Campus Point Drive
San Diego, CA 92121

Prof. Stephen Grand
University of Texas at Austin
Department of Geological Sciences
Austin, TX 78713-7909

Prof. Roy Greenfield
Geosciences Department
403 Deike Building
The Pennsylvania State University
University Park, PA 16802

Dan N. Hagedorn
Battelle
Pacific Northwest Laboratories
Battelle Boulevard
Richland, WA 99352

Dr. James Hannon
Lawrence Livermore National Laboratory
P. O. Box 808
Livermore, CA 94550

Prof. Robert B. Herrmann
Dept. of Earth & Atmospheric Sciences
St. Louis University
St. Louis, MO 63156

Ms. Heidi Houston
Seismological Laboratory
University of California
Santa Cruz, CA 95064

Kevin Hutchenson
Department of Earth Sciences
St. Louis University
3507 Laclede
St. Louis, MO 63103

Dr. Hans Israelsson
Center for Seismic Studies
1300 N. 17th Street, Suite 1450
Arlington, VA 22209-2308

Prof. Thomas H. Jordan
Department of Earth, Atmospheric
and Planetary Sciences
Massachusetts Institute of Technology
Cambridge, MA 02139

Prof. Alan Kafka
Department of Geology & Geophysics
Boston College
Chestnut Hill, MA 02167

Robert C. Kemerait
ENSCO, Inc.
445 Pineda Court
Melbourne, FL 32940

William Kikendall
Teledyne Geotech
3401 Shiloh Road
Garland, TX 75041

Prof. Leon Knopoff
University of California
Institute of Geophysics & Planetary Physics
Los Angeles, CA 90024

Prof. John Kuo
Aldridge Laboratory of Applied Geophysics
Columbia University
842 Mudd Bldg.
New York, NY 10027

Prof. L. Timothy Long
School of Geophysical Sciences
Georgia Institute of Technology
Atlanta, GA 30332

Dr. Gary McCartor
Department of Physics
Southern Methodist University
Dallas, TX 75275

Prof. Art McGarr
Mail Stop 977
Geological Survey
345 Middlefield Rd.
Menlo Park, CA 94025

Dr. George Mellman
Sierra Geophysics
11255 Kirkland Way
Kirkland, WA 98033

Prof. John Nabelek
College of Oceanography
Oregon State University
Corvallis, OR 97331

Prof. Geza Nagy
University of California, San Diego
Department of Ames, M.S. B-010
La Jolla, CA 92093

Dr. Keith K. Nakanishi
Lawrence Livermore National Laboratory
L-205
P. O. Box 808
Livermore, CA 94550

Prof. Amos Nur
Department of Geophysics
Stanford University
Stanford, CA 94305

Prof. Jack Oliver
Department of Geology
Cornell University
Ithaca, NY 14850

Dr. Kenneth Olsen
P. O. Box 1273
Linwood, WA 98046-1273

Prof. Jeffrey Park
Department of Geology and Geophysics
Kline Geology Laboratory
P. O. Box 6666
New Haven, CT 06511-8130

Howard J. Patton
Lawrence Livermore National Laboratory
L-205
P. O. Box 808
Livermore, CA 94550

Prof. Robert Phinney
Geological & Geophysical Sciences
Princeton University
Princeton, NJ 08544-0636

Dr. Paul Pomeroy
Rondout Associates
P.O. Box 224
Stone Ridge, NY 12484

Dr. Norton Rimer
S-CUBED
A Division of Maxwell Laboratory
P.O. Box 1620
La Jolla, CA 92038-1620

Prof. Larry J. Ruff
Department of Geological Sciences
1006 C.C. Little Building
University of Michigan
Ann Arbor, MI 48109-1063

Dr. Richard Sailor
TASC Inc.
55 Walkers Brook Drive
Reading, MA 01867

Dr. Susan Schwartz
Institute of Tectonics
1156 High St.
Santa Cruz, CA 95064

John Sherwin
Teledyne Geotech
3401 Shiloh Road
Garland, TX 75041

Dr. Matthew Sibol
Virginia Tech
Seismological Observatory
4044 Derring Hall
Blacksburg, VA 24061-0420

Dr. Albert Smith
Lawrence Livermore National Laboratory
L-205
P. O. Box 808
Livermore, CA 94550

Prof. Robert Smith
Department of Geophysics
University of Utah
1400 East 2nd South
Salt Lake City, UT 84112

Dr. Stewart W. Smith
Geophysics AK-50
University of Washington
Seattle, WA 98195

Donald L. Springer
Lawrence Livermore National Laboratory
L-205
P. O. Box 808
Livermore, CA 94550

Dr. George Sutton
Rondout Associates
P.O. Box 224
Stone Ridge, NY 12484

Prof. L. Sykes
Lamont-Doherty Geological Observatory
of Columbia University
Palisades, NY 10964

Prof. Pradeep Talwani
Department of Geological Sciences
University of South Carolina
Columbia, SC 29208

Dr. David Taylor
ENSCO, Inc.
445 Pineda Court
Melbourne, FL 32940

Dr. Steven R. Taylor
Lawrence Livermore National Laboratory
L-205
P. O. Box 808
Livermore, CA 94550

Professor Ta-Liang Teng
Center for Earth Sciences
University of Southern California
University Park
Los Angeles, CA 90089-0741

Dr. Gregory van der Vink
IRIS, Inc.
1616 North Fort Myer Drive
Suite 1440
Arlington, VA 22209

Professor Daniel Walker
University of Hawaii
Institute of Geophysics
Honolulu, HI 96822

William R. Walter
Seismological Laboratory
University of Nevada
Reno, NV 89557

Dr. Raymond Willeman
Phillips Laboratory/LWH
Hanscom AFB, MA 01731-5000

Dr. Gregory Wojcik
Weidlinger Associates
4410 El Camino Real
Suite 110
Los Altos, CA 94022

Dr. Lorraine Wolf
Phillips Laboratory/LWH
Hanscom AFB, MA 01731-5000

Dr. Gregory B. Young
ENSCO, Inc.
5400 Port Royal Road
Springfield, VA 22151-2388

Dr. Eileen Vergino
Lawrence Livermore National Laboratory
L-205
P. O. Box 808
Livermore, CA 94550

CONTRACTORS (Foreign)

Dr. Ramon Cabre, S.J.
Observatorio San Calixto
Casilla 5939
La Paz, Bolivia

Prof. Hans-Peter Harjes
Institute for Geophysik
Ruhr University/Bochum
P.O. Box 102148
4630 Bochum 1, FRG

Prof. Eystein Husebye
NTNF/NORSAR
P.O. Box 51
N-2007 Kjeller, NORWAY

Prof. Brian L.N. Kennett
Research School of Earth Sciences
Institute of Advanced Studies
G.P.O. Box 4
Canberra 2601, AUSTRALIA

Dr. Bernard Massinon
Societe Radiomana
27 rue Claude Bernard
75005 Paris, FRANCE (2 Copies)

Dr. Pierre Mecheler
Societe Radiomana
27 rue Claude Bernard
75005 Paris, FRANCE

Dr. Svein Mykkeltveit
NTNF/NORSAR
P.O. Box 51
N-2007 Kjeller, NORWAY (3 copies)

Dr. Peter Basham
Earth Physics Branch
Geological Survey of Canada
1 Observatory Crescent
Ottawa, Ontario, CANADA K1A 0Y3

Dr. Eduard Berg
Institute of Geophysics
University of Hawaii
Honolulu, HI 96822

Dr. Michel Bouchon
I.R.I.G.M.-B.P. 68
38402 St. Martin D'Heres
Cedex, FRANCE

Dr. Hilmar Bungum
NTNF/NORSAR
P.O. Box 51
N-2007 Kjeller, NORWAY

Dr. Michel Campillo
Observatoire de Grenoble
I.R.I.G.M.-B.P. 53
38041 Grenoble, FRANCE

Dr. Kin Yip Chun
Geophysics Division
Physics Department
University of Toronto
Ontario, CANADA M5S 1A7

Dr. Alan Douglas
Ministry of Defense
Blacknest, Brimpton
Reading RG7-4RS, UNITED KINGDOM

Dr. Manfred Henger
Federal Institute for Geosciences & Nat'l Res.
Postfach 510153
D-3000 Hanover 51, FRG

Ms. Eva Johannisson
Senior Research Officer
National Defense Research Inst.
P.O. Box 27322
S-102 54 Stockholm, SWEDEN

Dr. Fekadu Kebede
Geophysical Observatory, Science Faculty
Addis Ababa University
P. O. Box 1176
Addis Ababa, ETHIOPIA

Dr. Tormod Kvaerna
NTNF/NORSAR
P.O. Box 51
N-2007 Kjeller, NORWAY

Dr. Peter Marshall
Procurement Executive
Ministry of Defense
Blacknest, Brimpton
Reading FG7-4RS, UNITED KINGDOM

Prof. Ari Ben-Menahem
Department of Applied Mathematics
Weizman Institute of Science
Rehovot, ISRAEL 951729

Dr. Robert North
Geophysics Division
Geological Survey of Canada
1 Observatory Crescent
Ottawa, Ontario, CANADA K1A 0Y3

Dr. Frode Ringdal
NTNF/NORSAR
P.O. Box 51
N-2007 Kjeller, NORWAY

Dr. Jorg Schlittenhardt
Federal Institute for Geosciences & Nat'l Res.
Postfach 510153
D-3000 Hannover 51, FEDERAL REPUBLIC OF
GERMANY

Universita Degli Studi Di Trieste
Facolta Di Ingegneria
Istituto Di Miniere E. Geofisica Applicata, Trieste,
ITALY

Dr. John Woodhouse
Oxford University
Dept of Earth Sciences
Parks Road
Oxford OX13PR, ENGLAND

Dr. Ralph Alewine III
DARPA/NMRO
1400 Wilson Boulevard
Arlington, VA 22209-2308

Mr. James C. Battis
Phillips Laboratory/LWH
Hanscom AFB, MA 01731-5000

Harley Benz
U.S. Geological Survey, MS-977
345 Middlefield Rd.
Menlo Park, CA 94025

Dr. Robert Blandford
AFTAC/TT
Center for Seismic Studies
1300 North 17th St. Suite 1450
Arlington, VA 22209-2308

Eric Chael
Division 9241
Sandia Laboratory
Albuquerque, NM 87185

Dr. John J. Cipar
Phillips Laboratory/LWH
Hanscom AFB, MA 01731-5000

Cecil Davis
Group P-15, Mail Stop D406
P.O. Box 1663
Los Alamos National Laboratory
Los Alamos, NM 87544

Mr. Jeff Duncan
Office of Congressman Markey
2133 Rayburn House Bldg.
Washington, DC 20515

Dr. Jack Evernden
USGS - Earthquake Studies
345 Middlefield Road
Menlo Park, CA 94025

Art Frankel
USGS
922 National Center
Reston, VA 22092

Dr. Dale Glover
DIA/DT-1B
Washington, DC 20301

Dr. T. Hanks
USGS
Nat'l Earthquake Research Center
345 Middlefield Road
Menlo Park, CA 94025

Dr. Roger Hansen
AFTAC/TT
Patrick AFB, FL 32925

Paul Johnson
ESS-4, Mail Stop J979
Los Alamos National Laboratory
Los Alamos, NM 87545

Janet Johnston
Phillips Laboratory/LWH
Hanscom AFB, MA 01731-5000

Dr. Katharine Kadinsky-Cade
Phillips Laboratory/LWH
Hanscom AFB, MA 01731-5000

Ms. Ann Kerr
IGPP, A-025
Scripps Institute of Oceanography
University of California, San Diego
La Jolla, CA 92093

Dr. Max Koontz
US Dept of Energy/DP 5
Forrestal Building
1000 Independence Avenue
Washington, DC 20585

Dr. W.H.K. Lee
Office of Earthquakes, Volcanoes,
& Engineering
345 Middlefield Road
Menlo Park, CA 94025

Dr. William Leith
U.S. Geological Survey
Mail Stop 928
Reston, VA 22092

Dr. Richard Lewis
Director, Earthquake Engineering & Geophysics
U.S. Army Corps of Engineers
Box 631
Vicksburg, MS 39180

James F. Lewkowicz
Phillips Laboratory/LWH
Hanscom AFB, MA 01731-5000

Mr. Alfred Lieberman
ACDA/VI-OA State Department Bldg
Room 5726
320 - 21st Street, NW
Washington, DC 20451

Stephen Mangino
Phillips Laboratory/LWH
Hanscom AFB, MA 01731-5000

Dr. Robert Masse
Box 25046, Mail Stop 967
Denver Federal Center
Denver, CO 80225

Art McGarr
U.S. Geological Survey, MS-977
345 Middlefield Road
Menlo Park, CA 94025

Richard Morrow
ACDA/VI, Room 5741
320 21st Street N.W
Washington, DC 20451

Dr. Carl Newton
Los Alamos National Laboratory
P.O. Box 1663
Mail Stop C335, Group ESS-3
Los Alamos, NM 87545

Dr. Bao Nguyen
AFTAC/TIR
Patrick AFB, FL 32925

Dr. Kenneth H. Olsen
Los Alamos Scientific Laboratory
P. O. Box 1663
Mail Stop D-406
Los Alamos, NM 87545

Mr. Chris Paine
Office of Senator Kennedy
SR 315
United States Senate
Washington, DC 20510

Colonel Jerry J. Perrizo
AFOSR/NP, Building 410
Bolling AFB
Washington, DC 20332-6448

Dr. Frank F. Pilotte
HQ AFTAC/TT
Patrick AFB, FL 32925-6001

Katie Poley
CIA-ACIS/TMC
Room 4X16NHB
Washington, DC 20505

Mr. Jack Rachlin
U.S. Geological Survey
Geology, Rm 3 C136
Mail Stop 928 National Center
Reston, VA 22092

Dr. Robert Reinke
WL/NTESG
Kirtland AFB, NM 87117-6008

Dr. Byron Ristvet
HQ DNA, Nevada Operations Office
Attn: NVCG
P.O. Box 98539
Las Vegas, NV 89193

Dr. George Roane
HQ AFTAC/TTR
Patrick AFB, FL 32925-6001

Dr. Alan S. Ryall, Jr.
DARPA/NMRO
1400 Wilson Boulevard
Arlington, VA 22209-2308

Dr. Michael Shore
Defense Nuclear Agency/SPSS
6801 Telegraph Road
Alexandria, VA 22310

Mr. Charles L. Taylor
Phillips Laboratory/LWH
Hanscom AFB, MA 01731-5000

Phillips Laboratory
Attn: XO
Hanscom AFB, MA 01731-5000

Dr. Larry Turnbull
CIA-OSWR/NED
Washington, DC 20505

Phillips Laboratory
Attn: LW
Hanscom AFB, MA 01731-5000

Dr. Thomas Weaver
Los Alamos National Laboratory
P.O. Box 1663, Mail Stop C335
Los Alamos, NM 87545

DARPA/PM
1400 Wilson Boulevard
Arlington, VA 22209

Phillips Laboratory
Research Library
ATTN: SULL
Hanscom AFB, MA 01731-5000

Defense Technical Information Center
Cameron Station
Alexandria, VA 22314 (2 copies)

Phillips Laboratory
ATTN: SUL
Kirtland AFB, NM 87117-6008 (2 copies)

Defense Intelligence Agency
Directorate for Scientific & Technical Intelligence
Attn: DT1B
Washington, DC 20340-6158

Secretary of the Air Force
(SAFRD)
Washington, DC 20330

AFTAC/CA
(STINFO)
Patrick AFB, FL 32925-6001

Office of the Secretary Defense
DDR & E
Washington, DC 20330

TACTEC
Battelle Memorial Institute
505 King Avenue
Columbus, OH 43201 (Final Report Only)

HQ DNA
Attn: Technical Library
Washington, DC 20305

DARPA/RMO/RETRIEVAL
1400 Wilson Boulevard
Arlington, VA 22209

DARPA/RMO/Security Office
1400 Wilson Boulevard
Arlington, VA 22209